12-1-1995

Laser driven variable dot size thermal wax transfer printing

Steven Van Korol

Laser Driven Variable Dot Size Thermal Wax Transfer Printing

Steven Van Cleve Korol

A thesis submitted in partial fulfillment of the requirements for the degree of Master of Science in the Center for Imaging Science in the College of Imaging Arts and Sciences of the Rochester Institute of Technology.

December, 1995

Signature of Author_____

Accepted by Feb 6, 1996.

(Coordinator, M.S. Degree Program)

College of Imaging Arts and Sciences
Rochester Institute of Technology
Rochester, New York

Certificate of Approval

M.S. DEGREE THESIS

The M.S. Degree Thesis of Steven Van Cleve Korol has been examined and approved by the thesis committee as satisfactory for the thesis requirement for the Master of Science degree.

Dr. Dana Marsh, Thesis Advisor

Dr. Jon Arney

Mr. Paul Swift

Dec. 22, 1995

Date

Thesis Release Permission Form

Rochester Institute of Technology
College of Imaging Arts and Sciences

Laser Driven Variable Dot Size Thermal Wax Transfer Printing

I, Steven Van Cleve Korol, hereby grant permission to the Wallace Memorial Library of R.I.T. to reproduce my thesis in whole or in part. Any reproduction will not be for commercial use or profit.

Steven Van Cleve Korol

12/22/95

Date

Abstract

A digital image hardcopy device has been designed using a laser exposure mechanism, a pigmented wax/resin donor ink sheet, and an opaque receiver sheet. The writing system relies on image-wise thermal mass transfer of molten ink to the receiver in order to produce high resolution output. With the receiver media and a specially designed donor ribbon being held to a platen through vacuum pressure, a pulsed solid-state diode pumped near IR Nd:YAG laser provides the energy necessary to complete the thermal transfer process. By varying pulse width, dot size variation is possible. A mathematical model was developed to explain the physics of the imaging process and aid further experimentation. In order to maximize photothermal conversion and transfer efficiency while maintaining environmental friendliness, a water/alcohol based multi-layer donor ribbon was designed. Digital image analysis techniques and processing algorithms were developed specifically to provide a reliable quantification scheme for all variables. A randomized four factor central composite design provided a statistically robust means by which to map measured image quality. Response surface methods of factorial experimental design afforded a means to model the ribbon design space. Utilization of the *Downhill Simplex Method* (Nelder and Mead, 1965) yielded the optimum point on the estimated image quality response surface. The optimum point represented the final donor ribbon composition. It is primarily the continuously variable dot size capability and high thermal efficiency of the developed system that sets this research apart from other published works related to laser driven thermal transfer.

Acknowledgments

Due to the masterful instruction, guidance, and inspiration of the following four individuals, this thesis represents not only years of hard work, but also steadfast enthusiasm and dedication.

Mr. Paul Swift, International Imaging Materials, Inc.

Dr. Dana Marsh, Center for Imaging Science, R.I.T.

Dr. Jon Arney, Center for Imaging Science, R.I.T.

Mr. Ron Turi, Rexam Graphics

Dedication

As I contemplate the past years and the decisions I have made leading to this point in my career, a few faces shine more brightly than others. Who would have believed that my high school love of photography would lead to an M.S. in Imaging Science but my ever supporting parents, Emil and Peggy Korol, and Mr. Harold Sachwald, advisor of photography for my high school's newspaper. From there, Mr. Robert Kushner, technical photography instructor during my freshman year at R.I.T., gave me the self-confidence I needed to succeed in the imaging program. During my second year at R.I.T., I took my first courses in digital image processing with Dr. Russel Kraus. This was a crucial point in my career, for Dr. Kraus not only advised me to pursue my M.S. in Imaging Science, but also personally introduced me to the program. Without the patient instruction of Mr. Paul Swift, then Vice President of the R.I.T. Research Corporation's Imaging Division, I would not have mastered engineering fundamentals. He is my mentor -- he illustrated what electronic printing is and how to quantify and improve its quality. While introducing me to mathematical modeling and imaging system optimization, Dr. Dana Marsh guided me into my professional carreer . After completing coursework at R.I.T., Mr. Ron Turi, Rexam Graphics R&D Futures Manager, taught me some of the finer points of coating chemistry as he helped me to grow professionally. And I must finally add one of the only constants over the past five years, my closest friend, Karen McGovern, whose complete support enabled me to remain focused and to reach this important moment in my career.

Table of Contents

List of Figures

List of Tables

1.0 Introduction

> *Desktop publishers... still dream of the day when they can have imagesetters of their very own. They want the quality of today's imagesetters without all the muss and fuss -- and, of course, without the expense.*
>
> -- MacUser, April, 1995

In order to compete in tomorrow's desktop printing market, any worthy entry must excel in several areas, many of which conflict from an engineering standpoint. The educated desktop publisher leads an aggressive drive toward higher resolution, faster, less expensive, and environmentally friendly processes and machinery. Many current technologies vie for top honors and constantly strive to overcome inherent technological shortcomings. Rather than working to minimize the deficiencies of any one conventional printing system, research instead focused on the development of a novel electronic printing mechanism that has come into existence only within the last few years. The handful of researchers worldwide who have invested in this approach have been attracted largely by its capitalization on the intrinsic strengths of two proven technologies. Conventional direct thermal transfer (DT2) printing offers simple printing mechanics, near step function acuity, low operating cost, and environmental stability; however, spatial resolution is limited to 600 dots per inch (dpi), and the printing process is binary. Laser electrophotography, on the other hand, offers the potential for ultra high

spatial resolution and continuous tone printing, but the physics of stable image formation is complex, leading to environmental instability and high operating cost. Melding the strengths of these two technologies has led to an implementation of this novel electronic printing system capable of over 2000 dpi, 75 μs/dot writing speed, and continuous tone imaging. Driving the research was the desire to maximize thermal efficiency while achieving continuous tone capability.

Presently available are a few 1,200 dpi monochrome electrophotographic printers and a couple capable of 1,800 dpi. The list prices of these units are quite reasonable, ranging from $7,000 to $10,000, although their performance falls short of expectations set by costly 2,400 dpi laser driven imagesetters. Beyond image quality limitations, their complex electrophotographic engines lead to labor intensive operation, carrying with them, among other attributes, many unpopular consumer-replaceable components. There is no question that the current crop of high quality monochrome desktop printers leaves ample room for improvement of cost versus usability and imaging performance. It is with these considerations foremost in mind that this laser thermal transfer (LT2) printing system was designed.

Two allegations that are largely unjustified have limited developmental research into laser driven thermal transfer. Firstly, accompanying laser driven imaging, outside of electrophotography and some

silver halide systems, is the notion that powerful lasers must be used. And secondly, powerful lasers are equated to high capital investment and operating costs. With respect to the latter, as anyone familiar with the optical industry is aware, the power per unit cost of lasers continues to increase rapidly. To the former, the LT2 system was designed to prove that high power lasers are not necessary to produce high resolution thermal transfer printing systems. The researcher found that there is a range of temporal pulse widths over which LT2 imaging is possible. Pulses of higher intensity (more power) for shorter duration lead to non-steady state ablative imaging. Lower power pulses of longer duration are ideally suited to LT2. Taking advantage of the available range of pulse widths and the laser beam's Gaussian profile, continuous tone LT2 printing was investigated and proven to be feasible. These findings suggest strongly that LT2 is a viable high quality desktop printing technology worthy of further development.

2.0 Background Literature Review

When reviewing published literature and noting the distribution of report origins, it is not surprising to see that much of the research emanates in Japan and is often concerned not with parallel , but rather serial systems. Parallel systems utilize a stationary, page width linear array of heater elements to image over two thousand points simultaneously, whereas serial systems make use of a scanning linear array of a few (generally less than 100) elements. Serial thermal transfer printheads raster back and forth across the width of the page to build an image in a manner similar to the printheads found in many home ink jet printers. Serial systems must print very fast compared to parallel systems, in order to obtain equivalent throughput. For a desktop serial printer to achieve the same page speed as a parallel device, the allowed pulse width may be less than 1/3000 times that of the benchmark parallel system.

Following are reviews of several periodicals and patents that aided the research performed. While many works are included in this section, it is important to note that several additional texts were used, covering the topics of physical chemistry, surface chemistry, polymer science, heat conduction, lasers and electro-optical devices, and the statistics of designed experiments. All of the texts used are included in the References section.

2.1 Laser Thermal Transfer (LT2) Systems

All of the research performed required an intimate understanding of dynamic image formation in the printing nip. Many hours were spent using and researching systems related to that finally chosen. Two basic types of systems were investigated: conventional thermal transfer systems and laser driven systems. A fair amount of literature detailing various thermal mass transfer systems is available. The following sections review the articles and patents which served as the background necessary for an understanding of LT2 image formation.

2.1.1 Wax Ink Thermal Transfer Systems

Laser driven direct thermal transfer systems have been investigated by a few researchers over the last several years. The common conclusion to these reports takes one of two forms: the designed system either costs too much, or writes too slowly to warrant marketability as a desktop system. Although these conclusions are never explicitly stated, they are often implied. It is well known that a similar process including a dye diffusion receiver system has recently entered the market in the form of a high end digital proofing device. While this entry proves the viability of the technology in the high priced pre-press world, it also underscores the point that no one has been able to make laser driven thermal transfer a palatable option in the desktop printing arena.

In their paper entitled *High Definition Thermal Transfer Printing Using Laser Heating*, Irie, et. al. (1993) examined an LT2 system including a 780 nm, 30 mW continuous wave (cw) GaAlAs semiconductor diode laser, a single element lens (N.A. = 0.53), a hot-melt wax type ribbon, and conventional thermal transfer coated paper mounted onto a rotating drum. By focusing the beam to the diffraction limit, Irie, et. al. (1993) were able to achieve a spot size less than 5 μm. The minimum dot size they were able to transfer was 7.3 μm, although they made no mention of their ability to reproduce this dot size on a regular basis. At dot sizes this small, there is a very strong dependence on receiver topography that they do not mention. The smallest differences in height can cause poor contact between ribbon and receiver. In such a high resolution system, where there is no contact between a hot melt ribbon and the receiver, there will most likely be no image transfer. Therefore, it is of great importance to discuss the error associated with printing the highest dot frequency. This point is discussed with greater detail in section 4.6.

Perhaps the most intriguing aspect of the Irie, et. al. (1993) system was the rotating drum, to which the researchers were able to apply a heat bias. They found that by raising the drum temperature from ambient (25 °C) to 52 °C, they were able to increase image line width significantly. For example, at a recording speed of 23.7 mm/sec, line width roughly doubled with the increase in drum bias temperature. This effective increase in sensitivity is highly valuable. By holding the bulk of the wax ink just below its melting point, the

requirement of the laser is greatly relaxed. Rather than having to elevate the wax from ambient temperature to a point beyond its melting temperature, the beam must only push the wax ink over its melting point, greatly reducing the required power. Once above a threshold value, Irie, et. al. (1993) empirically found a linear relationship between line width and recording speed.

Although Irie, et. al. (1993) simulated the printing process with a three dimensional model, the only statement they drew out of the analysis was that they expected different energy requirements for short exposure times at high intensities and long exposure times at low intensities. They provided one example of this phenomenon; however, they did not provide any sort of derivation of their model. They did not use any part of their model for energy density calculations. For their set of desired conditions, Irie, et. al. (1993) calculated the energy density required to produce a 40 μm dot to be 5.3 mJ/mm^2. One must note that the researchers did not measure the laser power at the exposure plane, rather they used a measurement made at the exit aperture of the laser. Depending on the optical arrangement employed, such a measurement technique may have led to erroneous results; Irie, et. al. (1993) did not discuss optical losses. Their desired printing conditions included 5 mW incident beam power and writing speed of 23.7 mm/sec. Although Irie, et. al. (1993) did not explicitly present the calculation, at the conditions put forth, it would take about 11.75 hours to complete a letter size 600 dpi bitmap. Such a printer would reach the desktop market only with considerable difficulty, and little success once it got there. That is not to say

their system would not find a use in some other market, perhaps tag and label printing.

Although designing an efficient monochrome laser thermal transfer system is indeed difficult, designing a practical *color* laser thermal transfer system is even more complex due to the nature of the available process color (cyan, magenta, and yellow) pigments used in the wax inks. These color pigments tend to be fairly transparent at the near IR wavelengths of the laser sources used in LT2 technology. In fact, while the most efficient photothermal conversion will result from irradiance by longer IR wavelength sources, conventional color pigments become more transparent as the wavelength increases. For this reason, either an IR absorbent dye, tuned to the laser's output wavelength, must be added to the color pigmented wax, or a multi-layer ribbon must be employed. This multi-layer ribbon includes an IR absorbent layer coated onto the substrate that will not transfer, and a color pigmented thermo-sensitive wax layer. The IR absorbent layer may be referred to as the photothermal conversion layer (PCL).

In a report shortly following the work of Irie, et. al. (1993), an expanded group of researchers (Irie, Kato, et. al., 1993) described their investigations into a color LT2 system utilizing a unique hot-melt type ribbon. The researchers investigated two methods of producing their color ribbon, both of which relied upon a multi-layer design. The first of the two methods was to actually overlay a conventional black thermal transfer ribbon on a hot-melt

color wax ribbon. Laser light incident on the composite ribbon first passed through a poly(ethylene terephthalate) (PET) substrate, then into the carbon black layer where absorbed IR energy was converted to heat by the photothermal process. The heat propagated both back toward the source as well as through a minute air gap, through another layer of PET, and into the pigmented wax layer. Given enough energy density applied, the wax layer melted and transferred to the receiver.

Each of the two PET substrates had a thickness of 5.8 μm while the PCL and the ink layer were both 2.7 μm thick. The researchers made no mention of the additional air gap between the two ribbons. Their results, however, reflect its impact. Plots of Line Width vs. Laser Output for this type of ribbon show a large amount of variability not present in similar plots of other ribbon constructions. Print samples also reflect this phenomena. The researchers pointed out that "...the advantage of this structure was that the layers could be formed on the two sides of a base film, rendering manufacturing easy and the product stable" (Irie, Kato, et. al., 1993). While this statement is true, such a complex arrangement results in low thermal diffusion efficiency.

The second type of multi-layer ribbon investigated provided much higher efficiency. A carbon black loaded polyester resin was coated onto 5.8 μm PET at a coating thickness of 2 μm, forming the PCL. The color pigmented layer (carnauba wax plus pigment) was then coated onto the PCL to a coating thickness of 3 μm. This configuration proved more efficient

while producing results with greater repeatability. A series of single variable experiments led the researchers to the conclusion that the maximum resolution of the system was 2538 dpi. As with their earlier research, they made no mention of the error associated with the printing of the smallest dots. They did not state how they arrived at optimum conditions, or what specific criteria they used to judge image quality, but the researchers did decide on 5 mW laser power and 15.1 mm/sec recording speed. These exposure conditions produced 33 μm line widths. Using a coarse method of calculation (power divided by recording speed multiplied by dot size) led to 10.0 mJ/mm^2 recording energy density. This combination of high resolution and slow scanning speed results in a printing time of 11.8 hours to complete a letter size 600 dpi bitmap.

2.1.2 Resin Ablation Transfer Systems

A group of scientists and engineers at Rexam Graphics, South Hadley, Massachusetts and at the University of Illinois at Urbana Champaign have completed much research on a close cousin of LT2, namely Laser Ablation Transfer imaging (LAT). The three papers and three patents studied (Tolbert, et. al., July/Aug., 1993; Tolbert, et. al., Sept./Oct., 1993; Lee, et. al., 1992; Ellis, et. al., 1991; Ellis, et. al., 1992; Foley, et. al., 1992) provided a detailed description of the LAT imaging process. The literature traces the development of the process including specifics of the laser system. Although the nature of the non-equilibrium LAT process is very different from that of DT2, the theory of laser exposure system design and quantification proved very useful to this

research. Further, given the similarities between exposure systems and ink ribbon constructions, many of the ideas presented regarding heat conduction could be applied to the LT2 process.

Ellis, Lee, Foley, Tolbert, et. al. worked with a few laser systems, one of which was very similar to the configuration used for this research. Both systems employed diode pumped Nd:YAG semiconductor lasers operating in cw mode. While the LT2 system made use of an electro-optic modulator (EOM) to slice the cw output into discrete pulses, the LAT researchers chose an acousto-optic modulator (AOM). Although the chosen beam modulation mechanisms differed, the desired output was the same: to selectively, in an image-wise fashion, allow some fraction of laser radiation to affect the wax ink donor ribbon. Both systems held donor and receiver in place via vacuum chuck and moved media beneath the beam with a motorized x-y table. Specifics of the LT2 engine are discussed with detail in section 4.1. The LAT researchers proposed several methods for measuring the actual laser pulse, rather than relying upon the screen readouts of the laser's power supply and pulse generator. Versions of these same methods greatly aided quantification of the LT2 system described in section 4.1.

Donor material for LAT is similar to that of LT2 in that it too consists of one or more layers of ink coated onto a PET substrate. Although the LAT substrate is much thicker (120 μm versus 5.7 μm), and LAT ink is not thermo-setting (at the first order), there are many similarities in the heating of the

donor by near-IR laser radiation. Heat conduction may be modeled in a similar fashion; however, the authors were quick to point out that image formation is quite different. In LAT, "...the substrate interface of the ablatable coating is irradiated with submicrosecond, near-IR laser pulses with Gaussian spatial profiles. The large transient temperature jump produced near this interface causes a partial decomposition of the coating. Gas-phase products propel a spot of material from the film to a receiver sheet" (Lee, et. al., 1992). The LAT imaging process relies upon non-equilibrium conditions caused by extremely rapid heating of the donor in an image-wise fashion.

In order to initiate this miniature explosion, it is necessary to apply a large amount of energy in a very short period of time. Both benefits and drawbacks are present in such a system; while it is very fast, it is also very costly. Laser output power on the order of 2 to 9 W is required for LAT. Because LT2 requires the melting of waxes and soft resins rather than partial decomposition of an ethylcellulose/phenolic resin system, the power requirement of the laser is much less. For example, in LT2, the laser must be of sufficient power to generate peak temperatures of about 400 °C, with no fundamental constraints on the dwell time required to exceed the ink's melting point. By contrast, minimum ablation temperatures in LAT exceed 600 °C. Furthermore, these temperatures must be generated in a very short period of time in order to induce the required non-equilibrium state. With near-IR lasers, high power equates to high cost. A 2 W cw diode-pumped Nd:YAG laser costs between $15,000 and $20,000; Q-switched models cost even

more. The trade-off is one of throughput; exposure times for LT2 may be anywhere from a couple to many times greater than those for LAT.

The first LAT films developed by the group consisted of an ink layer coated onto 120 μm PET and were later referred to as Type I LAT donors. The binder of the ink layer consisted primarily of equal portions of ethylcellulose and a phenolic resin. The black ink was pigmented with graphite. Color inks were produced by pigmenting the binder with a near-IR absorbing dye (American Cyanamid Cyabsorb IR-165) and common gravure inks rather than graphite. At the laser's output wavelength, absorbance

$$A = -\log_{10} A_f, \tag{1}$$

where A_f is the fractional absorption, was about 1.5 for the black ink layer and 0.53 for cyan, magenta, and yellow. The first of the three LAT papers and the first of the three LAT patents researched deal entirely with this first type of film. Later literature focuses on more advanced Type II materials, but includes information on Type I films as well.

The main problem associated with the Type I materials was the comparatively low sensitivity of the color films. Type I color inks absorbed almost 2/3 less light than the Type I black ink. Of course, it was possible to increase the sensitivity of the color inks by adding more IR dye, at the cost of color fidelity. Cyabsorb IR-165 is not completely transparent over the visible wavelengths. Type II films represented improvement over Type I films in

their increased sensitivity due to the addition of a dynamic release layer, referred to by the authors as the DRL. The patents covering type II films gave many examples of metals that could be used for the DRL; however, a thin layer (≈30 Å) of vacuum-deposited aluminum was the primary DRL material discussed in the papers. Because the concept of a *dynamic* release layer is foreign to wax thermal transfer, further study of LAT focused on Type I films.

Lee, et. al. (1992) modeled the average spatial fluence of the pulse uniformly, as a cylindrical function

$$J_{avg} = \frac{E_p}{\pi r_o^2}, \tag{2}$$

where r_o is the Gaussian ($1/e^2$) beam radius and E_p is the applied pulse energy. Lee, et. al. (1992) pointed out that the peak fluence of a Gaussian pulse, J_{pk}, is the fluence at the center of the pulse, and may be written as

$$J_{pk} = \frac{2E_p}{\pi r_o^2} = 2J_{avg}. \tag{3}$$

It was noted that "...when a film is irradiated by Gaussian profile pulses of increasing E_p, ablation occurs first at the center of the profile" (Lee, et. al., 1992). This fact holds true for LT2 imaging. Further, the authors explained "...the value of J_{pk} that just produces a spot at the center is defined as J_{th}. When $J_{pk} = J_{th}$, the radius of the [imaged] spot r is approximately equal to zero. Above J_{th}, the [imaged] spot radius is an increasing function of the fluence" (Tolbert, et. al., July/Aug., 1993).

Note that their "...definition of J_{th} does not necessarily imply that a film irradiated by a uniform spatial profile pulse of radius R will ablate a spot of radius R, because a Gaussian profile and a uniform profile might produce different edge effects.... It is common among imaging applications to specify a different type of threshold, which [they] call J_{im}. J_{im} is defined as the value of J_{avg} that produces a... spot whose radius r equals r_o.... It is convenient to think of these quantities as follows. When $J_{avg} = 1/2J_{th}$, the center of the pulse is just above threshold and the spot radius r is approximately equal to zero. When $J_{avg} = J_{im} \approx 3.7J_{th}$, the $1/e^2$ intensity points of the pulse are just above threshold and $r \approx r_o$" (Tolbert, et. al., July/Aug., 1993). Such a definition of the spatial pulse is a convenient simplification that may be used in making quick calculations of fluence based on spot size.

Investigations were made by Tolbert, et. al. (July/Aug., 1993) into the temporal temperature profile as well as the spatial profile within LAT films during ablation. Reasoning that in Type II heating, the DRL is much thinner than the spatial pulse is wide, a one-dimensional model was investigated. The same simplification is considerably more risky when modeling Type I films, although the authors do not point this out. They cast the source terms conventionally, as

$$\frac{\partial T(z,t)}{\partial t} = D\frac{\partial^2 T(z,t)}{\partial z^2} + S(z,t) \qquad (4)$$

where D is diffusivity (assumed to be constant), and $S(z,t)$ models the effects of nonuniform pulsed laser heating (Tolbert, et. al., July/Aug., 1993). The

above equation was solved numerically using the Crank-Nicolson finite difference method. The source term $S(z,t)$ was modeled as

$$S_j^{n+1} = P^{n+1}[A_f \frac{\partial(z_j = 0)}{C_{Al} d_{Al}} + (1 - R - A_f) \times \frac{\alpha_{dye}}{C_{pol}} \exp(-\alpha_{dye} z_j)] \quad (5)$$

where n and j are the time and space indices, P^{n+1} is the laser intensity at time $\Delta t(n+1)$, A_f and R are the fractions absorbed and reflected by the DRL, C_{Al} and C_{pol} are the heat capacities of aluminum and polymer, and α_{dye} is the absorption coefficient of the ablatable coating (Tolbert, et. al., July/Aug., 1993). For Type I films, and for LT2 films, the first term in the brackets does not exist, simplifying the equation to

$$S_j^{n+1} = P^{n+1}[(1 - R - A_f) \times \frac{\alpha_{dye}}{C_{pol}} \exp(-\alpha_{dye} z_j)] \cdot \quad (6)$$

This equation shows that in Type I LAT and in LT2, the donor film heats up when exposed to the laser pulse due to absorption of the radiation by some pigment in the ink layer. Tolbert, et. al. (July/Aug., 1993) pointed out that this heating is exponentially distributed through the coating according to Beer's law.

It is important to realize that when the ink melts (or Al layer, in Type II films), there is an increase in heat capacity, which was not incorporated by the model of Tolbert, et. al. (July/Aug., 1993). The researchers made the assumption that heat capacity is independent of temperature. As they point out, "...this assumption is adequate to describe the film just below threshold,

but not to describe the film above threshold." (Tolbert, et. al., July/Aug., 1993) They go on to explain that their "...simplified thermal calculations would predict the temperature in the center of the spot to be enormous, but [the calculations] neglect the substantial increases in heat capacity from the melting aluminum and the decomposing coating" (Tolbert, et. al., July/Aug., 1993). The researchers' temperature calculations are by no means invalid, but they do decrease in accuracy toward the center of the irradiated spot.

2.2 Direct Thermal Transfer (DT2) Systems

In conventional DT2, the printing *nip*, or the specific region where imaging takes place, appears elegantly simple in comparison to such complicated systems as electrophotography. Although not to scale, Figure 2.2.1 provides a look at a cross-section of the conventional DT2 nip. To produce an image, the donor ribbon is placed in contact with the receiver sheet and the pair is passed between the thermal printhead and the platen under moderate pressure. As the donor and receiver pass beneath the printhead, the heater elements are fired in an image-wise manner. After passing through the nip, the donor ribbon is separated from the receiver sheet. In areas where a sufficient amount of heat was applied to the donor/receiver pair, wax ink adheres to the receiver, rather than to the ribbon substrate, producing wax ink dots. Although the printing system seems relatively simple, the complex interactions of printer hardware and controller software, ribbon, and receiver have led many researchers to investigate the intricacies of this printing technology. Since LT2 is a close cousin to

conventional DT2, a good deal of preliminary information applicable to LT2 was acquired by investigating existing conventional DT2 literature.

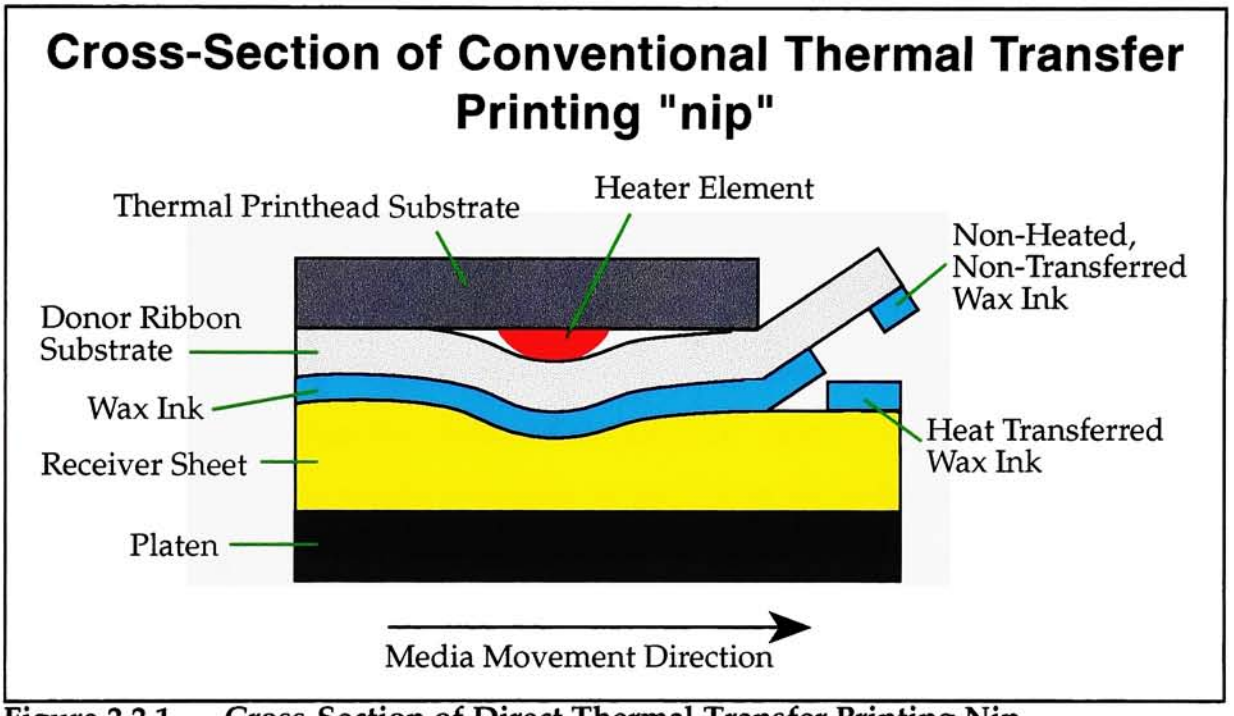

Figure 2.2.1 ~ Cross-Section of Direct Thermal Transfer Printing Nip.

A good deal of the Japanese DT2 history deals with the serial printhead thermal transfer typewriter industry, according to the nature of the reports available -- almost as much as with bar code printing. It is important to note that although the method of heating in LT2 is very different than with DT2, it is in fact another type of serial system. A fair amount of the information dealing with traditional serial DT2 printers is applicable to this unique system. While literature pertaining directly to the various methods of laser heat induced imaging is perhaps of greatest import to this research, there is

much information to be gained from conventional DT2 systems, especially in the areas of ink chemistry and physical properties.

2.2.1 Influence of Ink Properties on Printed Dots

In a 1991 IS&T paper entitled *Relation Between Dynamic Characteristics of Thermo-Fusible Ink and Print Quality in Thermal Transfer Printing*, Abe, et al. (1991) studied the ability of single pixel printed dots to fill or span voids on the receiver. Generally *image voids*, or *voids*, are defined as printed areas of the receiver lacking ink, and are caused by the failure of the wax ink to transfer from the ribbon to the receiver. Abe, et al. (1991) found that by increasing the *tensile elongation* of the ink at its melting point (about 70°C), image voids decreased. *Tensile elongation*, or simply *elongation*, was measured by molding a stick of thermal transfer wax ink, heating the stick to a controlled temperature (0°C to 70°C), stretching the stick lengthwise at a controlled rate (100 mm/min), and measuring the length of elongation at the point when the ink stick yielded (in millimeters). The researchers found, in their serial system, the initial and final temperatures of pulsed heater elements to be equal. In so doing, the researchers determined there was no accumulation of heat energy by the printing system during the printing process. In most DT2 systems, there is significant accumulation of heat that cannot be ignored and is conventionally dealt with through the use of both mechanical heat sinks and fins, cooling fans, and software techniques. Determining the accumulation of heat to be negligible greatly simplifies the DT2 printing process. Because Abe, et al. (1991) were able to enjoy the luxury

of this simplification, they concluded the print quality of a small dot to be influenced by the ink's tensile strength at room temperature (20°C).

Two rheological properties were measured: viscosity (cone/plate type) and tensile elongation. Although the measurements of rheological properties were valid, the analysis of resulting images is suspect. Abe, et al. (1991) define "Dot reproducibility" as:

" D_{rep} = [Printed Images of 20 Dots]/[(10 heat elements of print head) x 1.5] "

where "Printed Images of 20 Dots" is proportional to the area fraction of ink within a given area of printed image. Specifically, 20 dots (single pixels) were printed in a four-by-five grid, spaced evenly by a two pixel dot pitch. "10 heat elements of print head" is equal to the area of 10 printed dots. While this ratio is weighted (to take into account the size of the actual printed element shape, or *footprint*, which is elongated, they claim, by ribbon movement during heating), the equation relies on the integration of a 20 dot matrix. The model does not distinguish between a high quality image of the proper dimensions and one of inferior quality but having the same integrated printed area. For example, a print that contains many regions where the paper shows through the imaged area (voids) as well as a trailing edge that has been smeared, may very well yield an identical D_{rep} as the ideal image. In fact, one would expect that if tensile elongation is increased, void regions may be spanned, but trailing edge effect would also increase. If this is indeed

the case, their results would be erroneous. An image quality metric based on one attribute is elegant in its simplicity; however, if chosen carelessly, it will yield results that do not always correlate with perceived image quality.

Abe, et al. (1991) reported that "The ability to bend is directly dependent on tensile elongation. The transferred ink may still be in the soft state at the separation stage when the printing speed is high (150 mm/sec). If the ink is torn easily and cannot be stretched so much, the ink cannot form a uniform membrane covering the paper surface. Thus, many voids will be brought about in the printed images. Accordingly, ink which is easily elongated is expected to bring good print quality with few voids" (Abe, et. al., 1991). While Abe, et al. (1991) subscribed to a theory in which voids are *spanned* by the molten wax ink rather than *filled*, they did not consider the effects of accumulated heat when large (10 mm x 10 mm) solid fill areas are printed. It is interesting that they chose a void spanning theory when their ribbon design was of the hot melt type. Section 3.2 discusses some of the reasons why resin type ribbons, rather than hot melt, are commonly associated with the void spanning theory.

In conclusion, Abe, et al. (1991) divided the DT2 imaging process into three stages: 1) ink melting, 2) adhesion of the molten ink to the receiver sheet, and 3) separation of the ribbon from the receiver. The researchers concluded that ink adhesion to a paper surface is influenced by printing speed and ink viscosity. In their system, a low viscosity ink containing "...paraffin

wax, polyethylene wax, polymers, and small amounts of chemical agents..." (Abe, et. al., 1991) combined with slow printing speeds produced the best results, although they did not present any data supporting work on system optimization.

2.2.2 Influence of Ink Properties on Solid Areas

The Konica Corporation, in 1987 published an SPSE paper entitled *Quantitative Analysis of Print Quality Features* which was subsequently supplemented with a 1988 SPSE paper *Quantitative Evaluation of Print Quality of Thermal Transfer Printing*. The latter of these, written by Yasuhiko Tanaka, Kunihiro Koshizuka, and Takao Abe, brought to the scientific community several valid and interesting points related to conventional receiver image receptivity (Tanaka, et. al., 1987). As opposed to the Abe, et al. (1991) IS&T paper, the evaluation was of a 24x24 dot solid area, not serially printed dots. The researchers determined that print quality depends on three factors:

1) Properties of softening ink to adhere to a paper surface.
2) Strength of an ink membrane against elongation.
3) Cohesive failure of an ink at the moment when an ink ribbon is separated from a paper surface just after the heating process.

Their research centered around (2) above "...because it was expected that the strength would be connected with the uniformity of an ink membrane laid on an undulating surface" (Tanaka, et. al., 1987).

The basis of the Konica reports stemmed from *The Study on Properties of Thermal Transfer Ink Ribbon* (Kunihiro, et. al, 1986) where the idea of the importance of the ultimate elongation was first stated. The authors declared that the void rate (determined by the method of Abe, et. al., 1991, described above) "...has little relation to... results of the D.S.C. curve and the viscosity. The void rate is affected by the position of a heat element of a thermal head and an environmental temperature" (Kunihiro, et. al, 1986). They further found that void rate decreases with ultimate elongation to a point at which "stringing" (trailing edge effects) become too great for acceptance.

All of the ribbons constructed by Tanaka, et. al. (1987) had a release layer comprised of "...waxes and resins" (Tanaka, et. al., 1987). Ink composition consisted of four binders (three resins and one paraffin wax) and carbon black. A total of five ribbon formulations were produced. Results were equated to differences in "ultimate elongation" (having the same definition as tensile elongation) rather than ink component differences. No claims were made regarding relationships between ink formulation and image quality. With one of the formulations, two coating weights were examined. From this experiment the researchers determined that increasing coating weight decreases void rate in solid fills to some extent. "The void rate apparently decreases in the [thick ribbon] case compared with the [thin ribbon case], though the degree is not so great. However, when an ink layer was too thick, the degradation of print quality was observed" (Tanaka, et. al., 1987).

An interesting point brought out by Tanaka, et. al. (1987) was the failure of viscosity (cone/plate type) or melting point to correlate well with resulting print quality. Instead, it was found that the *integrated* void rate, or the percentage of a solid printed area not covered with ink, was minimized when the ink demonstrated proper strength against elongation at room temperature. Like Abe, et al. (1991), Tanaka, et. al. (1987) also subscribed to a theory supporting the spanning of voids. Although they made the distinction between raggedness of the leading edge of the print and what they term "blur" of the trailing edge, they failed to recognize that their "blurred" trailing edge effect is not necessarily due to heat accumulation in the printhead elements. Tanaka, et. al. (1987) defined "blur" as a "tail" of increased ink deposition at the trailing edge of printed pixels. They attributed "tail" entirely to the problem of heat accumulation, yet when images of characters produced with single pixels were presented (where heat accumulation truly would have been negligible), a "tail" attached to each printed dot was definitely visible, albeit unaccounted for.

Tanaka, et. al. (1987) reported that paper smoothness is certainly not the only property that effects print quality, and that for extremely smooth papers, the resulting image is sometimes *comb-like* in the machine direction. A comb-like image may be envisioned by picturing the teeth of a hair comb. In such a solid image, wax ink adheres to the substrate only at the points where maximum energy is applied: the center portion of each element. The minute gaps between the elements are not imaged. The authors believed this result

to be due to "...the insufficiency of heat required to move ink from a ribbon onto the paper surface" (Tanaka, et. al., 1987). Contrary to Tanaka, et. al. (1987), the researcher of this thesis subscribes to a different theory. In this contrary theory, the *comb phenomenon* described above results not only from the thermal properties of such smooth coated papers but also, and in some cases primarily, from surface chemical properties of smooth synthetic receiver sheets. A receiver whose surface resists dynamic wetting by the molten ink in the printing nip will keep the wax from fusing to the surface, thereby causing it to *bead* and only adhere to the areas where the differences in surface energy are the least. These areas correspond to the regions where the ink viscosity is the lowest -- where applied energy is the highest.

2.2.3 Influence of Receiver Properties on Image Quality

Historically, there has been much emphasis on the need for "specialty papers" when DT2 image quality is of paramount importance. U.S. Patent 4,686,549 (Williams, et. al., 1987) describes with great detail the parameters of greatest importance when designing a receiver for thermal transfer. Primarily, the patent, belonging to 3M, discusses overhead transparency material, although the coatings described could be combined with a variety of synthetic or paper based materials. The authors described the transfer onto a paper receiver as "...a combination of adhesion, capillary action, and mechanical intermingling of wax and paper fibers. Because the porosity of the paper makes the adhesion area of the paper receptor sheet much greater than the surface area occupied by the image on the donor sheet, release from

the backing of the donor sheet and transfer to and adhesion on the paper receptor sheet is favored" (Williams, et. al., 1987). Some nonconventional synthetic receivers attempt to mimic the porosity of paper in order to enhance receptivity of molten wax ink. In fact, the synthetic sheet used in the LT2 system of this thesis is a highly uniform micro-porous receiver. Without a special receiver, the output quality of LT2 would be greatly reduced. The LT2 receiver is described with greater detail in section 4.6.

The authors of U.S. Patent 4,686,549 (Williams, et. al., 1987) explained that if the receiver is a polymeric film such as PET, transfer depends entirely upon the adhesion of the softened thermoplastic ink to the smooth film surface. Because there is no possibility of "mechanical coupling," the adhesive properties of the film are of greatest importance. Bare PET cannot be used because it has very low compressibility compared to paper and does not make good contact with the donor sheet. Further, the heat capacity of the material plays a strong role. The heat capacity of a material is related to the quantity of heat required to raise the temperature of unit mass of a substance through a small temperature range; the higher the heat capacity, the more difficult the task of raising a substance's temperature. The authors of the patent found that the high heat capacity of uncoated PET films limited maximum thickness to 50.8 μm. Referring back to Figure 2.2.1, note the platen backing the receiver. Although not pointed out by Williams, et. al. (1987) the platen, with intrinsically low heat capacity, was of benefit to sufficiently thin films, where it reflected heat back into the receiver,

effectively lowered the receiver's heat capacity, and promoted imaging. With films having calipers greater than 50.8 μm, the effect of the low heat capacity platen was negligible. While thinner films imaged due to their being backed by a platen of lower heat capacity in sufficiently close proximity to the heater element, the high thermal inertia of thick, uncoated PET films kept the receiver from achieving temperatures required for imaging.

Williams, et. al. (1987) reported that "Critical surface tension is a measure of the *wettability* of a solid surface, and surfaces having higher wettability exhibit higher values of critical surface tension. Calculation of the critical surface tension of a material consists of recording contact angles of drops of various liquids on the surface of a layer of material being evaluated, plotting a curve of contact angle against surface tension of the liquid, and extrapolating to a contact angle of zero. The critical surface tension is the surface tension which a liquid would have to have in order to just form a droplet with zero contact angle with the surface under consideration" (Williams, et. al., 1987). The authors of the patent found that donor and receiver coatings must be designed so that the critical surface tension of the receiver is higher than that of the molten ink, allowing wetting of the receiver surface by the ink. They further reported that the coating should ideally be compatible with the donor ink material, so that intermixing of the ink and coating takes place during heating. For this purpose, waxes common to donor ink binders are employed in receiver coatings. Waxes also serve the purpose of modifying receiver hardness so that the sheet remains sufficiently

hard at room temperature, but becomes soft when imaged, thereby enhancing intermixing and compliance.

Concentrating on image quality, by choosing appropriate amounts of proper surface tension modifiers and hardness modifying waxes, Williams, et. al. (1987) claimed that a coating may be formulated so that a two or three ingredient lacquer will yield excellent image quality when applied at the optimum weight with the optimum process. Some examples of useful polymers mentioned by the authors include poly(caprolactones), chlorinated polyolefins, blends of chlorinated polyolefins and poly(methylmethacrylate), block copolymers of styrene-ethylene/butylene-styrene, and copolymers of ethylene and vinyl acetate. Some examples of waxes used include beeswax, carnauba wax, paraffin wax, microcrystalline wax, and other synthetic hydrocarbon waxes. In summary, this patent outlines the important parameters for thermal transfer receivers as 1) possessing the ability to be wetted by the molten wax, 2) being compliant enough to insure intimate contact between receiver and donor in the printing nip, and 3) being soft enough to facilitate good adhesion/intermixing during the imaging process.

2.2.4 Mathematical Descriptions of DT2 Systems

In their article *Temporal and Spatial Response in Thermal Transfer Printing*, Davids, et. al. (1987) discussed thermal diffusion of the ribbon and its effect on the temporal response and spatial resolution of the system. The authors proposed both one and two-dimensional heat flow models for

conventional DT2 printing. Their experimental findings correlated very well to those computed via their solutions of the well known heat equation. Although their system was more-or-less conventional, the paper provided insight into DT2 system modeling.

Davids, et. al. (1987) found that diffusion through the ribbon caused a significant reduction in the temperature of the ink, and a corresponding delay in the time at which maximum ink temperature is achieved. Perhaps the most significant declaration was the finding that "...lateral heat flow in the ribbon is found to cause only a small effect on spatial resolution, even for high-resolution print heads." At high printing speeds, however, the time delay "...caused by the diffusion process through the ribbon and the retardation associated with the latent heat of fusion..." can cause a decrease in media movement direction resolution (Davids, et. al., (1987).

Swift developed a method for describing the thermal response of DT2 printing systems (Swift, 1991). In the report, Swift described the reasoning and methodology of the measurement process as well as insight into the thermal transfer imaging process. A governing equation for DT2 printing was proposed along with a procedure to correlate the printhead input energy to the resulting image. It was stated that when implemented properly, the described process can be used to quantify ribbon/paper parameters with a high degree of accuracy and precision.

2.3 Related Systems and General Information

Infrared Microradiometry of Thermal Inkjet Heaters (Muller, et. al., 1989) provided insight into the measurement of temperature profiles of small resistive heating elements. While thermal ink jet is quite a different technology from thermal wax transfer, it shares the fundamental thermal physics of thin film resistor elements. Various pulse widths, frequencies, voltages, and heater geometries were studied. No unexpected conclusions arose; rather the paper confirms the logical conclusions one would form given knowledge of resistive heaters.

An article entitled *Waxes* (Letcher, 1984) does well to describe in some detail the wax ingredients common to hot-melt thermal transfer wax ink. Descriptions, physical properties, and chemical components by weight are given for many waxes. The information found within provides excellent background into the chemistry of the primary constituent ink ingredients. Texts expanding on this article and providing greater detail include **The Chemistry and Technology of Waxes** (Warth, 1956) and **Commercial Waxes** (Bennett, 1956).

3.0 Approach

In order to design this research project, a modular approach was taken. Tasks were divided into separate projects, each requiring a unique set of experiments. Many of these *sub-projects* depended on information, a developed process, or a piece of equipment designed in a previous series of experiments, while some were independent of others and could be researched simultaneously. Indeed, much thought went into not only the substance of each sub-project, but also into the order in which the sub-projects were completed.

The first sub-project examined the difficulties of producing thermal transfer ribbons. For these experiments, a conventional print engine was used for testing, as the goal was to investigate fundamental ribbon chemistry and manufacture. Once it was determined that thermal transfer ribbons could be successfully formulated and built in an R&D lab by the experimenter, effort then shifted to decisions relating to the engine architecture. Both conventional and novel approaches were studied. Once the laser writing engine was decided upon, work began on a mathematical model of image formation while simultaneously ribbon design work began anew. As ribbon designs became more refined, quantified image quality measurement became more important. At this time, digital image analysis techniques were employed to study image quality. Once every piece of the system was operating properly, an experimental design study ensued in order to optimize the system for a given set of conditions. The following sub-sections outline

the various decisions that were made in approaching the overall research project.

3.1 Engine Architecture Decision

In designing a high resolution, high throughput, continuous tone direct thermal transfer printing system, several fundamental decisions had to be made. Initial experimentation showed that a few basic limitations would have made development of such a system based on conventional DT2 architecture extremely difficult. Using many commercially available ribbons, an Atlantek Model 200 thermal print engine, and a 300 dpi printhead (Kyocera KST-216-8MPD1), it was determined early on that two primary facts force the design of a conventionally-based high resolution, continuous tone system into the hands of software engineers.

Indeed, conventional thermal transfer printer manufacturers place a good deal of their resources in discovering novel ways to compensate and mask two limitations of their systems:

- effects caused by residual heat in the printhead bulk and elements
- the technological limits of conventional printhead manufacturing processes.

Both of these limitations relate to the printhead itself. With respect to the former, there is not much that can be done about the diffusivity of heat in a printhead, yet it is essential that ink ribbon melting is controlled quite

precisely. Addressing the latter, increasing spatial resolution of conventional printheads leads to a rapid escalation in unit price.

Metal heat sinks, fins, and fans will only buy so much, relegating the bulk of residual heat compensation methods to software solutions. Residual heat effects further hinder continuous tone thermal transfer by reducing the signal-to-noise ratio (SNR) of an already fragile system. Thin film resistive element printhead process yields decrease with the size of the elements and the increase of the number of elements. Reasons of cost limit all but one very expensive commercial color DT2 printer to the use of printheads having no greater addressibility than 300 dpi. In order to claim "high resolution" (1200 dpi or greater) with a conventional system, addressibility may be increased in the media movement direction; however, pixel size (resolution) cannot change from the technology limited maximum 600 dpi, leading to complex dithering algorithms. While current DT2 printer manufacturers choose to optimize conventional 300 dpi DT2 engines with elaborate software algorithms, the decision was made to investigate a novel type of thermal printing system with the potential to exceed the current benchmark level of performance.

A few articles, discussed in the Background Literature Review, proclaimed the advantages of laser driven thermal transfer. The systems described in these articles suffered from either lack of speed or excessive cost for the desktop printing market. The technical depth of all of the articles was

limited; none of the articles described any sort of an optimization process of materials or exposure system. None of the articles touted the potential for continuous tone imaging. Therefore, the focus of the research became the quest for a fast, economical way to produce high resolution, continuous tone direct thermal transfer output using a laser exposure system. Figure 3.1.1 presents a block diagram of the chosen system.

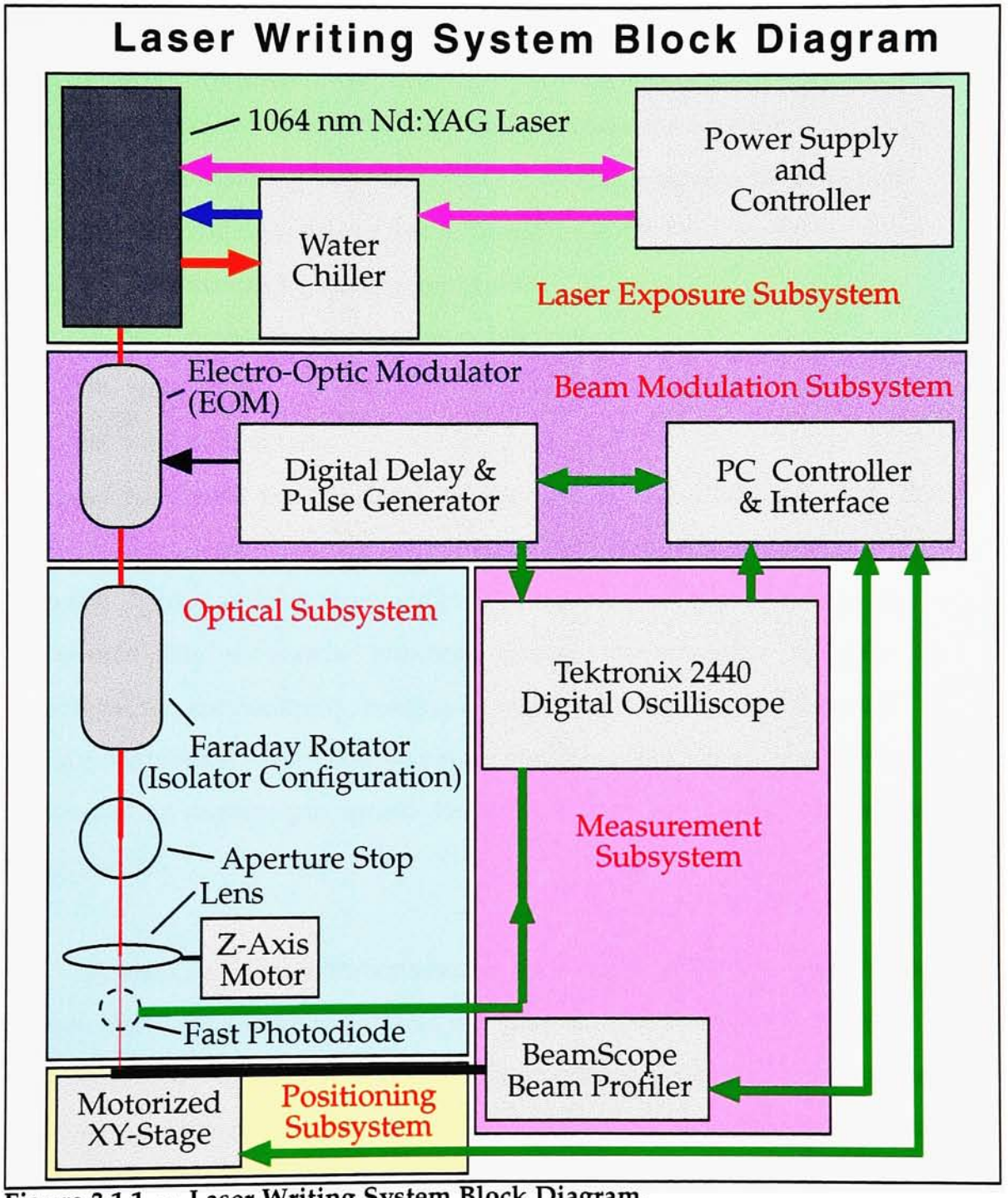

Figure 3.1.1 ~ Laser Writing System Block Diagram.

3.2 Ink Ribbon Chemistry Decision

Given knowledge of the fundamental engine configuration, it became necessary to choose a chemistry upon which to base the wax ink. Components comprising inks used for DT2 or LT2 include a thermoplastic binder system and a pigment. At the lowest level, binder systems for use in DT2/LT2 systems can be one of three types:

- wax based, also referred to as hot melt
- resin based
- wax-resin blends.

Of these, wax based systems dominate the desktop DT2 printing market. Wax based inks work well with receivers that have been optimized for use in these systems. Typical opaque receivers for DT2 wax inks are heavily coated and calendared cellulosic sheets. Important receiver characteristics include smoothness, compressibility, coating compatibility with the wax ink, and surface wettability. Resin and wax-resin blend inks are not necessarily so dependent on receiver properties. Receivers will be discussed in greater detail in section 4.6.

A couple of generalizations can be made about wax inks. First, when molten, wax inks adhere to surfaces that they are able to wet. That is, they will adhere only to receiver materials whose critical surface energy is greater than theirs. Second, wax inks do not typically exhibit much tensile strength. Therefore, wax inks do not perform well on rough surfaces, for, while the wax may stick firmly to any area of the receiver with which it makes contact,

cohesive forces are not strong enough to force neighboring hot wax to span void areas in the receiver. In some cases, wax inks can be formulated to fill small voids; however, in so doing, such inks often show increased sensitivity to residual heat, caused by a necessarily low melt temperature (T_m).

Resin based inks, on the other hand, place different requirements on the receiver sheet. Critical surface energy is still a key requirement, as is compressibility, though there may be less emphasis on smoothness depending on the formulation. By definition, resins are complex mixtures of organic compounds that possess no definite melting point (Bennett, 1956). When heated, resin inks become soft; however, it is important to note that they do not melt. The glass transition temperature (T_g), or temperature at which a material changes from a glass to a soft, rubbery state, is an important physical parameter that greatly aids quantification of a resin's behavior. A resin based system may be optimized so that its tensile strength in the softened state is great enough to span small voids in the receiver (see Figure 3.2.1). Such formulations are difficult to create in that the softened ink's tensile strength must be great enough to allow void spanning, but less than the strength of the bond between the solid ink and the film substrate. If these requirements are not met, too much ink may release from the ribbon, resulting in elongated pixels and decreased media movement direction (y-axis) resolution.

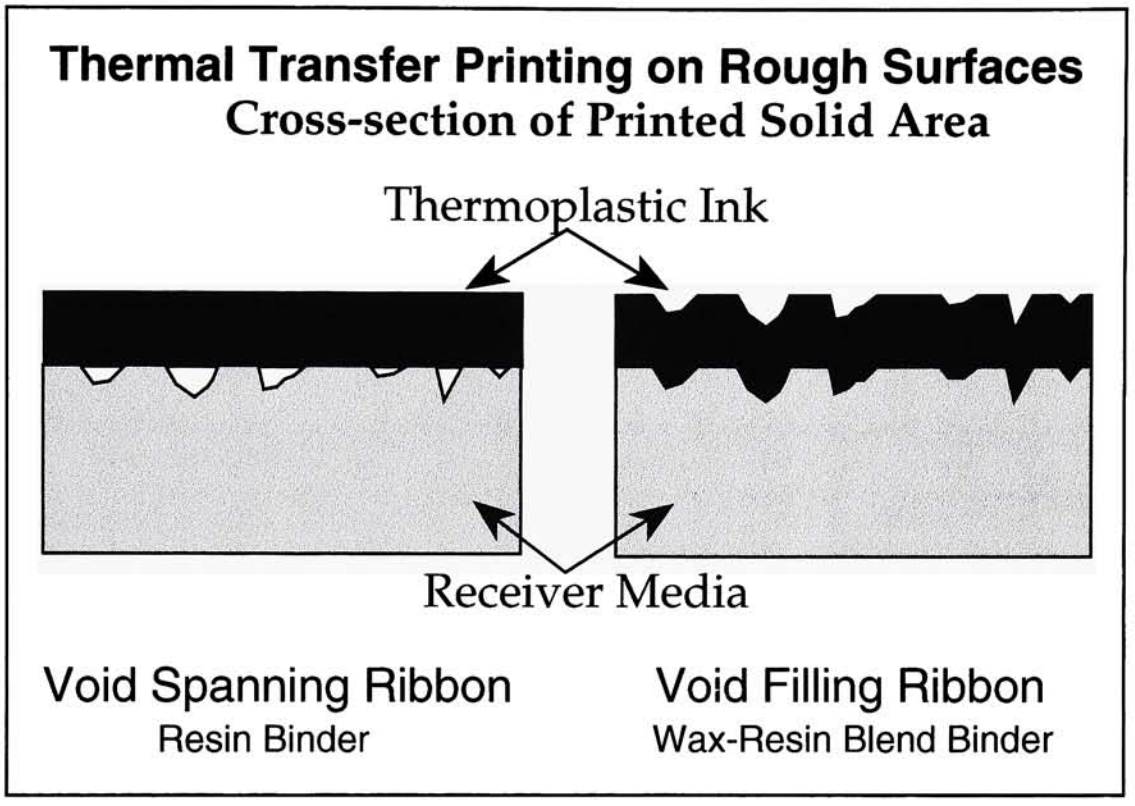

Figure 3.2.1 ~ Thermal Transfer Printing on Rough Surfaces.

Wax-resin blends offer perhaps the greatest flexibility of the possible ink binder system types. Depending on the application, wax-resin blends may be formulated so that the molten-state rheology allows the ink to conform and adhere to many surfaces. While resin based inks may be formulated to span voids, wax-resin blends may be made to fill voids (see Figure 3.2.1). Blending waxes and resins affords the chemist greater design latitude with respect to the physical parameters of the ink. For example, as the amount of *resin* increases, the tensile strength of the ink may *increase*, while as the *wax* content increases, the tensile strength of the ink may *decrease*. Using the T_g

of the resin and the T_m of the wax as guidelines, suitable waxes and resins may be blended in many ways to create inks with widely varying printing properties. Because of this added design flexibility (and not because of a desired ability to fill voids), the decision was made to produce an ink based on wax-resin blend binder chemistry. Flexibility of design was of paramount importance to the experimentation process.

Wax-resin inks may be mixed and coated in two ways: either with the binder components molten (wax and resin above T_m and T_g, respectively) or with finely divided binder components solid (wax and resin below T_m and T_g, respectively) and dispersed in a solvent. If the latter is chosen, a dispersion is prepared in which undissolved pigment and binder particles are suspended in some liquid. Solvent dispersions provide such benefits as the rapidity at which inks can be mixed, freedom to mix at room temperature, independence of coating viscosity from temperature, and simple clean up procedures. These pluses are partially offset by the difficulties of formulating and producing a stable dispersion, of determining the optimal solids percentage for use in coating, of determining appropriate drying conditions, and of obtaining the desired coating weight after the drying process, once the solvent has evaporated.

By comparison, the molten wax mix making process is extremely time consuming. For example, a chemist experienced in the art of mix making and armed with proper tools and carefully chosen ingredients was able to make

up to one solvent dispersed ink per hour, but the same chemist was only able to make one molten wax mix per three hours. The additional time required corresponded to the added energy necessary to melt the binder ingredients. Generally, in these systems, the experimenter qualitatively found that more energy was required to melt the binder ingredients for molten wax mixing than to disperse pigment and binder ingredients for solvent dispersion wax mixing.

An important factor in mix making, which may force the ink to be formulated as a solvent dispersion, is the mixture's viscosity when in the molten state. For many of the resins used in wax inks, the higher the resin content, the higher the molten viscosity. As stated earlier, above its T_g, a resin becomes rubbery. Once the temperature increases sufficiently above T_g, the material enters a state of viscous flow. The further above T_g, the less viscous the flow. Even in its least viscous state, the resin binder is often of too high a viscosity for practical molten state coating. It is for this reason that resin based ribbons are coated exclusively as solvent dispersions. Depending on the ratio of wax to resin in a blended binder system, molten state coating may or may not be possible. Summarizing, because of this viscosity issue, it is possible to coat a wax ink either by solvent dispersion or molten state methods; it is not necessarily possible to coat wax-resin blend inks by molten state methods; and it is not possible to coat resin inks by molten state methods. The desire for design flexibility and time considerations led to the choice to formulate inks using solvent dispersion methods.

Two types of solvent dispersion methods were investigated. The first of the two techniques utilized both the hydrocarbon solvent toluene and the polar organic solvent isopropanol (IPA) as the dispersing agents. These low-molecular weight organic liquids were completely compatible with the wax-resin blend binder, allowing the binder ingredients to completely dissolve in the solvent. The solvent-binder mixture constituted one liquid phase. Pigment was dispersed directly in the blend to form a second, solid phase that was totally encapsulated by the liquid. Dispersions of this type are generally referred to as a solvent dispersions and are characterized by their high volatile organic compound (v.o.c.) content. It was found to be relatively elementary to produce highly stable dispersions using this method. The greatest drawbacks of this method were found to be the handling and disposal of the v.o.c.'s. Indeed, handling of v.o.c.'s is not a trivial issue; the Occupational Safety and Health Administration (OSHA) is leading the coating industry away from solvent dispersions having high v.o.c. content.

The second of the two dispersion techniques employed a mixture of water and a small amount of the polar organic solvent ethylene glycol as the dispersing agent. Although water was not the sole component comprising the dispersing agent, this type of formulation falls under the general category of aqueous dispersions. To formulate an ink using the aqueous dispersion technique, the waxes and resins had to be forced to either dissolve or emulsify in water. Waxes and resins compatible with water formed the first

continuous phase; emulsified solid waxes (particle size < 1 μm) formed the second *incompatible* phase; and dispersed pigment formed the third independent phase. The task of wetting all pigment and solid wax/resin particles in the second and third phases was found to be as difficult as finding an ingredient to aid the dispersion of resin in the first phase. While such formulations were much more difficult to stabilize, the benefits of low v.o.c. content far outweighed the drawbacks, and it was decided that aqueous dispersion methods would be used throughout the research.

Dispersing carbon black pigment is not a trivial task. While a Lightnin' Mixer provided the energy necessary to disperse the ingredients, much additional effort was put into the determination of optimal vessel diameter, fluid height, and impeller size, shape, and rotational speed. Even with these determinations made, some of the wax-resin inks were more difficult to produce than others. Two main factors pertaining to binder chemistry were found to govern ease of pigment dispersion and wetting:

- mix viscosity
- binder surface chemistry (surface tension).

Once these attributes were discovered, research was performed to determine acceptable upper and lower limits for each.

Mixes with higher viscosities tended to allow more complete pigment dispersion due to the higher level of shear produced during the mixing of these inks. All successfully designed systems incorporated binder ingredients

able to encapsulate pigment aggregates. It was therefore important for the waxes and resins comprising the binder to be of lower surface tension (γ) than the pigment aggregates. In order to assure this was the case, various surfactants were investigated before an anionic fluorosurfactant was decided upon. An anionic surfactant was chosen over the non-ionic, cationic, and amphoteric surfactants tested for a few reasons. By tuning the pH of the system, it was possible to raise the efficiency of the anionic surfactant to quite a high level while keeping the amount added extremely low. Further, the anionic surfactant not only served the purpose of lowering γ of the binder system, but it also helped prevent re-agglomeration of pigment particles by imparting a negative charge to the surface of the aggregates. All ribbons contained a small amount of this additive to increase the binder's ability to wet the pigment. This topic is discussed with much greater detail in section 4.2.2.

3.3 Ink Ribbon Coating Technique and Drying Decisions

All wax inks made, regardless of composition or dispersion type, were coated onto the poly(ethylene terephthalate) (PET) substrate by the well-known Meyer rod draw-down method. This coating technique was chosen due to of the ease of application, coating weight flexibility, and quick clean-up relative to other experimental coating procedures. Other methods investigated included spin coating and mini-pilot coater offset gravure. While both of these methods offered the potential for increased coating

weight uniformity, they were judged impractical because of their lack of coating weight flexibility and necessarily high preparation and clean-up times.

Drying conditions were found to be of utmost importance to image quality and varied from coating to coating. In all experiments, drying was accomplished with forced hot air, through use of a Precision Scientific 625 drying oven. In the coating industry, for matters of practicality, it is necessary to speed the drying process. For both solvent and aqueous dispersed ink coatings, efficient removal of the liquid phase was only possible through such drying techniques. A good deal of time was spent investigating drying conditions. It was found that the drying profile was critical, in that drying a film for too short a period or at too low a temperature resulted in a soft, tacky wax ink. Drying a film for too long a period or at too high a temperature resulted in a wax ink that would not release from the PET substrate. Suitable drying times for 8.5" x 11" draw-downs were in the neighborhood of one and a half minutes; temperatures were around 85 °C.

In order to evaluate the quality of the wax ink ribbons produced, an image processing algorithm was specially developed using image analysis techniques to detect void areas and streaks in the pigmented coatings. First, an 8.5" x 11" area was scanned at 75 samples per inch and eight bits of gray. After thresholding at a predetermined optical density, the algorithm then computed the total area occupied by voids and streaks. This area was presented as a percentage of the total coated area and reported as Coating

Quality (CQ). The CQ metric allowed objective measurement of the degree of success achieved after the coating step was performed but before the material was imaged. CQ is discussed with greater detail in section 4.4.

3.4 Ink Ribbon Physical Design Decisions

From a process engineering standpoint, the ideal ribbon would consist of one layer of wax ink coated onto the PET substrate. Laws of coating process control dictate that complex coatings lead to difficult process control issues. Naturally, processes that require a great deal of effort to control are more expensive to maintain. While many DT2 ribbons are single layer designs, many others consist of multiple layers despite the added production risk. Because the design goal of the project was to yield high quality images at the fastest throughput possible, multi-layer designs were not ruled out. First, however, single layer designs were investigated extensively.

The initial sixty or so experimental ribbons consisted of pigmented wax ink draw-down coated directly onto PET and dried in the previously discussed manner (section 3.3). Results of these experiments showed that release from the substrate during printing was somewhat inhibited for ribbons having the best pigment dispersions and the highest coating quality. Indeed, for some of these early ribbons, the PET substrate raised above its T_g well before wax transfer of any sort took place. Single layer wax inks that released easily from the substrate tended to suffer from poor coating quality and poor ink-receiver adhesion. Lowering γ of the wax/resin binder to aid pigment wetting also

aided the adhesion of the wax ink to the PET substrate, a trade-off manifesting itself in decreased transfer efficiency. Conversely, when γ was raised to lower the adhesion to the PET, thereby increasing release properties, poor dispersion quality resulted. Because of the aforementioned design goals of the system, it was decided that rather than falling pray to a multi-objective optimization (compromise) at such a low level, it would be worth the added design effort to develop a multi-layer solution. In hopes of simultaneously optimizing PET release characteristics, dispersion quality, and ink-receiver adhesion, multi-layer designs were subsequently investigated.

The decision to coat two layers of wax onto the substrate immediately opened up doors that previously had not even existed. Most importantly, the multi-layer coating allowed simultaneous optimization of uniform release from the substrate and adhesion to the receiver. Of course, adding a release layer doubled the amount of formulation work required, partially offsetting the benefits. Initially, the release layer contained the IR absorbing pigment; however, experimentation proved that decisions made to insure adequate pigment dispersion conflicted with the requirements of optimal release. Once this was realized, the release layer was formulated with only two objectives:

- coat onto the substrate with high uniformity
- aid uniformity of release from the substrate at a relatively low temperature.

Constraints on tensile strength rested on the pigmented wax-resin layer -- the release layer was formulated to have low tensile strength, leaving the window wide open for optimization in the outermost layer.

The thermal efficiency of the release layer was directly related to its thickness. Therefore, the physical structure of the release layer was optimized by minimizing its thickness while maintaining high coating uniformity. The release layer was further optimized by leveling its surface tension with that of the PET, so that γ_{PET} was only slightly greater than γ_{RL}. Figure 3.4.1 presents a cross-section of the basic ribbon design. The release layer was coated onto the PET first. After drying the release, the pigmented layer was coated onto the release layer and the ribbon again placed in the oven. Because the outermost layer contained the pigment sensitive to the 1.064 μm laser radiation, it was subsequently referred to as the photothermal conversion layer (PCL).

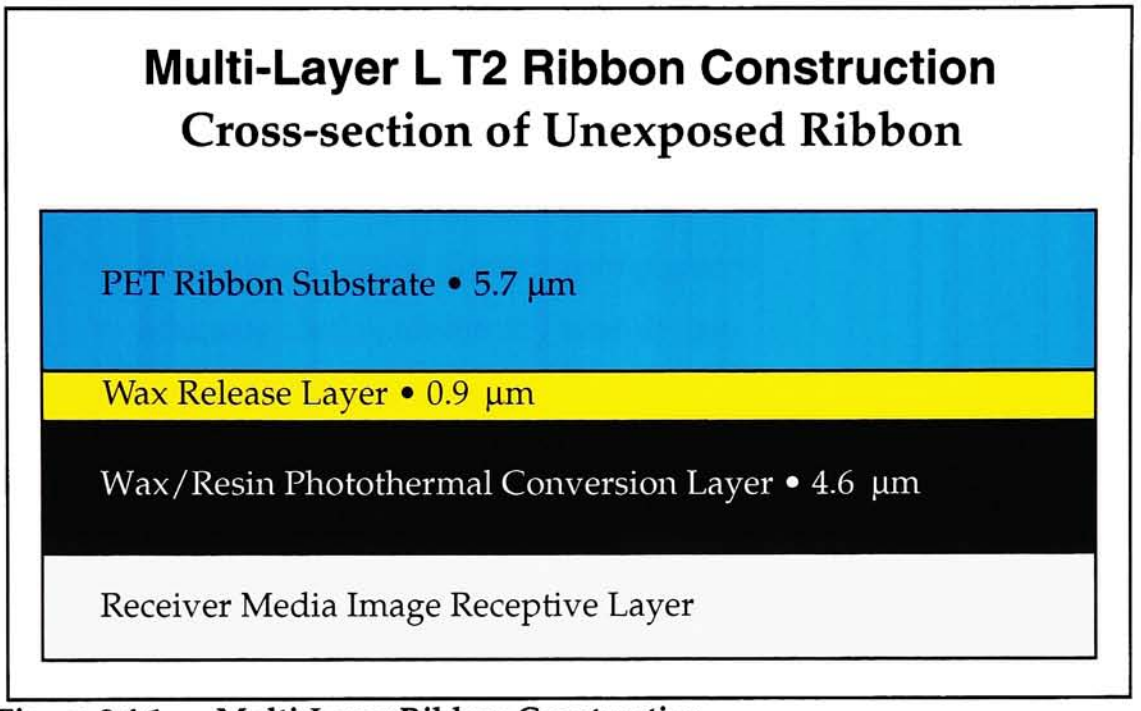

Figure 3.4.1 ~ Multi-Layer Ribbon Construction.

3.5 Ink Ribbon Formulation Design and Optimization

With fundamental decisions of construction, coating, and drying made, an exhaustive series of screening experiments ensued. The purpose of these screening experiments was to probe the design space in order to determine the basic formulation which would then be optimized. All of the PCL inks formulated consisted of the following basic ingredients:

- pigment
- wax binder(s)
- resin binder(s)
- viscosity modifier
- surfactant.

Many combinations of different ingredients were investigated before a suitable formulation was found. The constraints placed on these experimental PCLs included:

- compatibility of components with one another
- adequate and stable dispersion of pigment
- adequate coating uniformity after drying
- no repellancies in coating
- printable with laser exposure system.

While none of these attributes were optimized at this point, it was found to be relatively difficult to combine a set of ingredients in such a way so that all of the above criteria were met. After countless trials, the decision was made to use powdered pigment mixed with a polyethylene/paraffin wax emulsion, a styrene acrylic polymer emulsion, a styrene acrylic polymer latex, a poly(vinylpyrrolidone) (PVP) dispersion, and an anionic fluorosurfactant. The ingredients were dispersed in water and ethylene glycol.

3.6 Modeling / Optimizing System Exposure Parameters

With all fundamental decisions regarding exposure system and ribbon design made, it became possible to develop a mathematical model of the system. A closed form solution to the three-dimensional Fourier Heat Equation proved to work very well as a tool to increase understanding of the system. The model incorporated such parameters as:

- laser spatial pulse height, shape, and size
- laser temporal pulse shape

- wax ink heat capacity
- wax ink layer thickness
- optical blurring of the laser pulse caused by PET and release layer.

Once formulated mathematically, the equations were coded in Wolfram Research's Mathematica for efficient evaluation and analysis. Numerical integration of the model equation yielded the temperature at a chosen point given some set of input parameters.

The model, discussed with great detail in section 4.3, was used primarily to predict the outcome of hypothetical input scenarios. It was ideally suited for evaluations such as these, where relative comparisons were of greatest importance. By evaluating the relative effects of the various input parameters, the model aided greatly the optimization process; especially around the laser exposure system. The model provided insight, predicting what variables and interactions were key and what variables governed only higher order effects.

3.7 Measuring the Quality of Output Produced

In order to evaluate the ribbons produced, key response variables had to be defined and subsequently measured. Image analysis techniques provided a means to quantify output quality. It came as no surprise when it was found that a prerequisite of acceptable image quality (IQ) is acceptable coating quality (CQ). Undulating coating thickness, repellancies, and large pigment aggregates all increase the noise level of the imaging system. Digital

microscopy and digital image analysis (DIA) were first employed to determine the quality of pigment dispersion for a general PCL formulation. Once acceptable dispersion quality had been obtained, an image analysis algorithm was developed to quantify the coating quality of a particular ribbon formulation by looking for repellancies (sometimes called "craters") and large variations in coating thickness. The algorithm, discussed in greater detail in section 4.4, operated on an image acquired via a backlit flatbed scanner. The image mapped to an 8.5" x 11" section of ribbon sampled 75 times per inch. The algorithm employed thresholding, binary morphological filtration, and area computations to output a number corresponding to the percent defect area of the image. The technique proved to be highly a repeatable means of producing a variable CQ measurement system whose output decreased as coating uniformity improved.

While high image quality required a low CQ, a ribbon formulation yielding a low CQ didn't necessarily mean high image quality would follow. Many PCL formulations coated beautifully but failed to produce acceptable image quality. An example of such a scenario was an early case in which the release layer contained a surfactant to such a degree that the surface tension of the mixture was lowered far beyond that of the PET substrate. With an ink formulation of appropriate γ applied to the release layer, the sample yielded a high CQ but would not image under any conditions. Of course, the acid test was to print any sample of adequate CQ and quantify the results.

The imaging system was developed and optimized for halftone printing. An image analysis system and a more-or-less conventional DIA algorithm (discussed with greater detail in section 4.4) was designed to quantify various properties of printed halftone dots. The precision of the algorithm greatly aided the refinement of the system. The IQ measurement system showed that in order to yield consistent IQ values over sample replication, it was necessary to refine various aspects of the coating and imaging processes. Large pigment aggregates were removed through use of a centrifuge, platen vacuum pressure was increased, and a more uniform substrate was chosen. Once such necessary refinements were made, a sample's IQ was categorized using a weighted combination of dot size, shape and placement accuracy.

3.8 Optimizing the Photothermal Conversion Layer (PCL)

With the imaging system's operational parameters well defined and ribbon construction and receiver chosen, it became possible to optimize the formulation of the PCL. For this process, all other factors were held constant, including:

- the set of exposure conditions
- PET substrate
- release layer composition and coating weight
- PCL coating weight.

The large number of screening experiments leading up to the prototype formulation not only served as a means to obtain this initial design, but also

helped to define what ingredients in the formulation would affect IQ the most. Materials to be included in the formulation optimization process included:

- thermoplastic wax emulsion
- thermosetting resin dispersion
- thermoplastic resin latex
- thermoplastic resin emulsion.

Pigment and surfactant levels were held to constant percentages of the mix. In order to optimize these variables, a good understanding of the design space was necessary.

Initially, a series of PCLs was formulated to probe the limits of the space; however, to most efficiently map out the space, a factorial experiment series was required. Many experiment series types were investigated before a 2^4 central composite response surface design was chosen. The basic design was further augmented with a star, which added ±2 levels. Axial distances and locations were carefully chosen so that the design would be both rotatable and orthogonal. Because of its rotatability, replications were made at the center point and variances were computed based on a point's distance from the center. By replicating the center point 12 times, a robust estimate of variation was obtained. The center point was adjusted so that each -2 level required very small amounts of the corresponding ingredient.

For every formulation produced, a ribbon was fabricated and CQ and IQ were determined. These results were analyzed with Manugistics Statgraphics, version 7.0, which aided the computation of ANOVA statistics. Various Statgraphics tools were used to evaluate the effects of the components and their interactions. Regression coefficients were estimated to fit the following model:

$$IQ = \hat{\beta}_0 + \sum_{i=1}^{k} \hat{\beta}_i x_i + \sum_{i=1}^{k} \hat{\beta}_{ii} x_i^2 + \sum_{i,i<j} \sum_{j} \hat{\beta}_{ij} x_i x_j \qquad (1)$$

where $\hat{\beta}_i$ are regression coefficients and x_i are the independent input variables. Given the regression coefficients for the first and second order effects and first order interactions, the model of the design space could be cast as an objective function. The optimum point of the objective function was determined through use of a C program employing the *downhill simplex method* of Nelder and Mead (1965). This optimization technique is described in greater detail in section 4.5. In order to verify the result, the objective function was verified using *Brent's Method* (Brent, 1973). Several starting locations were investigated to assure the algorithm converged to the global minimum point.

The optimal formulation was used to produce many additional experimental ribbons which were used primarily in experiments involving the close scrutiny of other aspects of the ribbon production and imaging processes. These experiments led to the employment of several techniques further optimizing IQ. For example, a pressure roller mechanism was implemented to remove air bubbles at the interface between receiver and ink;

thorough investigation of a centrifuge technique led to the removal of large pigment aggregates; and a great number of LT2 images was produced in order to better understand the latitude of the developed LT2 process. Upon completion of these sub-projects, the experimenter had obtained a fundamental understanding of the designed LT2 process window. The laser imaging system proved viable and the optimal ribbon capable of high resolution.

4.0 Results

Once the above fundamental decisions were made, it became possible to engineer a system optimally suited for a given set of conditions. As would be expected for a desktop printing system, the main factors revolved around price point versus output quality. It is widely known that laser prices, as with many other high-technology goods, are falling while their performance continues to increase. Companies such as the Vixel Corporation (formerly Photonics Research, Incorporated) are continuously introducing affordable laser solutions for a variety of applications. A technology such as LT2, to be viable in the desktop printing market given its output quality, must take full advantage of these innovations in order to carry a price tag below $5,000. Using this logic as the primary constraint, the system was designed to use a modest amount of laser power while keeping throughput as high as possible. Each component of the system, engine, donor ribbon, and receiver sheet, were designed or chosen accordingly.

4.1 The Writing Engine

The engine used was based on a design originally intended for high power applications such as Laser Ablation Transfer (LAT) imaging. However, the desire to assemble a system that would have the potential for significant cost reduction greatly constrained the design effort. The engine and control electronics finally decided upon can be divided into several subsystems, each of which performs a set of functions critical to proper operation. Each of these

subsystems was designed to integrate efficiently with the other sections. Writing engine subsystems illustrated in Figure 3.1.1 include:

- laser exposure subsystem
- beam power modulation subsystem
- optical subsystem
- positioning subsystem
- measurement subsystem.

It is important to note that in a commercialized LT2 printer, paper and ribbon handling subsystems integral to those mentioned above would have to be developed. Design of the engine was accomplished by first gaining an understanding of each necessary component and then working with others knowledgeable in laser marking systems to assemble the components. The basic integrator involved was A•CAD•emic Solutions, Inc. of Santa Clara, CA; the chief consultant and designer of Rexam Graphics' LAT engine was Mark Doxtader, Polaroid Corporation. As is always the case in digital printer engine design, several configurations were evaluated before an adequate design was found. The following several sections summarize the componentry of the subsystems from technological aspects to the reasoning behind their selection for the LT2 imaging system.

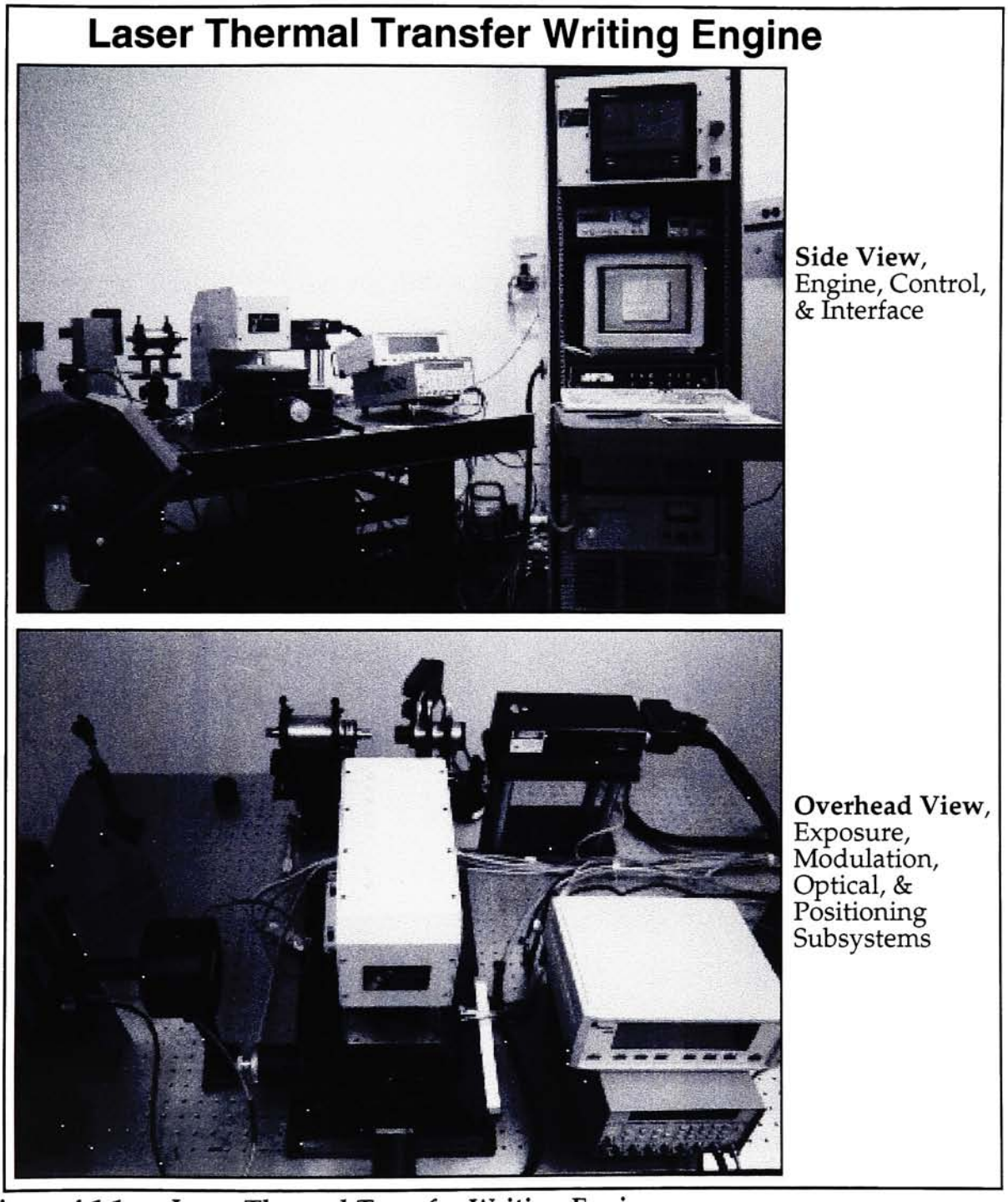

Figure 4.1.1 ~ Laser Thermal Transfer Writing Engine.

4.1.1 Laser Exposure Subsystem

A Spectra-Physics, Inc. Tightly Folded Resonator (TFR) diode-pumped laser system provided the novel means of thermal exposure necessary to drive the thermal transfer process. Comprising this subsystem were the head, power supply and controller, and the cooling system. Although initially purchased for high power applications, the laser head used was found to be well suited for employment in this system. Some of its features included highly stable emission characteristics, high efficiency, compactness, *hands-off* operation, and a wide power band offering great exposure flexibility. While a Q-switched mode was available, optimization for a low power, low cost system dictated that the system be used in continuous wave (cw) mode. Even so, the system provided stable output continuously from zero to 2.5 watts. The same optimization constraints dictated the system operate in the TEM_{00} mode, ideal for the TFR design.

Diode lasers have long been choice exposure mechanisms for desktop electrophotographic engines. In the case of the LT2 engine's Nd:YAG head, the laser diode combines characteristically "...high brightness, high efficiency, monochromaticity, and compact size in a near-ideal source for pumping solid-state lasers" (Spectra-Physics, Inc., 1992). The key to the efficiency of a pumped solid-state laser lies in the degree of mode matching achieved. Mode matching may be described as the maximization of the regional overlap of the active medium occupied by the pumping source and the volume of the active medium occupied by the desired laser mode (Siegman, 1986). In low power

pumped lasers, fiber lenses are used to focus the pump volume onto a volume of the active medium best matching the desired mode. Because the pump volume is focused onto the end of the active medium, these geometries are termed *end-pumped*. Such optical mode matching schemes are of low cost and sufficient for low power systems. Although a system of this type would most likely prove more than adequate for a conventional desktop laser printer, its temporal power stability would be in doubt for a high resolution, variable exposure printer.

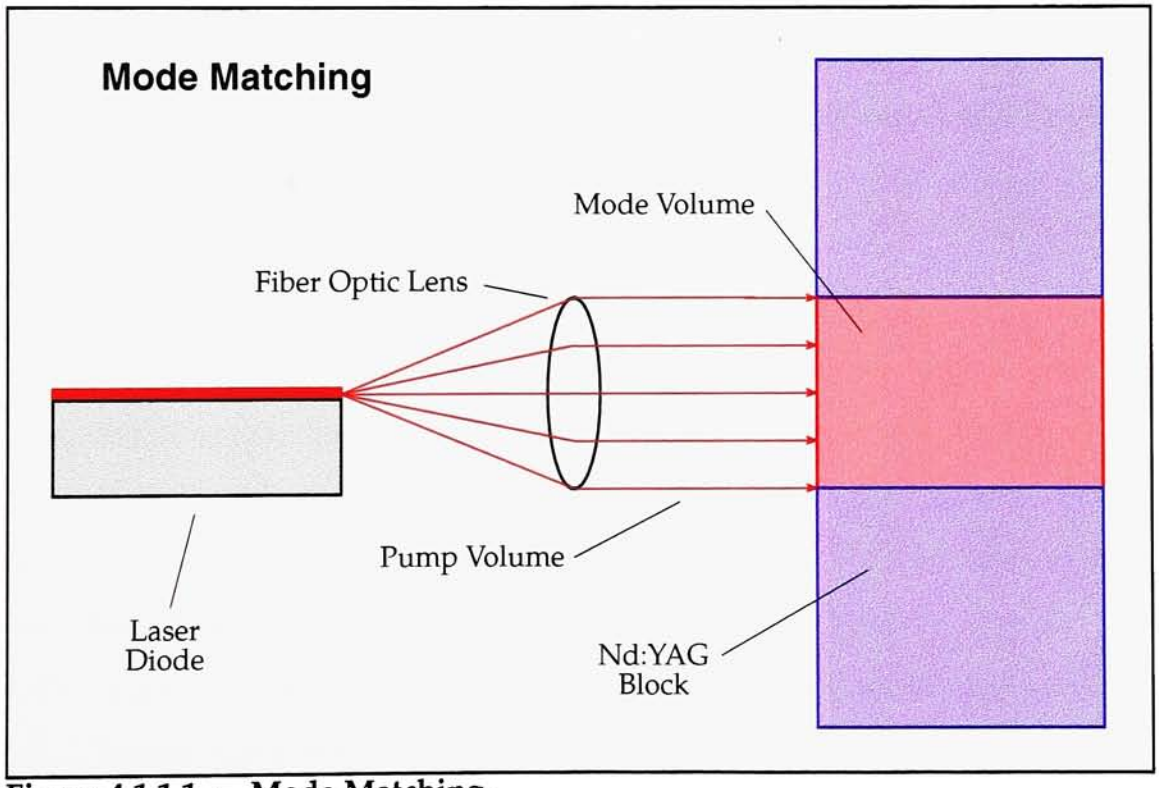

Figure 4.1.1.1 ~ Mode Matching.

In order to increase the power of such a system, laser diode size must be increased; however, doing so also increases its spatial emission region. In order to mode match to this increased region, the radius of the active mode volume must also be increased. Unfortunately, increased mode radius results in a higher lasing threshold. To avoid this problem, some systems employ multiple laser diodes, multiplexed together and focused onto the active medium. This approach is complex and cost prohibitive in terms of fabrication and alignment. Laser diode bars, comprised of several diodes residing on a monolithic semiconductor chip, solve this problem to some degree. Although the diode fabrication process is simplified, optically focusing this high intensity onto the end of the active medium results in low reliability from high thermal stress and a relatively wide effective emission region upon which to match the mode volume.

TFR designs utilize laser diode bars in a much more efficient manner. By carefully optimizing the spacing of the diodes on the semiconductor wafer, the device may be set up so that the TEM_{00} beam path in the active medium maximizes the overlap of the excitation volumes. Figure 4.1.1.2 demonstrates how this efficient mode matching geometry may be achieved. In this configuration, "...the folded resonating cavity allows each diode of the diode bar to be in a quasi-end-pumping mode without requiring the laser mode diameter to increase. The heat load in the active medium is spread over multiple points, eliminating the problem of thermal fracture of the laser medium" (Spectra-Physics, Inc., 1992). Additionally, the laser mode diameter

is relatively small, yielding a very high cw gain. Efficiency of such systems commonly exceeds 40%. (Spectra-Physics, Inc., 1992)

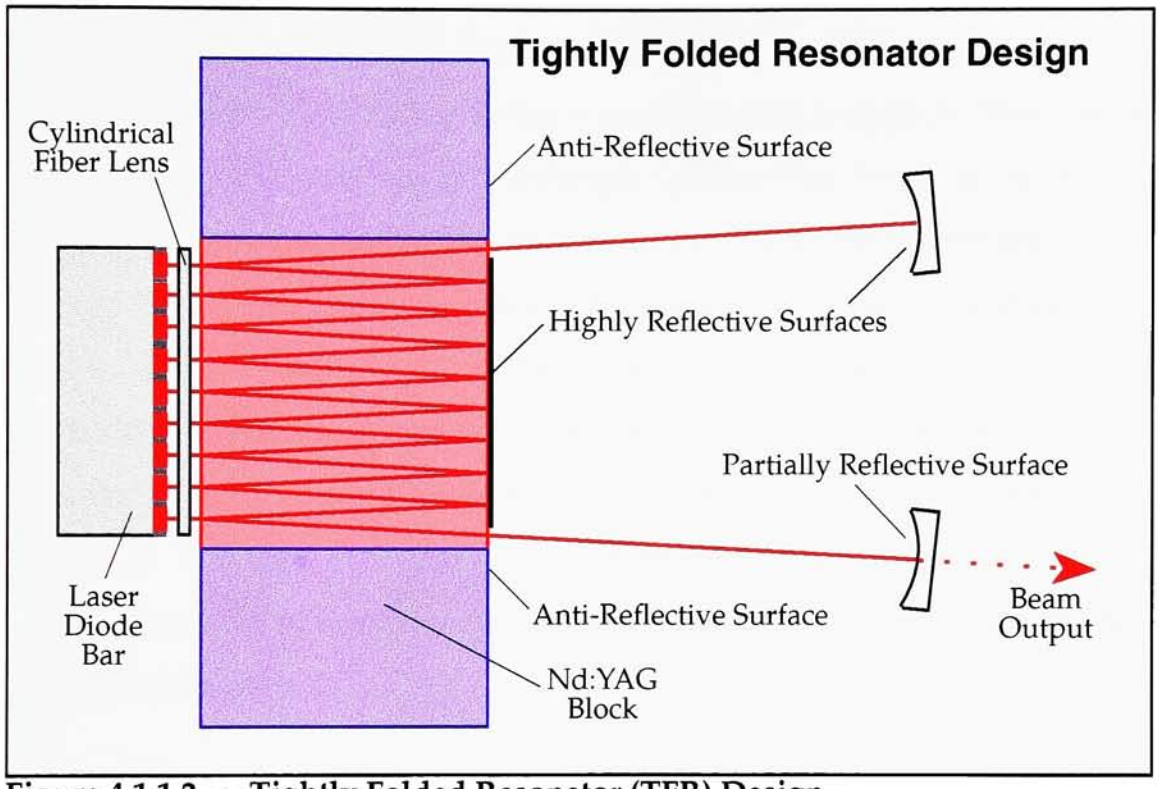

Figure 4.1.1.2 ~ Tightly Folded Resonator (TFR) Design.

The Spectra-Physics, Inc. Nd:YAG system contains an array of 12 AlGaAs 1 Watt diodes, each of roughly 250 μm square area. At one absorption length (about 1 mm), their projected area expands to roughly 250 x 320 μm. Spacing and dimensions are optimized so that the TEM_{00} mode completely fills the pump region. The diode bar is collimated via cylindrical fiber lens and coupled to a block of the active medium, a slab of Nd:YAG. The faces of the slab parallel to the bar are highly polished. The side opposing the diode bar is

coated with a highly reflective material at the laser wavelength directly opposite the diodes in order to provide total internal reflection (TIR) conditions at the interface. To either side of the polished surface, an anti-reflective coating is applied so that the beam may exit. At the interface between the slab and diode bar optics, a special coating is applied. This coating is highly reflective at the lasing wavelength (greater than 99.9%, as reported by the manufacturer) and highly transmissive at the pump wavelength (about 98%). An anti-reflective coated fiber optic cable is used to collimate the diodes. The manufacturer claims the numerical aperture to be greater than 0.5, which is "...sufficient to capture and collimate all of the laser diode bar emission in the direction transverse to the diode junction" (Spectra-Physics, Inc., 1992). Setting the fold angle to match the divergence of the beam, about 7°, facilitates both mode matching close to the diode bar as well as toward the center of the beam.

As in conventional laser designs, the highly reflective mirror and output coupling optics are tuned so that the intracavity TEM_{00} mode reflects between the two sides. "By choosing the angle of reflectance such that the vertices coincide with the centers of the diode pitch, an optimized overlap of pump volumes excited by the laser diode bar and the TEM_{00} of the solid-state laser results" (Spectra-Physics, Inc., 1992).

As reported by the manufacturer, the effective gain of each AlGaAs diode is about 30%. Calculating the system gain G_S conventionally yields the following:

$$G_s = \exp(12 \times 0.3) \cong 37. \quad (1)$$

The power gain of the system is defined as 10 log G_S, which is about 15 dB. In order to maximize this gain, the diode bar is temperature-tunable. By thermoelectrically cooling the diode wafer, the output wavelength may be optimized so that it matches the absorption band of the YAG laser slab. The optimization process is known as power tuning. By measuring laser power output as a function of diode temperature, a curve may be generated for a particular diode current setting. A family of curves results from repeated measurements at various input currents. Linear regression through the maxima of these curves yields the Power Tuning Curve for the laser. The Power Tuning Curve equation for the laser used was calculated to be:

$$T_{Diode} = [-0.5(I_{Diode} - 10.0 Amps) + 25.5]^{\circ}C \quad (2)$$

where T_{Diode} is the temperature at which laser output power is maximum and I_{Diode} is the operating current. Figure 4.1.1.3 shows the curves obtained experimentally. These results agree with the operating conditions suggested by Spectra-Physics, Inc. Once the operating temperature has been selected, an internal feedback loop provides control to within 0.01 °C. Note that the temperature dependence is not high, in that a shift in temperature plus or minus one degree of the optimum set point results in power losses less than five percent. Such a trait is important in the design of a commercial system.

The laser could be controlled with a feedback loop driving cooling fans and delay cycles as necessary.

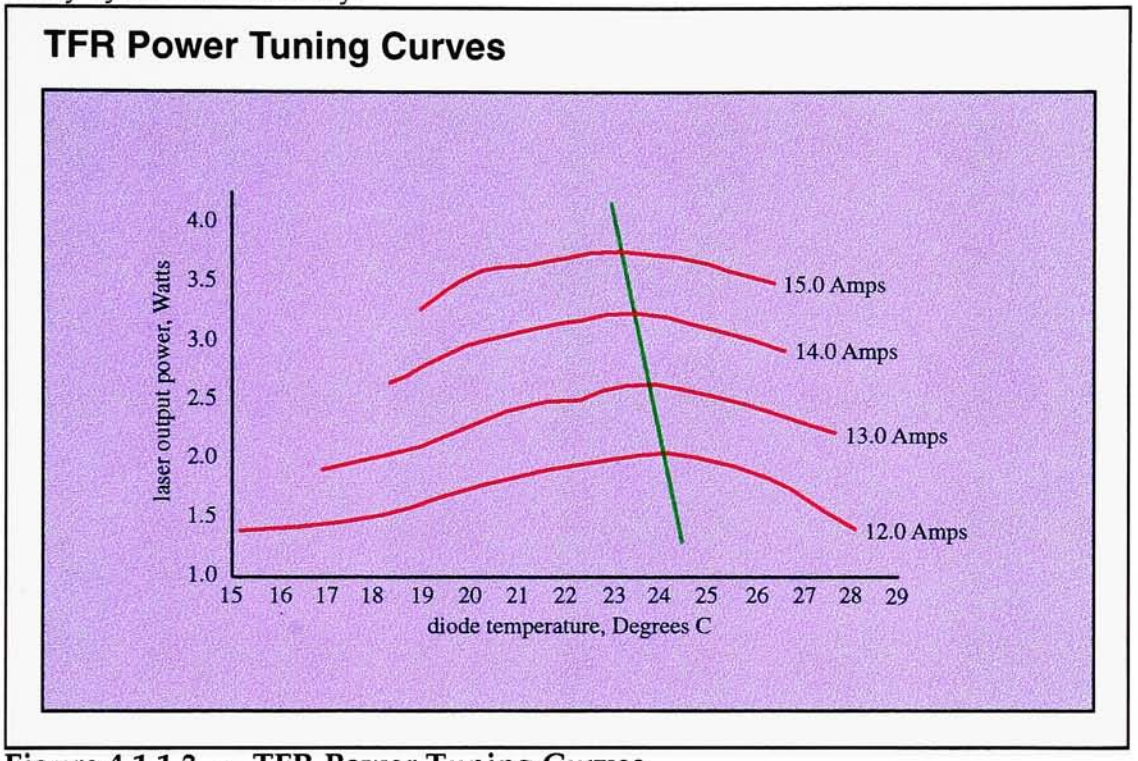

Figure 4.1.1.3 ~ TFR Power Tuning Curves.

A final strong point of the TFR design is its sharp characteristic pulse shape. Because a raster system was designed rather than a vector system, it was important to maximize both spatial *and* temporal acuity of the laser pulse. Optimization in both domains was necessary in order to form the sharpest dots possible. A laser having a broad temporal pulse profile would yield blurred dots at all but the slowest recording speeds. As Figure 4.1.1.4 illustrates, rise to maximum and the return to zero intensity may take place as quickly as 10nsec with a TFR laser. With temporal pulse envelopes on the order of 90 µsec, the shape formed by the Spectra-Physics, Inc. laser was nearly

a perfect rectangle. As noted elsewhere, such a shape greatly simplified mathematical model calculations.

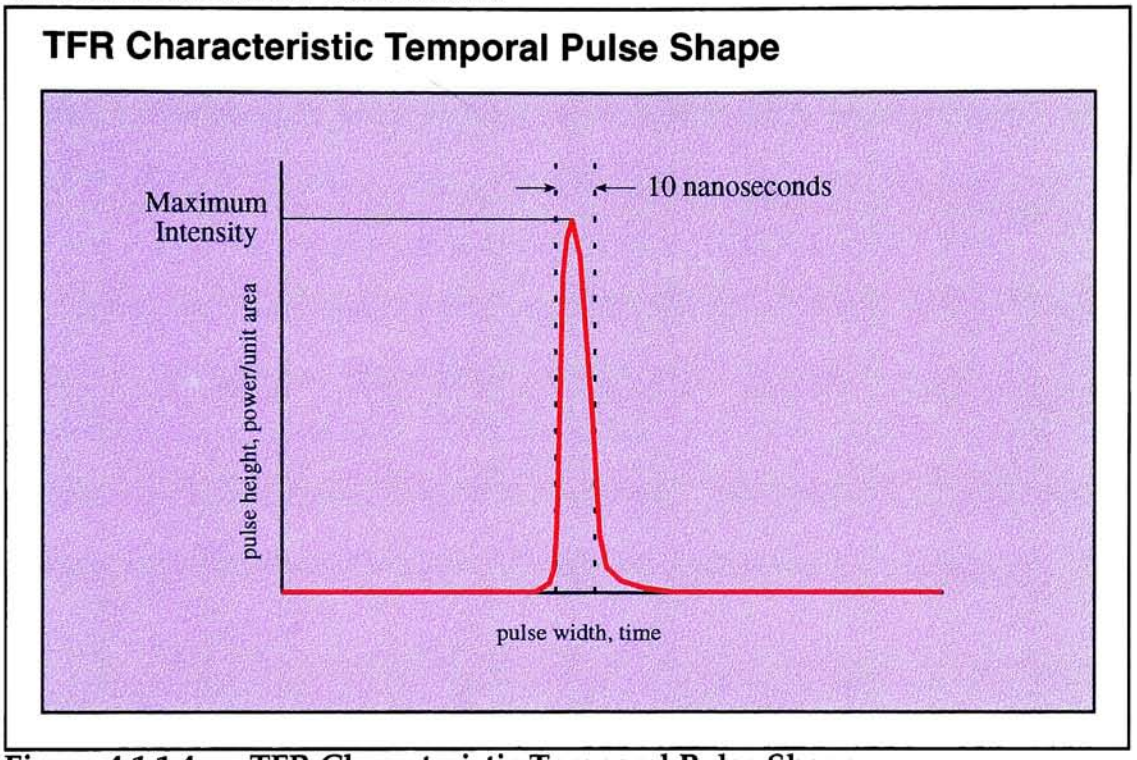

Figure 4.1.1.4 ~ TFR Characteristic Temporal Pulse Shape.

The head was driven by a Spectra-Physics, Inc. 80C31 microprocessor controlled power supply and controller. An internal analog power source provided the voltages and currents necessary to drive the laser. The function of the controller was to provide and maintain on demand a constant laser power output by monitoring and maintaining the operating temperature for a given current.

4.1.2 Beam Power Modulation Subsystem

An electro-optic modulator (EOM) provided a precise means by which to attenuate the dc laser output. Although there were less complex and less expensive modulation systems available, the electro-optic method was chosen on the basis of its high efficiency and dynamic response characteristics. For modeling purposes, it was important that the pulse temporal profile remain as near rectangular as possible; from a radiation modulation standpoint, the EOM assured this would be the case. System flexibility also played a major part in the decision. While much less expensive lasers and modulators exist, to choose one such limited alternative at the onset of the project may have proven fatal in the long run. Only after all optimization criteria were met (including cost factors) was cost *reduction* considered.

The Conoptics, Inc. 362 Electro-Optic Modulator employed was of a conventional design, utilizing the Pockels effect. The device included a quarter-wave plate and an electro-optic crystal placed between crossed polarizers (one vertically oriented and the other horizontally oriented). By passing a substantial current density through the bulk L of an electro-optic crystal, circularly polarized light from the quarter-wave plate could be resolved into eliptically polarized light. The polarization of this emergent light may be represented by two vector components x' and y', plus and minus 45° from the incident angle of polarization. Following the electro-optic crystal with an analyzer allows only the portion of x' and y' parallel to its orientation to pass. Figure 4.1.2.1 illustrates this phenomenon.

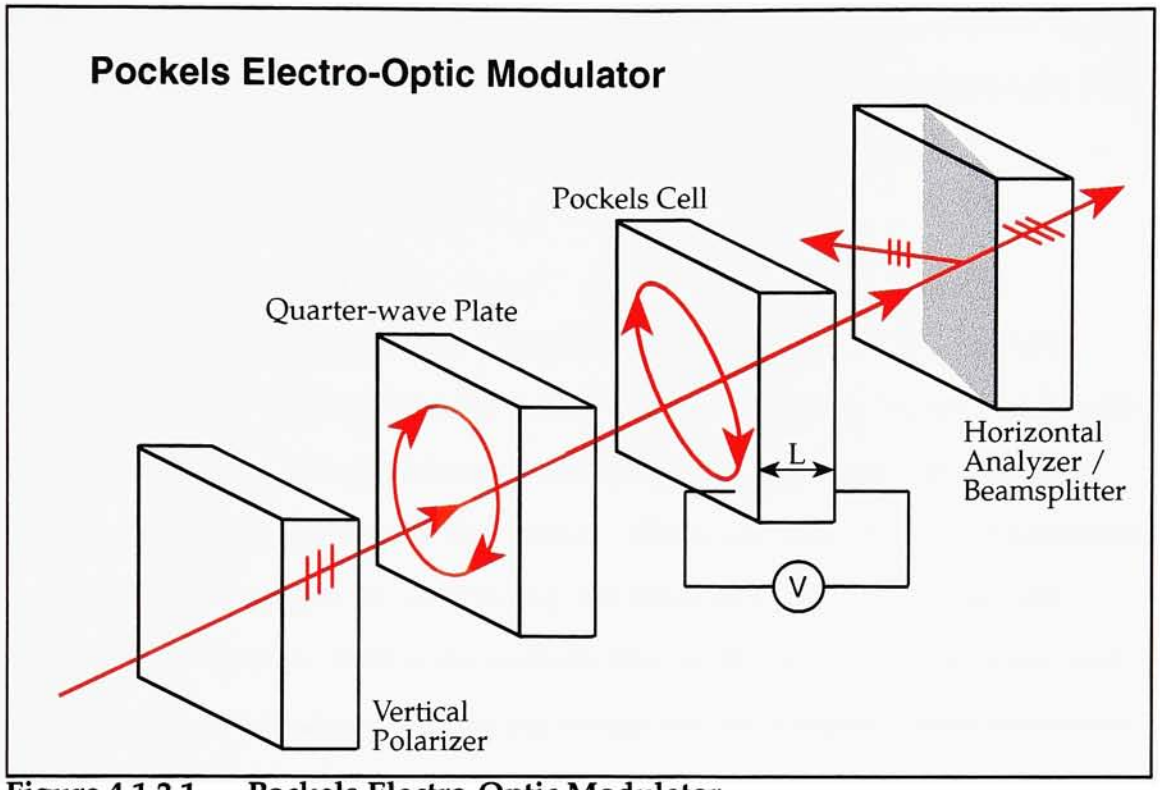

Figure 4.1.2.1 ~ Pockels Electro-Optic Modulator.

Varying the current to the electro-optic crystal varies the output of the modulator. By replacing the analyzer with a beamsplitter/analyzer, the rejected component may be directed to a detector and run through a feedback loop. It was in just this manner that the Conoptics, Inc. 362 EOM functioned.

Driving the EOM power supply was a Stanford DG535 Digital Delay/Pulse Generator (Stanford Research Systems, Inc.). The precision of the digital pulses insured a rectangular temporal pulse would be sliced from the laser beam. The width of the pulse correlated directly to the temporal duration of the output laser pulse. The height of the pulse was proportional

to the intensity of the output laser pulse; that is, it was possible to slice any lower amount of power from the 1.5 cw max. laser source. A Tektronix 2440 Digital Oscilloscope was used to monitor these driving pulses.

4.1.3 Optical Subsystem

Components comprising the optical subsystem included a Faraday Isolator, an aperture stop, and the focusing objective, as can be seen in Figure 3.1.1. Additionally, plane mirrors were used to fold the beam 90° at three locations in order to compact the system. Great care was taken in maximizing laser beam throughput by optimizing the alignment of each component relative to all others. Both a photodiode and an IR viewing scope were used to monitor beam propagation during set-up and on a regular basis thereafter. Measurement procedures are discussed with greater detail in section 4.1.5.

Each component of the subsystem served a specific purpose; any piece not completely necessary to realize a high quality beam was removed in the interest of simplicity and cost savings. For example, the aperture stop, an adjustable multi-blade unit obtained from Newport Optics, served specifically to block any diverging components of the beam. In an effort to keep optical efficiency as high as possible, the number of optical components in the beam path was kept to an absolute minimum. The 1" focal length single element beam focusing objective was of double convex spherical design, and was supplied by A•CAD•emic Solutions, Inc. Although a simple focusing arrangement, the objective proved to work quite well in both imaging the

Gaussian profile sharply at the exposure plane and absorbing a minimum of the laser's radiation. The objective was focused manually via PC interface to a small z-axis drive motor (American Precision Industries, Inc., Buffalo, NY). Focus was monitored through use of a BeamScope Optical Profiler (Dataray, Inc.), which is discussed with greater detail in section 4.1.5. A plot of z-axis lens position vs. beam width is presented in Figure 4.1.3.1.

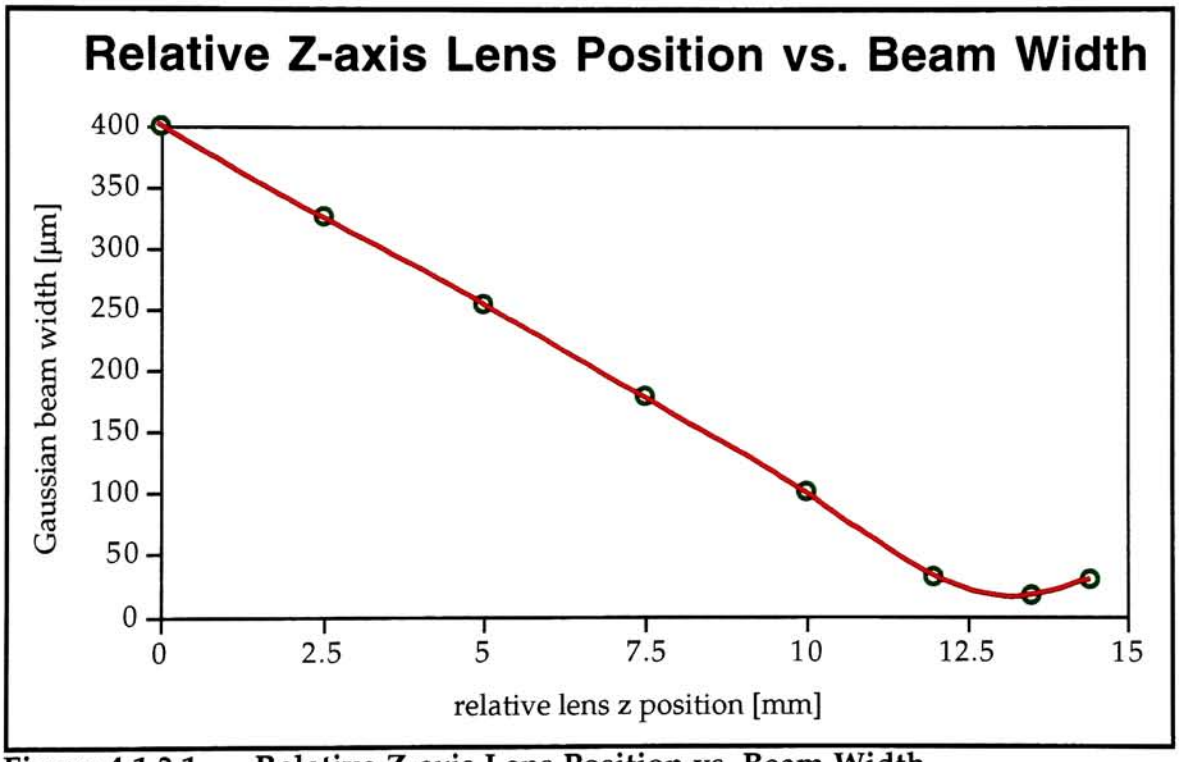

Figure 4.1.3.1 ~ Relative Z-axis Lens Position vs. Beam Width.

By measuring the beam width as a function of the lens position, it was a simple task to bring the beam into focus. Interestingly, the beam maintained better than 92% Gaussian fit, as calculated by the BeamScope, over the range presented in the above graph. The ease with which proper focus was

achieved contrasted with the difficulty of isolating the laser from optical feedback.

The optical isolator, found to be a necessity for development work, was the most unique piece of the subsystem, and was by far the most cumbersome and difficult to configure. Not surprisingly, in the early stages of system design, an optical isolator was not considered. Indeed, the first operational prototype did not include any type of optical isolation device. It was only after initial exposures were made that it became apparent power was being lost internally to the system at some point. Intensity measurements originally performed by Mark Doxtader (Polaroid Corporation) with the aforementioned photodiode confirmed a loss of approximately 35% percent between the laser beam exit aperture and the exposure plane. The cause for this loss was determined to be feedback, or back-propagation from optical components in front of the laser and the ribbon itself. Minute reflections back into the laser cavity were causing interference in the pumping process thereby reducing lasing.

Magneto-optic devices are very stable and require no applied current to operate, compared to electro-optic devices employed for similar purposes. For these reasons, a Conoptics, Inc. Model 711 Faraday Rotator was employed to isolate the laser from optical feedback. The Faraday effect concerns the change in refractive index of an optical material placed under the influence of a magnetic field. "Faraday found (1845) that when a beam of plane polarized

light passes through a substance subjected to a magnetic field, its plane of polarization is observed to rotate by an amount proportional to the magnetic field component parallel to the direction of propagation" (Wilson et al, 1989).

A Faraday Rotator relies on this magneto-optical effect, utilizing a strong permanent magnet and an adjustable glass element with a high Verdet constant to deflect the reflected component of a beam of light. The Verdet constant V is unique to the particular material selected and can be closely approximated by:

$$V = \frac{a\lambda^2}{(\lambda^2 - b)^2} \qquad (1)$$

where a and b are constants intrinsic to the chosen material (Conoptics, Inc., 1991). For example, at 589.3 nm, the V for crown glass is 6.4, while V for Zinc Sulfide (ZnS) is 82 (Wilson et al, 1989). Although ignored in the above approximation, the Verdet constant is a weak function of temperature. A Faraday Element produces rotation θ according to:

$$\theta = V_\lambda \int_0^L H_x dz \qquad (2)$$

where H_X is the local magnetic field strength. By moving the element further into and out of the local magnetic field, the degree of rotation may be altered. Note that the dependence on a magnetic field assures that the Faraday Rotator is *uniquely non-reciprocal*. When an axial magnetic field is applied, the element rotates the orientation of through-traveling light; however, unlike materials with intrinsic rotary properties, the direction of polarization rotation *or handedness* is dependent on the propagation direction relative to

the applied field. In plain terms, a left handed beam of light moving through the device becomes right handed if reflected back.

By combining this unique tool with a polarizer, an Optical Isolator may be configured. Figure 4.1.3.2 illustrates the basic Optical Isolator. Light propagates through a linear polarizer configured to transmit the vertically polarized component. Following the polarizer is a Faraday Element set up to cause an exact 45° rotation. Transmitted light moves through the Faraday Element, is rotated, and continues its path toward the focal point. Axial feedback caused by optical components in the beam path (such as dust, the aperture stop, the focusing objective, or even the ribbon) reflects back through the Faraday Element. The unique element *adds to, rather than cancels, the rotation* on the polarized beam, causing horizontally polarized light to exit toward the polarizer. The vertically oriented polarizer denies passage of the reflected component, eliminating optical feedback. "The degree of isolation is determined by three factors: residual reflections from elements in front of the Faraday Element and the first surface of the Faraday Element itself, the extinction ratio of the polarizer, and the precision, of the 45° rotation" (Conoptics, Inc., 1991).

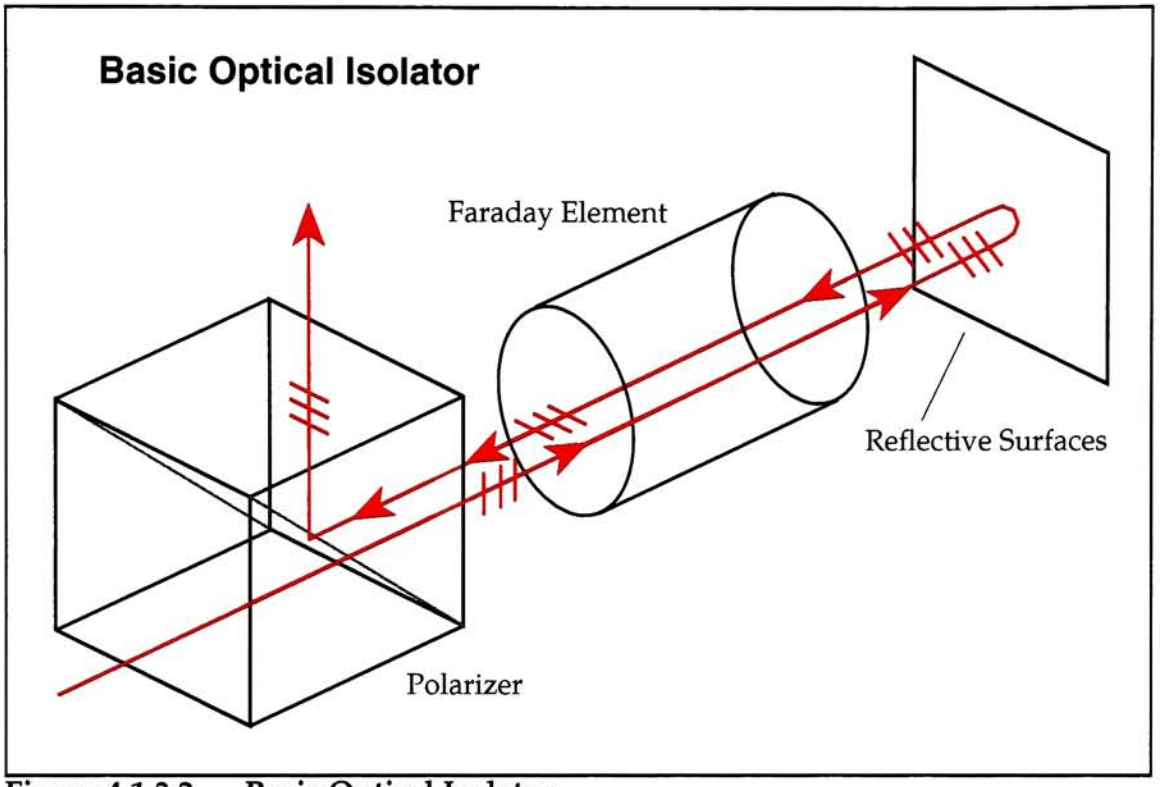

Figure 4.1.3.2 ~ Basic Optical Isolator.

The basic isolator fails if downstream components alter the 45° polarization, as any component of the backscattered light not orthogonal to the polarizer will be passed. This problem is easily solved with the addition of a second polarizer opposite the Faraday element from the first polarizer with its polarization axis aligned precisely with the 45° rotated light. Aside from losses caused by imperfection, this second polarizer has no effect on forward light but allows only light of matching polarization to pass back through only to be eliminated by the isolator. Chosen for their high extinction ratio (>50 dB), both polarizers employed were of Glan type. The unit was placed between the beam modulator and the focusing optics (refer to

Figure 3.1.1). Orienting it as such eliminated effects of all components save the modulator.

4.1.4 Positioning Subsystem

Receiver media and ribbon were mounted onto a motorized x-y vacuum chuck prior to exposure. Vacuum pressure was maintained at 7.2 psi (0.49 atm). Using this arrangement, the sample moved beneath the stationary laser beam. Encoder equipped lead-screw type stepper motors (American Precision Industries, Inc., Buffalo, NY) supplied by A•CAD•emic Solutions, Inc. were chosen carefully so that movement could be synchronized with the upper limit of the desired driving pulse frequencies. The stage motor controllers were driven through PC serial port connections.

While the precision of the x-y stage was more than adequate, the sample mounting procedure was found to be the weakest part of the imaging system. During system optimization, a good deal of time was spent working on ways to improve the ribbon/receiver contact area in the printing nip. Placing the imaging materials beneath a glass plate was ruled out due to objectionable amounts of reflection, absorption, and diffraction. Vacuum pressure was kept as high as possible; stubborn air bubbles were removed from the ribbon/receiver sandwich with a hard rubber pressure roller prior to imaging. In a commercial system, vacuum pressure would certainly not be used to locate the sample. Instead, a configuration similar to Figure 4.1.4.1 is envisioned. The ribbon and receiver would be held in place by 2 pressure

rollers and a platen drum. The laser beam would pass between the rollers to expose the ribbon. Another possible solution would be to employ a cylindrical glass roller through which the beam could pass. While the high nip pressures necessary for printing on rougher papers could be achieved in this way, reflection and absorption by dirty glass would probably limit performance.

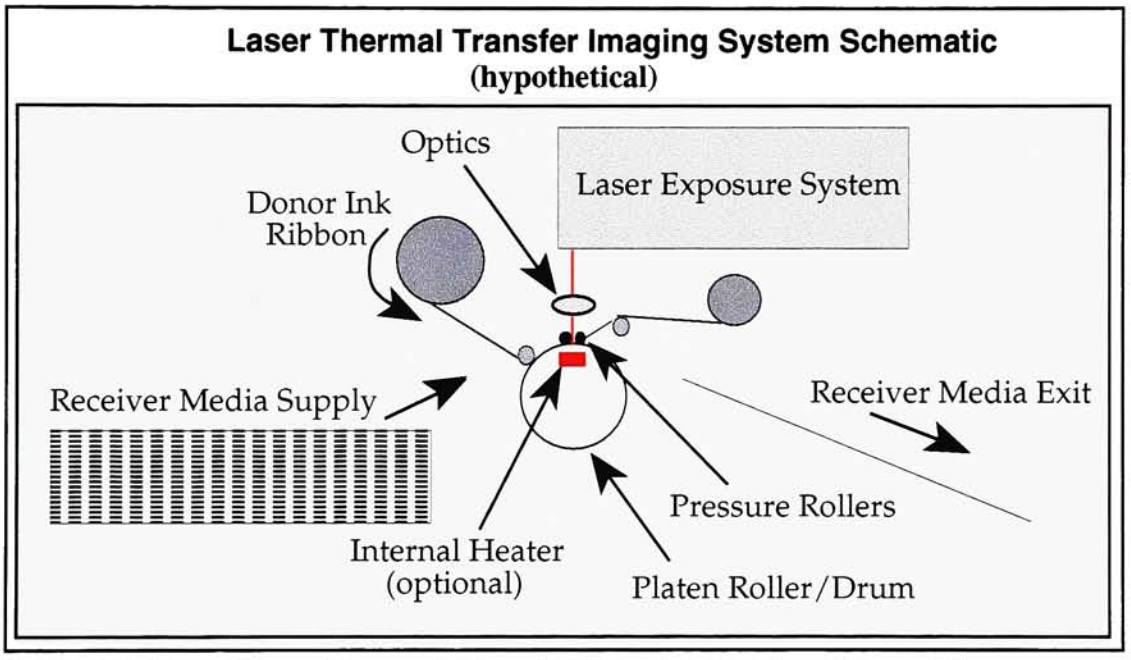

Figure 4.1.4.1 ~ Laser Thermal Transfer Imaging System Schematic.

4.1.5 Measurement Subsystem

Three independent detectors and an oscilloscope provided the means by which the laser exposure pulse envelope was quantified. A fast photodiode characterized the temporal shape of the pulse while the knife edge technique (Siegman, 1986) accurately captured the spatial pulse profile.

A conventional photodiode yielded the pulse amplitude. Much time and effort was put into these determinations, for without precise knowledge of the pulse, the mathematical model could not be verified nor could true beam fluence be reported.

Temporal pulse shape was determined with a Newport 875 Pin Detector fast photodiode. This particular unit was chosen on the basis of its sub-nanosecond rise time (t_r = 0.75 nsec). Figure 3.1.1 presents a schematic of the system. With the photodiode wired to a Tektronix 2440 Digital Oscilloscope and placed between the focusing optics and exposure plane, pulse shape could readily be resolved. Due to the high near-IR sensitivity of the device, only the characteristic shape of the pulse (and not its height) could be determined in this manner. By connecting the second input of the oscilloscope to the pulse generator controlling the electro-optic modulator, a Stanford Research Systems, Inc. Model DG535 Digital Delay/Pulse Generator, timing pulses could be monitored in line with the laser intensity pulse. Figure 4.1.5.1 shows the observed pulse shapes.

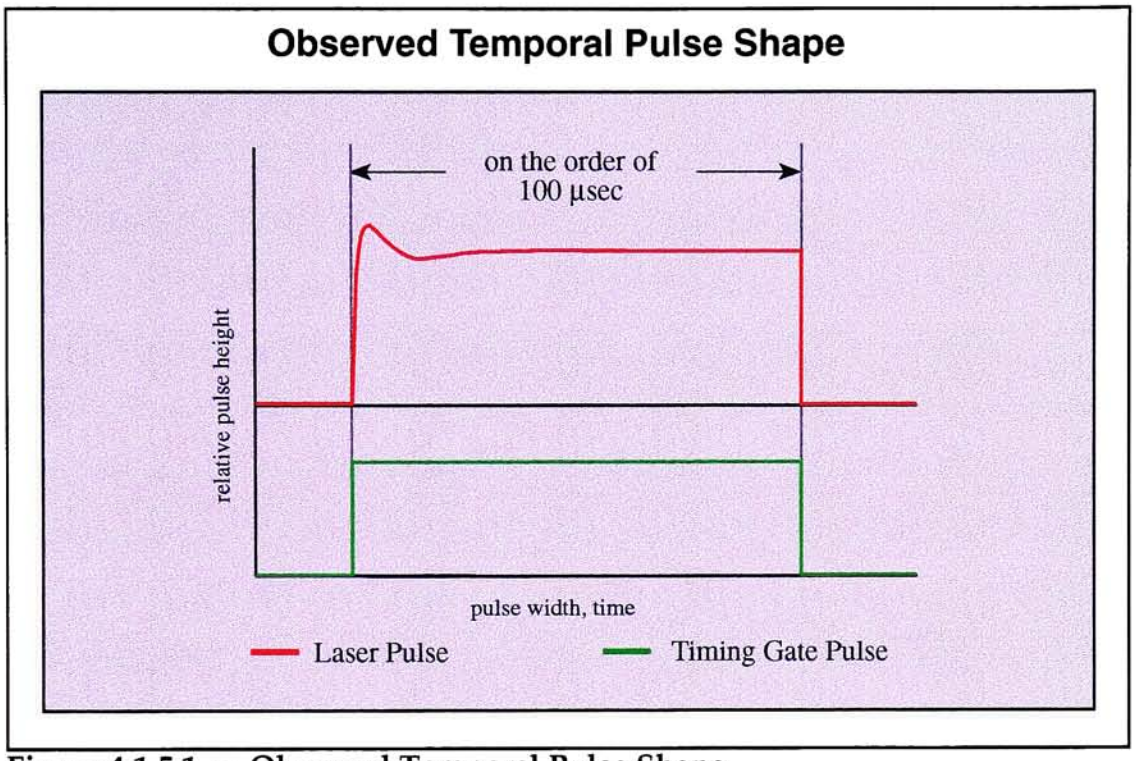

Figure 4.1.5.1 ~ Observed Temporal Pulse Shape.

The majority of the irregularity at the pulse onset was determined to be attributable to the response of the detector. If one were to deconvolve the detector response from the waveform, the shape would be nearly perfectly rectangular. Even so, given the aspect ratio of the empirically timed pulse, it was definitely not a stretch to consider the pulse square. Of course, it was not by luck that a rectangular timing pulse translated to a rectangular energy pulse. The carefully chosen electro-optic modulator assured that this would be the case. This determination was important chiefly to the mathematical model. Were the pulse not rectangular, computations would have become significantly more cumbersome.

Pulse height measurements were determined with a Scientech Photodiode and an Astral AD30 Power Meter. Figure 3.1.1 shows the power metering configuration. By holding the pulse generator's timing gate open with the amplitude set to the level used for exposure, a continuous pulse of the desired amplitude could easily be measured. Each time the gate amplitude was changed, pulse amplitude was remeasured in this manner. In one case, exposure optimization led to 19.6 mWatts, obtained with a 0.31 V gate amplitude. Closing the gate yielded the amount of power bled through the electro-optic modulator between pulses. This value, recorded 30 times over the life of the experiment was found to be 6.28 mWatts, with a variance of 0.0006. Dividing these two numbers yielded the Extinction Ratio ρ_{ext}:

$$\rho_{ext} = \frac{P_{\max.out}}{P_{\min.out}}, P_{\min.out} > 0 \qquad (1)$$

This ratio is similar to one proposed by Conoptics, Inc. The criteria has been placed on P_{min} so that the formula does not fail for the ideal system. Maximization of this ratio was very important to image quality. As the ratio decreases, dot blur increases. Figure 4.1.5.2 illustrates dot blur caused by a low extinction ratio.

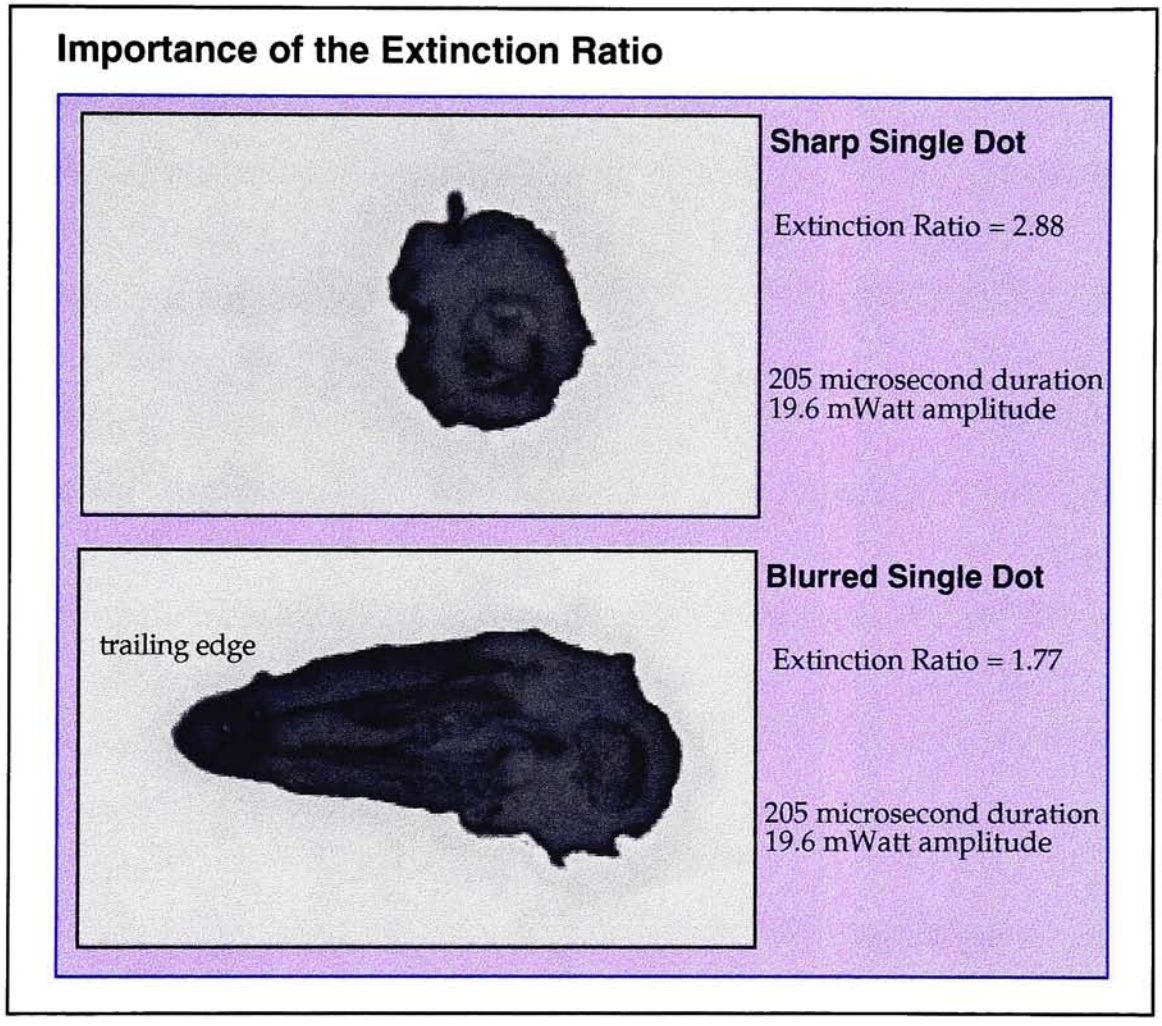

Figure 4.1.5.2 ~ Importance of the Extinction Ratio.

The faster the writing system, the more important a high ρ_{ext} becomes. The result is similar to the printhead residual heat effects common to conventional thermal transfer systems. While even a large amount of leakage does not provide enough energy to transfer solid wax ink, it may carry enough to push ink in the rubbery state (just above the polymer's Tg) to a

state of viscous flow that may result in transfer. Note in Figure 4.1.5.2 the texture of the tail of the blurred dot. There are lines demonstrative of flow as the dot trails off. The laser beam traces across the ribbon either bleeding power or pulsing. Just after a pulse, the laser traces over the adjacent area at bleed output level. If this bleed energy is great enough to push the ink adjacent to the molten dot to a state of viscous flow, transfer may extend past the dot. As the distance from the dot and the time since pulsation increase, the influence of the "hot spot" decreases and the bleed power is no longer sufficient to produce transfer. In this case, the printed dot acts as a catalyst for further transfer. Just as in conventional thermal transfer, this effect may be modeled and compensation may be built into dithering algorithms. The effect is dependent not only on the laser but also on the ink's thermal and melt-rheological properties. Modifying the ink's melt rheology does have an effect on this phenomenon.

The final piece of the laser exposure system requiring intimate understanding was the spatial intensity profile of the beam. In terms of building a model of the imaging system, as the ideal temporal profile would be rectangular, the perfect spatial intensity function would be cylindrical. Whereas the temporal profile was measured and determined to be effectively rectangular at the pulse widths being used, determination of the spot function yielded a result not so simple. Beyond the exit pupil of the laser cavity were several other optical components. All real optical components degrade signals passed through them more or less, commonly blurring a point source

by widening the intensity distribution about the intensity axis. The manufacturer claimed the beam profile produced by the laser to have a nearly symmetrical Gaussian radial shape. The best optical systems are tunable to some degree in three orthogonal dimensions (Siegman, 1986). Through careful alignment of the optical components, it was possible to obtain a nearly circular Gaussian intensity profile.

For purposes of both modeling and interpreting the empirical results, it was important to quantitatively determine such characteristics as the pulse intensity profile. A BeamScope Optical Profiler (Dataray, Inc.) provided the means. Figure 3.1.1 shows the system configuration. The device used consists of two orthogonal scanning linear CCD arrays which employ the knife edge technique (Siegman, 1986) to accurately capture the spatial pulse profile. It was positioned so that its small motor drove the two slits back and forth in the beam path at the film plane. Signals interpreted by the BeamScope's CPU were analyzed with the resident software, Microsoft Excel, Wolfram Research Mathematica, and Computer Associates Cricket Graph III. Figures 4.1.5.3 and 4.1.5.4 graphically display the results. Note the high degree of fit to the Gaussian curve in both of the simultaneously measured dimensions. By adjusting the orientation of the slits, it was possible to confirm a radial profile. Once the optical system was optimized, Gaussian fit to measurements made at any orientation never fell below 98%. This data proved that the pulse was not significantly asymmetric. While not the *ideal* cylindrical pulse, this result was indeed welcome, as the shape was well

defined, could be employed accurately in the model, and was convenient to visualize.

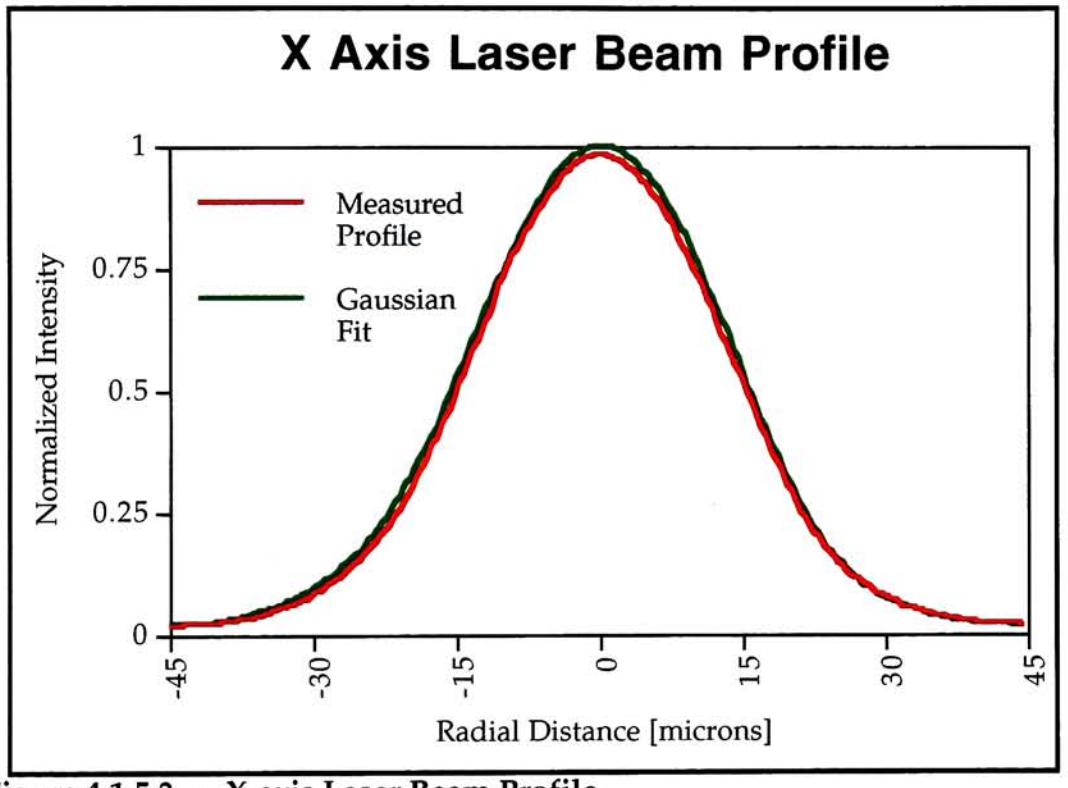

Figure 4.1.5.3 ~ X-axis Laser Beam Profile.

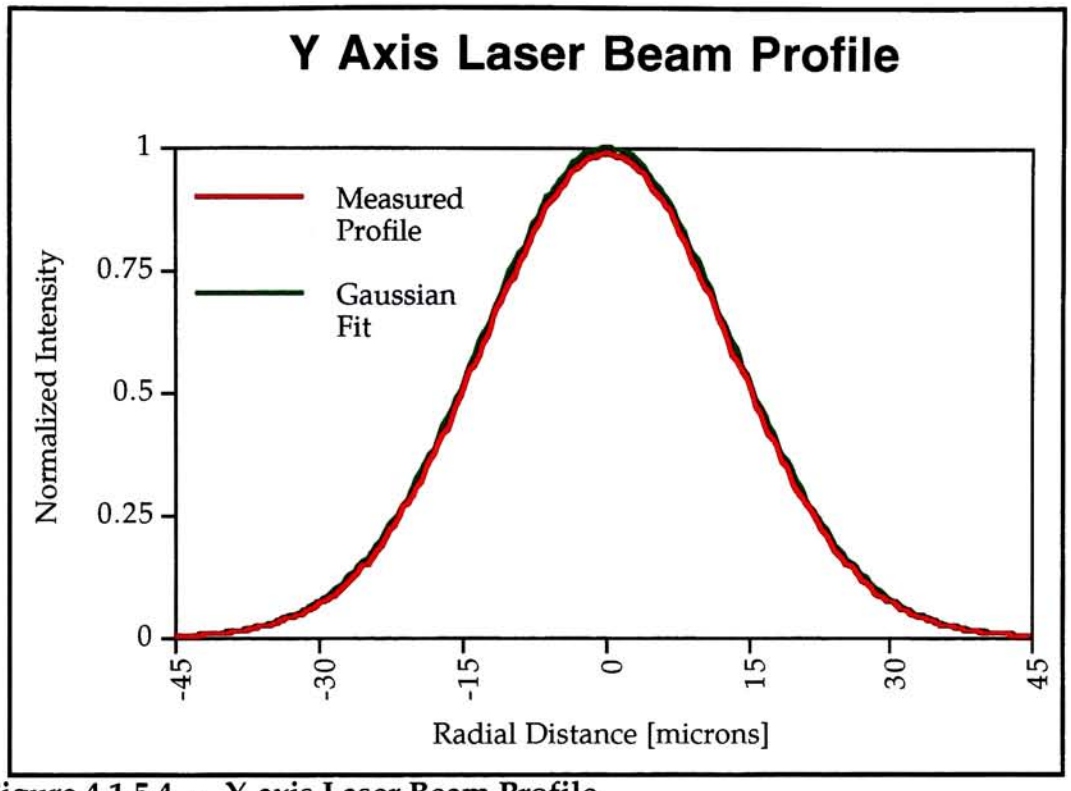

Figure 4.1.5.4 ~ Y-axis Laser Beam Profile.

4.1.6 Gaussian Profile for Variable Dot Size Printing

Although model calculations would have been slightly less cumbersome had the pulse been spatially cylindrical, printing variable dot sizes would have been much more difficult. The Gaussian shape yielded a relatively gradually sloping, continuous intensity distribution from zero some distance away from the pulse's z-axis to maximum intensity on the z-axis (radial distance = 0). A cylindrical intensity distribution would have been bimodal, with a discontinuous jump from zero intensity to maximum intensity at the beam radius.

In contrast to dye sublimation printing, the thermal wax transfer printing process is bimodal, that is, the entire thickness of wax irradiated by the energy source will either transfer to the receiver sheet or remain adhered to the ribbon substrate. In this case, there is a threshold temperature, above which thermal and rheological conditions permit the transfer of molten ink to the receiver. There is no case, regarding the type of thermal transfer ribbons researched, where an intermediate thickness of wax is transferred. Therefore, in order to build a grayscale thermal transfer device without conventional dithering, it is necessary to vary the size of the dot printed. Such dot size variation can be accomplished by varying the size of the isotherm that describes the transfer threshold temperature condition. With a Gaussian beam distribution, altering the intensity alters the location of this isotherm. Figure 4.1.5.5 shows, for the ideal Gaussian heated DT2 printing process, a few of the dot sizes achievable by varying intensity. In an actual system, the number of different dot sizes achievable (or, the grayscale capability) is a direct function of the signal-to-noise ratio of the printing system.

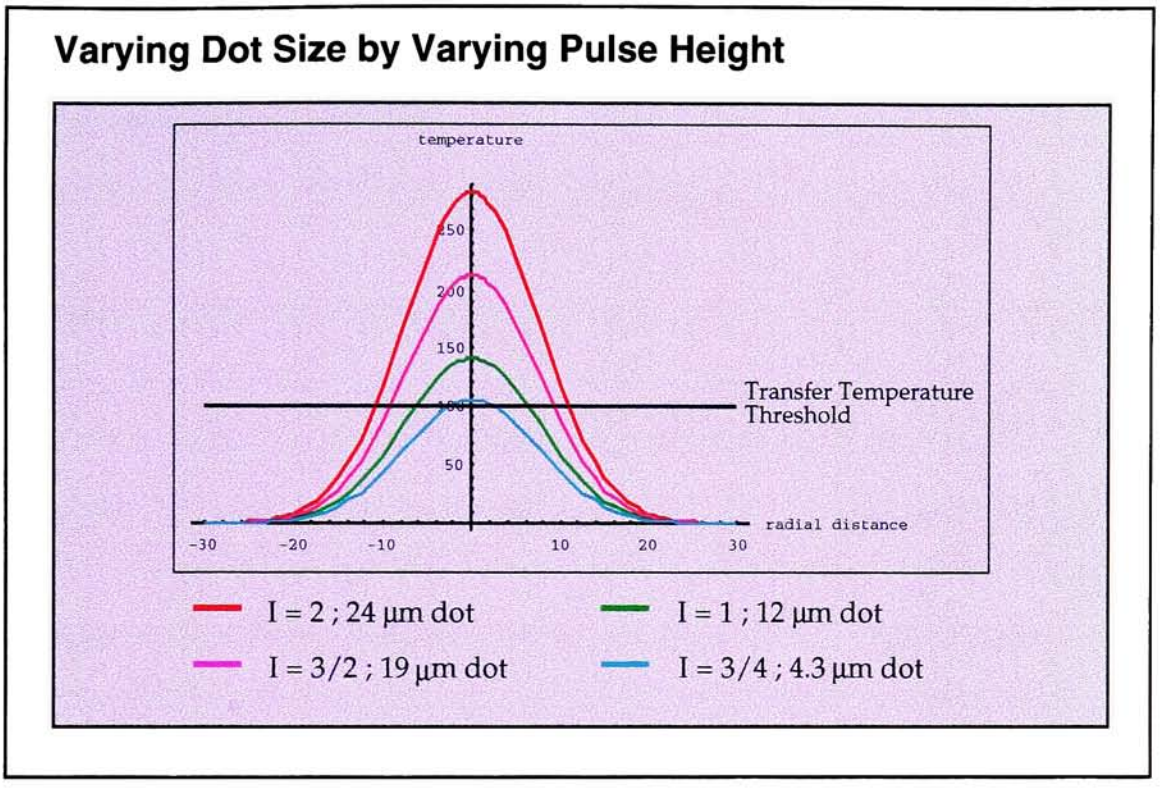

Figure 4.1.5.5 ~ Varying Dot Size by Varying Pulse Height.

4.2 The Ink Ribbon

A great deal of research focused on the design of the ribbon. Both solvent and water based systems were investigated before a dispersion method was chosen. Much effort focused on the process of producing ink mixes, beyond formulation. In a system such as this, where the nip is only under low vacuum pressure and the desired resolution is so high, coating uniformity is of tremendous importance. Ink ingredient order of addition was investigated as was mixing vessel, impeller structure and speed, draw-down coating technique, centrifuge post-processing of the ink, and drying of

the coated substrate. Each of these areas played an important role in the production of ribbons for LT2. Once a dispersion type, base formulation, and mixing procedure were decided upon, the formulation was optimized for high transfer efficiency, that is, image-wise transfer at low energy density.

4.2.1 Initial Wax Ink Formulations

The first inks made were of single-layer solvent dispersed wax type. Wax and carbon black pigment was dispersed in a mixture of toluene and IPA. Small amounts of a resin were used in some cases to modify rheological properties. As an aside, it is important to note that while up to 10% of the ink was comprised of a resin, the ribbons were still referred to as the wax type. This is the case in industry, where almost all wax type ribbons contain some small amount of resin. It has been suggested (Lacy, 1995) that the line between wax and wax/resin blend ribbons be drawn on the basis of price, rather than on formulation (a small amount of resin, from a few to 10%, in most cases does not significantly raise the price of the ribbon). This first group of experiments provided a fundamental understanding of the parameters governing the solvent mix making process. Percent solids of the mix was found to be of great importance. Additionally, the difficulties of handling finely divided pigment particles led to investigations of the various dispersion methods.

Waxes first had to be dissolved in order to disperse in IPA. Toluene provided a means to dissolve the waxes which were not highly soluble in

IPA. The mix making process, therefore, was to combine the waxes (paraffin and carnauba) and resin (ethylene vinyl acetate) over a hot plate, mixing the molten composite by stirring. Toluene was added to the mixture at 80 °C, dissolving the waxes and resin. Wax, resin, toluene and IPA constituted a continuous liquid phase. Pigment was folded into a steel beaker and the contents transferred to a quantity of IPA at 20 °C. At this stage, the ink was comprised of about 20% solids, 30% toluene, and 50% IPA. Once transferred to IPA, pigment was dispersed with an impeller type lab mixer (Bamix ESGE Laboratory Mixer), yielding a second solid phase, totally encapsulated by the liquid. The liquid was inherently of low enough γ to wet the pigment particles, so no surface chemistry altering additives were necessary in these formulations. It was soon found to be impossible, however, to produce sufficient sheer energy to consistently break up pigment aggregates solely with the lab mixer. Reason for the ineffectiveness of the impeller method was largely due to the rheological properties of the aromatic hydrocarbon toluene. Its ultra low viscosity and zero *tack* (Cabot Corporation, 1989) prevented any of the sheering action necessary to break up pigment aggregates.

Indeed, in the mass production of thermal transfer ink ribbons, preliminary mixing techniques are always supplemented with an additional dispersing step using equipment such as ball mills or attritors. To mimic the action of an attritor in the lab, a quantity of glass beads (4 mm diameter) was added to the mix, the vessel was sealed, and placed in a conventional paint shaker for 30 minutes. Viewing ink films with a microscope and transmitted

illumination revealed resulting dispersion quality comparable to that of production based inks.

In order to produce ribbons of adequate coating quality, ink film thickness and uniformity had to be optimized. For these solvent dispersed inks, percent solids and Meyer rod gauge were found to govern coating quality. Coating uniformity was based on the second-order statistics (variance) of a 3 inch transmission micro-intensity trace of the ribbon. On first glance it was thought that a factorial experiment would be necessary in order to determine the optimum combination; however, upon producing the first few ribbon trials, it was observed that uniformity was quite independent of Meyer rod gauge at both low (7% and below) and high (12% and above) solid percentages. When the ink/solvent combination was either too thick or too thin, it simply would not spread evenly with *any* Meyer rod at 20 °C. Results of a factorial experiment surely would have echoed this fact. Therefore, solid percent was optimized first and the result then applied to the optimization of Meyer rod gauge.

Figure 4.2.1.1 graphically shows the results of these experiments. Intensity vs. linear pixel position illustrates the difference in variance for three ribbons coated at varying solid percentage and may be correlated to the supplemental images of Figure 4.2.1.5. For ease of graphical interpretation, the curves have been smoothed with a five point running average; calculations were based on unsmoothed data, however. Note the decrease in standard

deviation with the decrease in solid percentage, exemplifying the ink's ability to flow evenly. Figure 4.2.1.2 gives the results of all of the solid percent variations. The lowest standard deviation, and hence the most uniform coating, corresponds to a concentration between 9 and 10% solids.

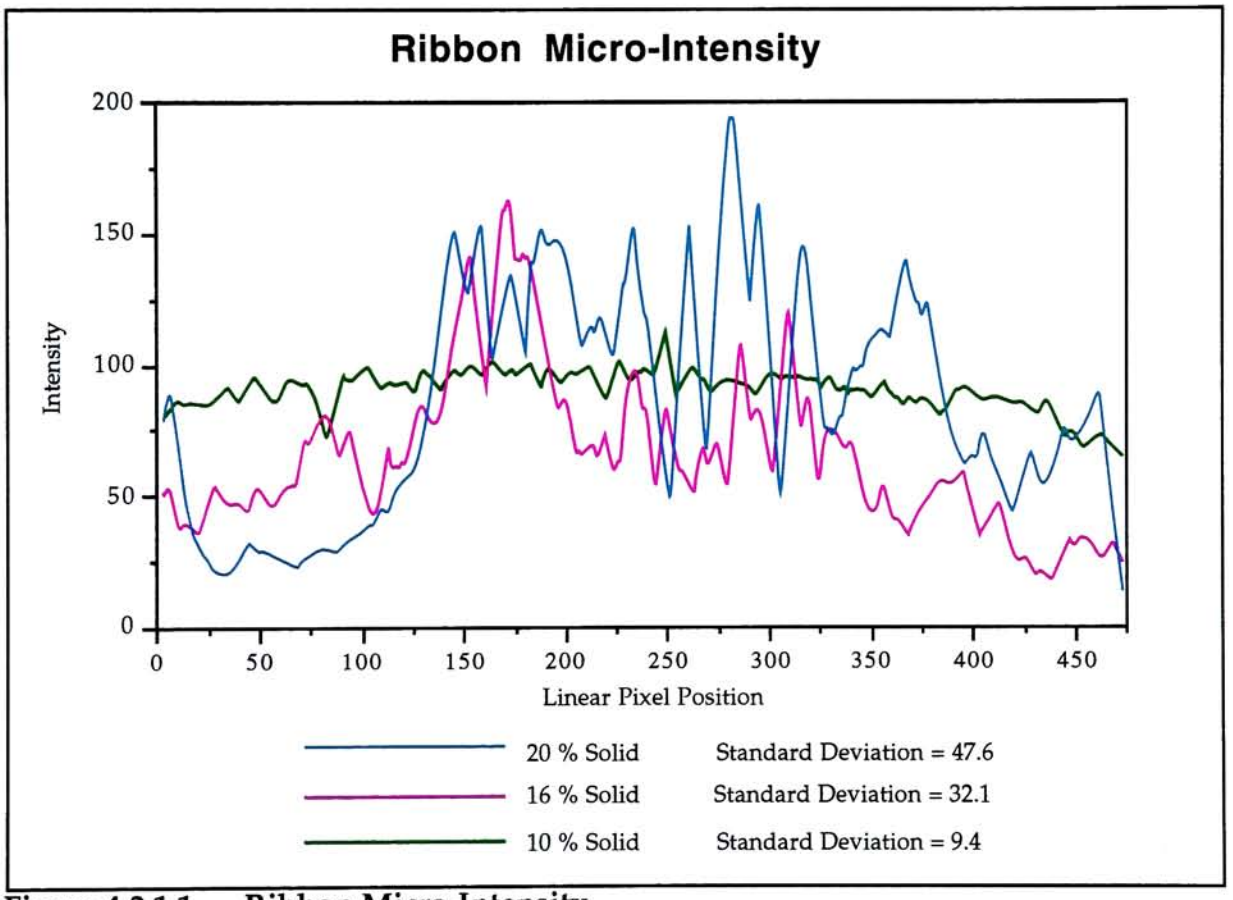

Figure 4.2.1.1 ~ Ribbon Micro-Intensity.

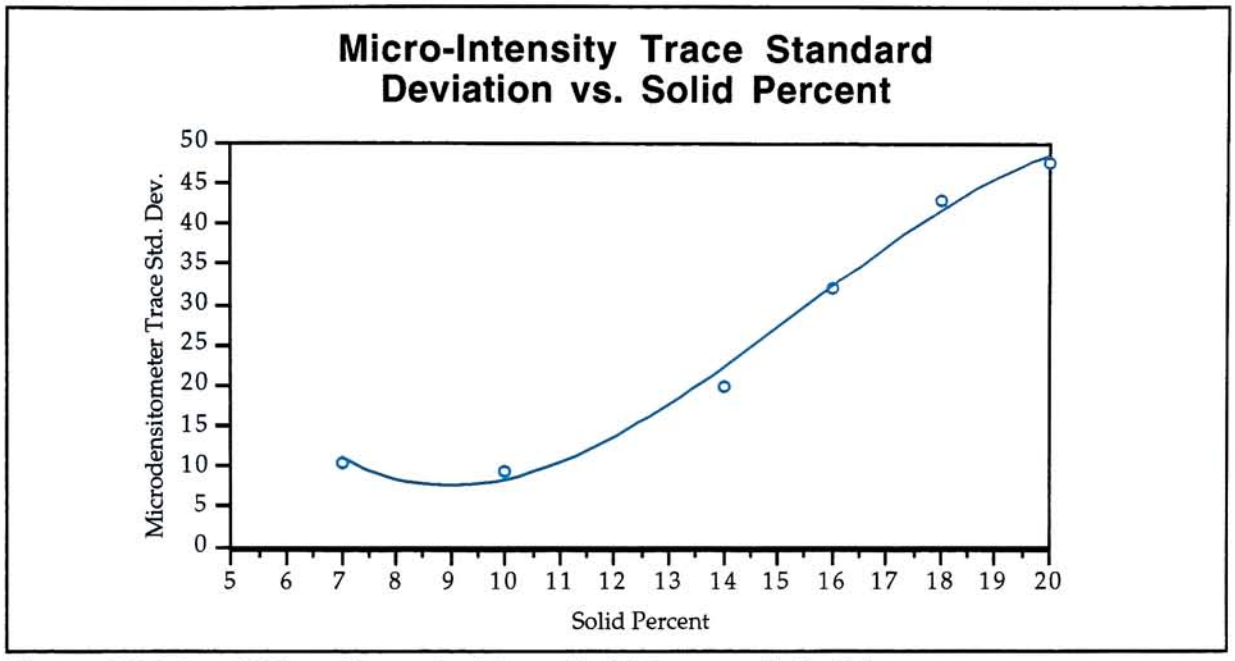

Figure 4.2.1.2 ~ Micro-Intensity Trace Std. Dev. vs. % Solids.

A concentration of 10% solids was then used to generate Meyer rod gauge test data (using Meyer rods from R.D.S. of Webster, NY). As would be expected, coating uniformity increased with coating thickness before beginning to decrease due to sinusoidal variation in coating thickness caused by the lower frequency winding of the wider wire Meyer rod (see Figures 4.2.1.3 and 4.2.1.4). The decrease in uniformity is slight from a #19 rod to a #26 -- note the y-axis scale of Figure 4.2.1.3. A Meyer rod gauge of 24 was used in the production of the first ribbon to be print tested. A series of prints were made using a conventional 300 dpi print engine. This first printing revealed that a coating thickness of 3.0 μm was not sufficient to minimize voids due to receiver (paper) irregularities, so a second ribbon was produced at 4.6 μm (#30 Meyer rod). Results from this test were satisfactory, demonstrating that noise

introduced by paper surface irregularities masks slight coating weight irregularities.

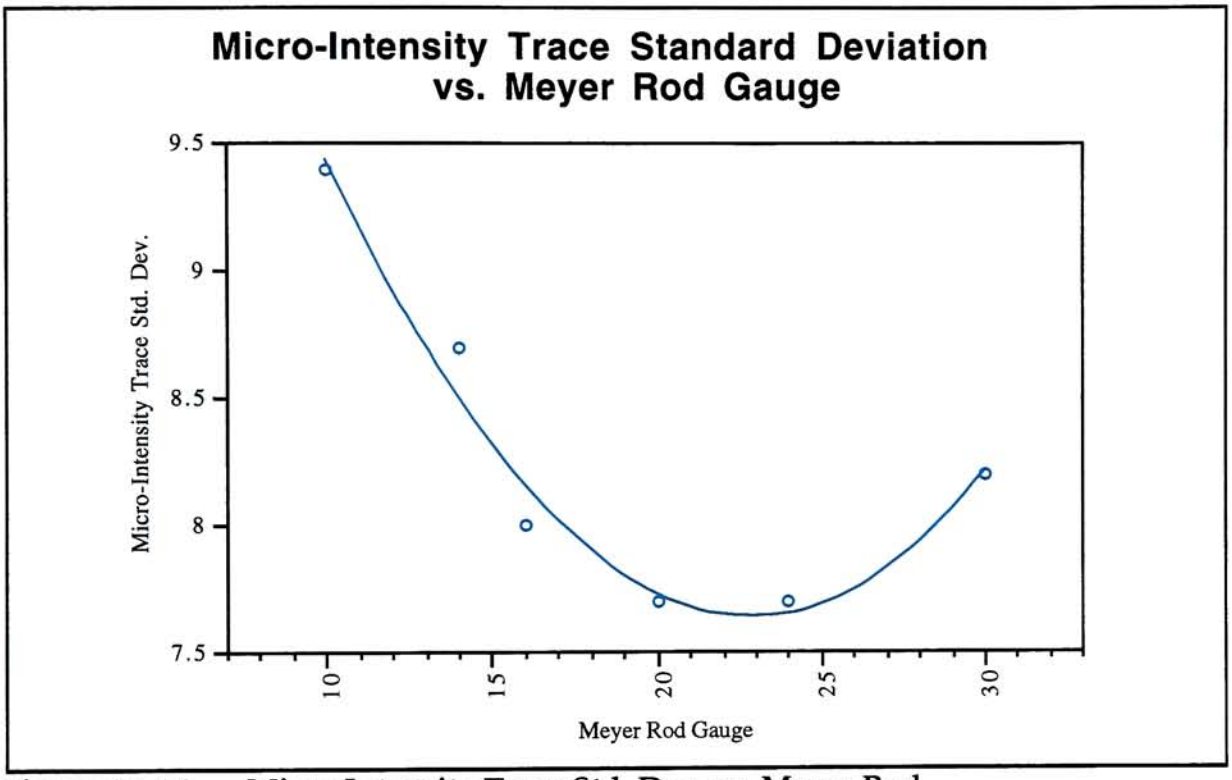

Figure 4.2.1.3 ~ Micro-Intensity Trace Std. Dev. vs. Meyer Rod.

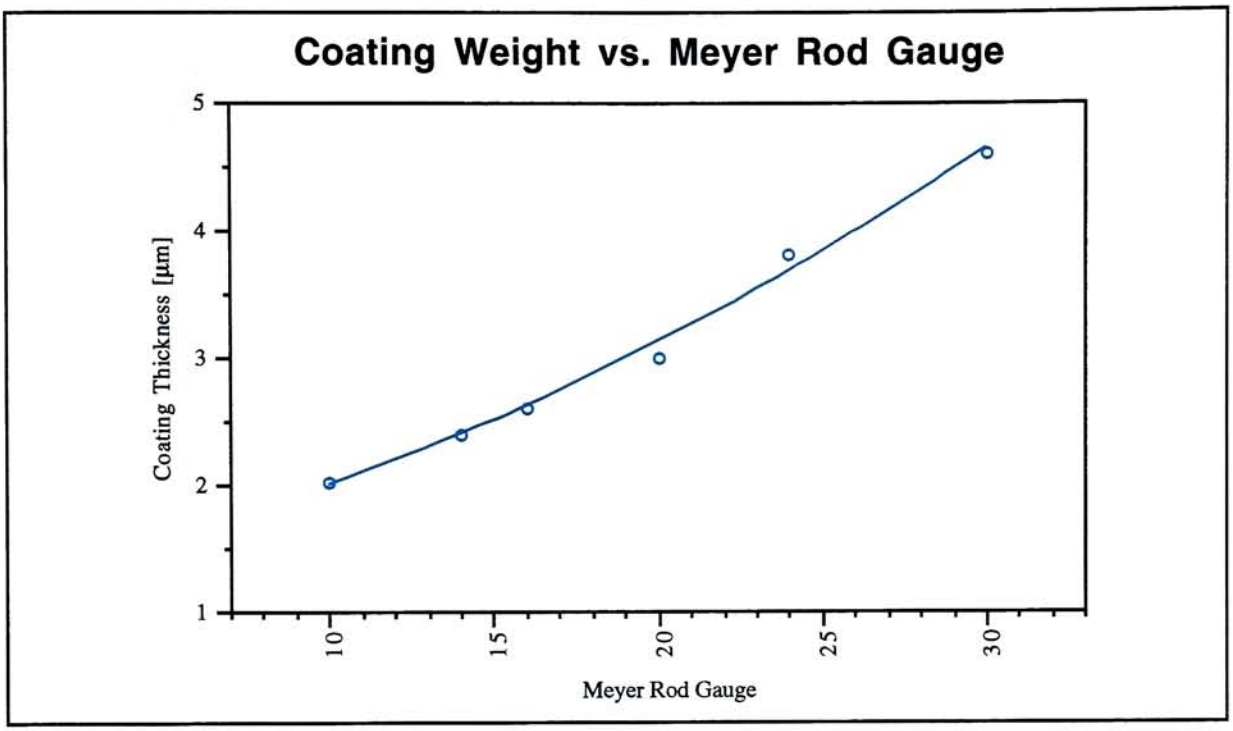

Figure 4.2.1.4 ~ Coating Weight vs. Meyer Rod Gauge.

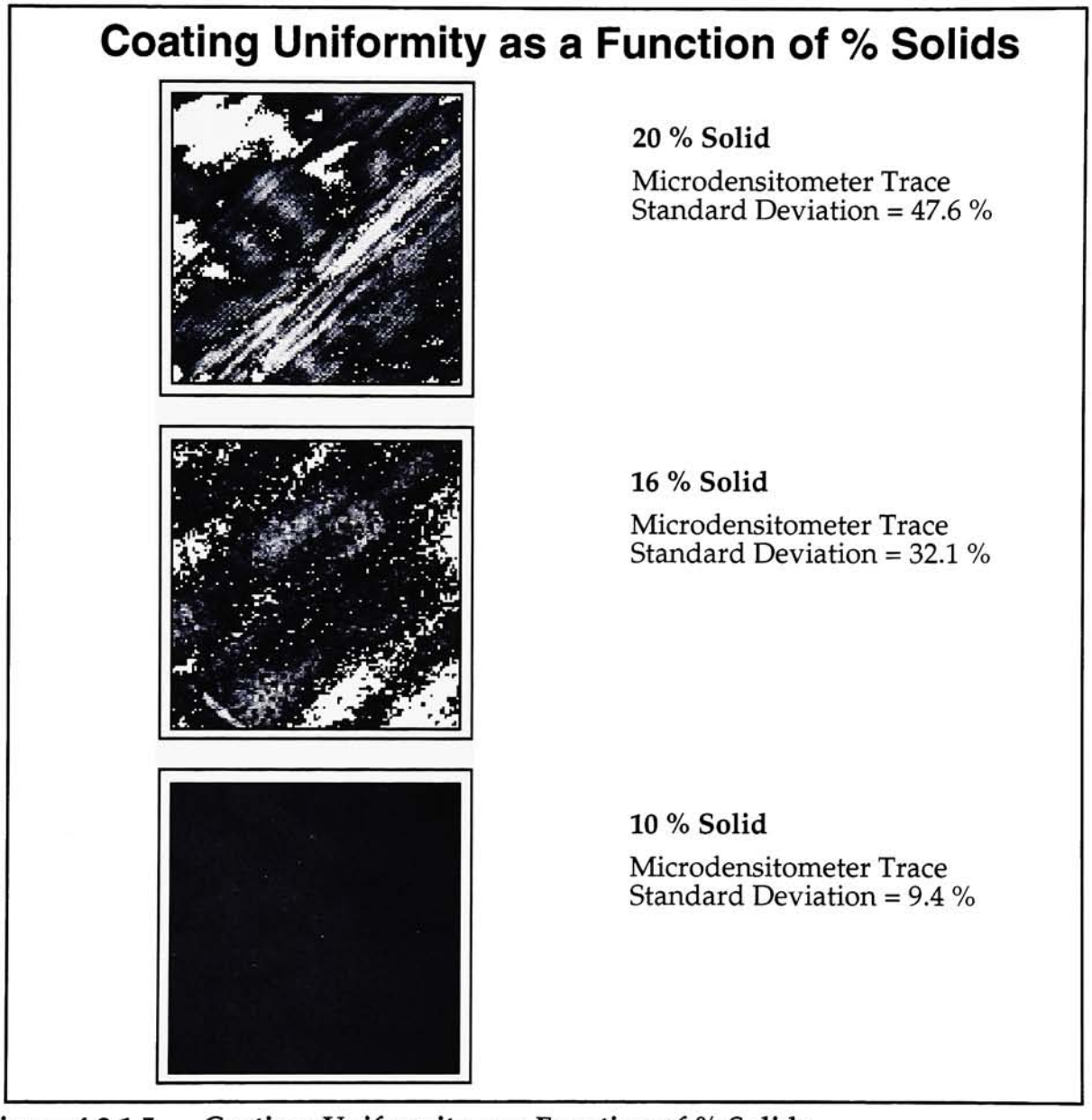

Figure 4.2.1.5 ~ Coating Uniformity as a Function of % Solids.

While the experimenter encountered no major difficulties in producing solvent dispersed inks, disposing of waste materials and

incinerating the solvent during the drying process was a real concern. As mentioned in section 3.2, environmental issues and state and federal regulations on v.o.c. emissions are ever increasing, forcing any concerned coating chemist to formulate environmentally friendly coatings whenever possible. For this reason, formulations were redesigned to allow water based coating. Fortunately, the fundamentals of pigment dispersion and draw-down coating techniques could be applied to the more difficult chemistry work which ensued.

4.2.2 Water Based Wax/Resin Ink Formulations

Building on the experience gained from previous solvent dispersed ink work, aqueous dispersion ink formulating began by first finding waxes and resins that could readily be adapted to this approach. Producing stable aqueous solutions of most waxes and resins in water is not a trivial task. Fortunately, several commercially available wax and resin latexes and emulsions exist, permitting the ink chemist to concentrate on formulating unique inks and coatings. Needless to say, the experimenter took full advantage of these products in formulating the wax/resin photothermal conversion layer (PCL) as well as the release layer (RL). As mentioned in the Approach, the first several ribbons of this type were of single layer design. It was not until system optimization was begun in earnest that a multi-layer ribbon was designed. Designing and optimizing the RL was trivial once the daunting task of formulating pigmented ink layers had been mastered.

Compared to the solvent dispersions, water/alcohol dispersions were found to be much more difficult to produce, for a number of reasons. Principally, waxes and resins are generally much less soluble in dilute water/alcohol mixtures than they are in aromatic hydrocarbon solvents such as toluene (also known as methylbenzene). Additionally, the comparatively low γ of high v.o.c. solvent mixtures greatly aided the wetting of the pigments used, making the use of additional surfactant additives unnecessary. For water/alcohol mixtures, however, even when using predispersed binder ingredients, great care had to be taken in order to assure compatibility between ingredients. The pH of the various ingredients had to be monitored closely, as it was experimentally found that any deviation to the opposite side of neutrality from the bulk of the mixture by an additive would shock the system and result in clumping and/or precipitation of one or more binder ingredients. Trace amounts of ammonium hydroxide were added as necessary to maintain pH between 7.5 and 9. In order to permit wetting of the pigment, a surfactant had to be employed.

DuPont, Inc. Zonyl FSJ, an anionic fluorosurfactant, was employed to capitalize on the slightly basic formulation yielding ultra-high effectiveness at very low concentration (0.1%). Zonyl FSJ has the following formula:

$(F(CF_2CF_2)_{3\text{-}8}CH_2CH_2O)_{1,2}P(O)\ (ONH_4)_{2,1}$ + Non-fluorinated surfactant.

The fluorocarbon chain, $F(CF_2CF_2)_{3-8}$, in the fluorosurfactant molecule affords this surfactant its high effectivity for the designed water based system by giving the surfactant an extreme tendency to orient at interfaces. "This tendency results from the small affinity of fluorocarbon molecules for water and the low interaction between fluorocarbon chains. Consequently, fluorosurfactants depend upon the powerful wetting action which usually corresponds to such low surface tensions" (EI DuPont, Inc., 1993). Once this surfactant was selected, a series of single variable experiments served to determine the minimum quantity necessary for complete pigment wetting. Evaluation of dispersion quality was completed as above, where inks were draw-down coated and analyzed with a micro-image analysis system.

A large number of screening experiments were conducted in order to obtain a base formulation for the PCL. At the design stage, necessary ingredients were defined. These ingredients included:

- wax base with a T_m in the neighborhood of 60 °C
- plasticizer resin with a T_g below room temperature
- resin with strong adhesive affinity to the chosen receiver
- viscosity modifying resin
- pigment.

Conventional wax/resin inks generally contain significant amounts of paraffin and carnauba waxes. Johnwax 120 (S.C. Johnson Wax, Racine, WI), a commercially available paraffin/polyethylene wax blend, offered similar solids properties in an aqueous pre-emulsified product. With respect to the

second, third, and fourth ingredients listed above, aqueous polymer latexes and emulsions having glass transition temperatures below 20 °C abound, as do emulsifiable viscosity modifiers. Indeed, due to the wide variety of readily available chemicals suiting these loose requirements, items two through four of the above list required the greatest screening effort. Possible candidates eventually screened out for various incompatibilities included ethylene vinyl acetates (EVAs), styrene maleic anhydrides, polyacrylic acids (PAAs), and certain other styrenated acrylics. The second, third, and fourth requirements listed above were eventually met with two styrenated acrylic polymers, Joncryl 624 and 2560 (S.C. Johnson Wax, Racine, WI), and PVP, PVP K-90 (ISP Technologies, Inc., Wayne, NJ). Screening experiments included, in the following order, (1) test tube compatibility tests, (2) draw-down coatings to check film forming abilities, and (3) complete wax ink production, draw-down ribbon coating, and print testing.

Two general types of pigments were investigated, both of which strongly absorbed 1.064 μm radiation, one of which was opaque over the visual wavelengths, the other of which, when properly formulated, was largely transparent to the human eye. By far, the greatest amount of effort was spent on formulations containing carbon black pigment. Of seven carbon black grades sampled from the Cabot Corporation (Billerica, MA) including both fluffy and pelletized powders, two were selected as finalists based on dispersibility (Cabot Black Pearls L and Cabot Vulcan XC72R), and one of those was chosen over all others based on its superior dispersibility and anti-static

properties (Cabot Vulcan XC72R). This carbon black offered 30 nm mean primary particle size with high structure (254 m^2/gm surface area) and provided the highest conductivity of any of Cabot's blacks. The high conductivity was viewed as a strong plus due to the ability of a ribbon formulated with this pigment to dissipate static charge during winding and unwinding.

The high aggregate structure, caused by large primary aggregate size, equated to relatively large amounts of occluded air which consequently produced some wetting difficulties. However, the high structure also kept the aggregates from packing too tightly, keeping inter-aggregate distances smaller and van der Waals attractive forces lower. Of course, the goal of the pigment dispersion effort was to produce a condition in which all agglomerates were broken down into primary aggregates, each primary aggregate separated from every other aggregate, and the surface of each aggregate completely covered by vehicle or resin (Cabot Corporation, 1989). To this end, once the fluffy XC72R pigment was wetted by adequate adsorption of the binder solution, much less effort had to be placed on de-agglomeration than with other pelletized grades.

Table 4.2.2.1 presents an example wax/resin ink formulation mix outline. Note the order of addition, which was carefully chosen based on test tube compatibility experiments. The S.C. Johnson ingredients were added together first, followed by water (to decrease mix viscosity and solvent contribution) and ethylene glycol (to aid pigment wetting). Ethylene glycol

was chosen only after several other alchohols were tested, including isopropanol, Dowanol PM (Dow Chemical, Inc.), N-butanol, and 1-octanol, all of which failed due to clumping produced with their addition. It is theorized that the additional [OH^-] of ethylene glycol coupled with its short carbon backbone permitted compatibility in the system designed. Following alcohol, PVP was added (largely to modify viscosity) before the Zonyl FSJ surfactant. With each addition of an ingredient, the mixture was stirred with a glass rod for several minutes. Finally, pigment was carefully folded into the mix in preparation for final dispersion.

Table 4.2.2.2 lists the ingredients for the final multi-layer ribbon design. Each component served a specific task, listed in the table under **Function.** The low melting points of the RL ingredients indicate low tensile strength at imaging temperatures, which was indeed found to be the case. The sole function of this layer was to allow extremely uniform, efficient release from PET. The PCL could then be formulated specifically for photothermal conversion and adhesion to the receiver sheet. Note the range of melting points and glass transition temperatures of the PCL ingredients. The low T_g thermoplastics assured the ink would not flake off of the substrate during handling and plasticized the ink during printing, modifying the low tensile strength molten state rheology of the wax employed.

Multi-Layer Wax/Resin Ribbon Ink Mix Content
Mix No.: DE 109

Photothermal Conversion Layer:

Manfr.	Order of addition	Product	pH	%Solids	solution amount	grams to add	solvent content
Cabot	8	Vulcan CK	•	100%	4.9%	2.71 g	0.00
GAF	6	Luviskol (PVP)	7.0	10%	27.2%	15.00 g	13.50
Johnson	3	Joncryl 624	8.1	48%	5.5%	3.05 g	1.59
Johnson	2	SCX 2560	8.4	55%	6.2%	3.43 g	1.55
Johnson	1	Jonwax 120	9.0	34%	56.2%	31.00 g	20.46
						55.19 g	37.10
	5	ethylene glycol				22.26 g	
	4	water				16.69 g	
	7	Zonyl FSJ (40%)				0.33 g	
				Totals :	Pigment :	2.71 g	
					Binder :	15.38 g	
					Solids :	18.10 g	
					Total Mix :	94.48 g	
					% Solids :	19.16%	
					P:B :	0.18	

Release Layer:

Manfr.	Order of addition	Product	pH	% Solids	solution amount	grams to add
Koster Keunen	2	Bee's Milk	5.1	24%	30.0 %	7.50 g
Johnson	1	Jonwax 120	9.0	34%	70.0 %	17.50 g
	•	water				0.00 g
					Total Mix :	25.00 g

Table 4.2.2.1 ~ Example LT2 Ink Formulation.

The wax/resin ink mixture was dispersed through use of a lab mixer for one hour with an impeller speed of 800 rpm. Mix batch size was matched with vessel dimensions and impeller geometry so that the vortex formed was of the shape pictured in Figure 4.2.2.1. The impeller was centered on the axis of the vessel; the blade was approximately 0.25" above the bottom. The particular impeller design, shown in Figure 4.2.2.1, was chosen over other

multi-blade and slotted types of various sizes through a series of single-variable experiments. The metric for these experiments was dispersion quality, measured as above, using micro-image analysis.

Release Layer

Component	Manufacturer	Description	Function	Tm/Tg
Beesmilk	Koster Keunen	Beeswax dispersion	Thermoplastic Wax Release	Tm 63 °C
Jonwax 120	Johnson	Polyethylene/paraffin wax emulsion	Thermoplastic Wax Binder	Tm 61 °C
ZONYL FSJ	Du Pont	anionic fluorosurfactant dispersion	Surfactant	•

Adhesive Photothermal Conversion Layer

Component	Manufacturer	Description	Function	
Vulcan XC72R	Cabot	Conductive carbon black	Pigment	•
Jonwax 120	Johnson	Polyethylene/paraffin wax emulsion	Thermoplastic Wax Binder	Tm 61 °C
Luviscol K-90	ISP Technologies	PVP dispersion	Thermosetting Resinous Binder	Tg 184 °C
SCX 2560	Johnson	Styrene acrylic polymer latex	Thermoplastic Resinous Binder	Tg -11 °C
Joncryl 624	Johnson	Styrene acrylic polymer latex	Thermoplastic Resinous Binder	Tg -30 °C
ZONYL FSJ	Du Pont	anionic fluorosurfactant dispersion	Surfactant	•

Table 4.2.2.2 ~ Ribbon Coating Constituent Descriptions.

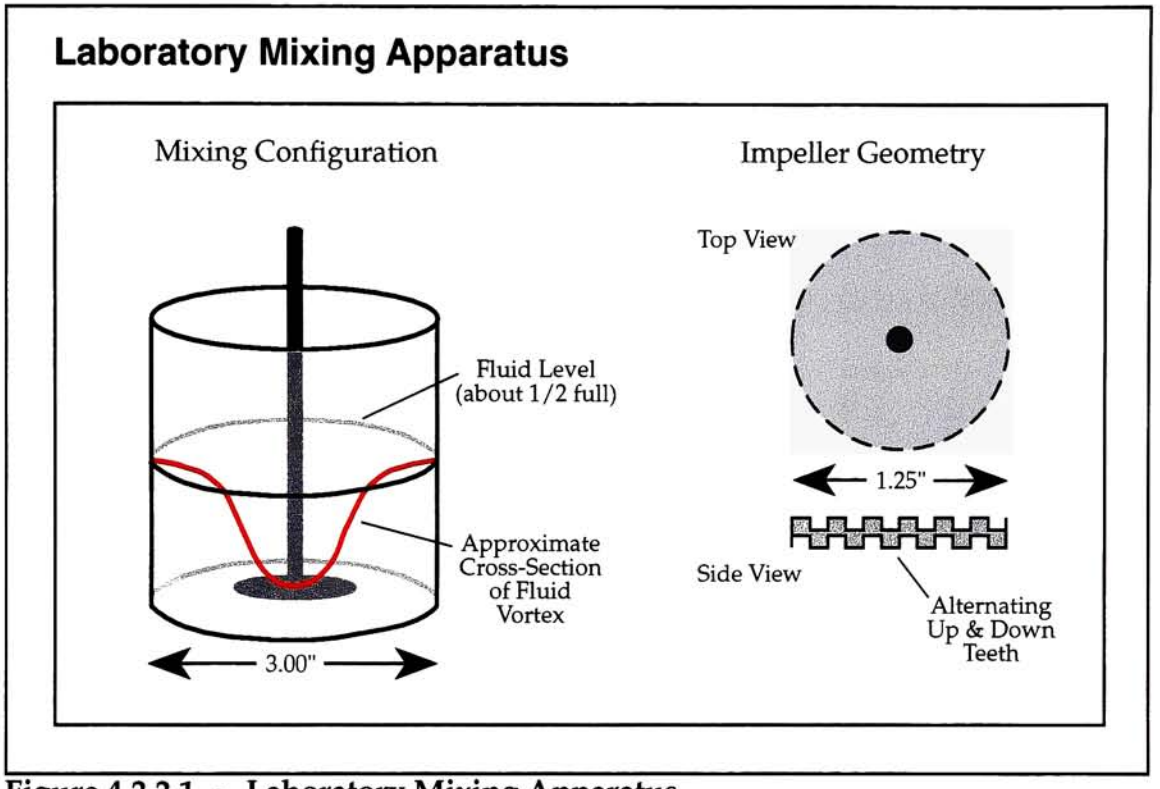

Figure 4.2.2.1 ~ Laboratory Mixing Apparatus.

Release Layers were formulated obeying the same rules as those for the PCL. Again, order of addition was found to be very important, as were drying conditions. Surface tension was found to be a key parameter in optimizing uniform release from PET and adhesion to the receiver sheet. Surface tension (γ), measured in dynes/cm, was determined by applying a thin film of liquid having a known surface tension onto the surface of interest (PET, RL, PCL, or receiver). If the liquid film wetted the surface (i.e. spread to a greater area than the size of the initial film), it was known that γ of the surface in

question was greater than that of the liquid. By using a set of such liquids covering a large range of γ, the γ of all layers was readily quantified.

Coating and printing experiments proved that the surface tension of each of the layers relative to one another was critical. γ_{RL} was leveled with respect to γ_{PET} so that it was only slightly lower. Doing so assured that adhesion of the Release Layer would not be greater than adhesion to the receiver sheet during printing. Further, it assured the RL would coat evenly onto the surface of the PET, without streaking or repellancies. γ_{PTC} was maintained well below γ_{RL} and $\gamma_{receiver}$ so that, on one hand, it would coat evenly onto the Release Layer, and on the other, easily wet the receiver sheet during printing. Figure 4.2.2.2 shows a cross section of the multi-layer ribbon and receiver sheet. Note the surface tensions. Release layer surface tension was controlled via the ratio of Koster Keunen Beesmilk to Johnson Jonwax 120. Photothermal Conversion Layer surface tension was controlled via the quantity of DuPont Zonyl FSJ added to the ink.

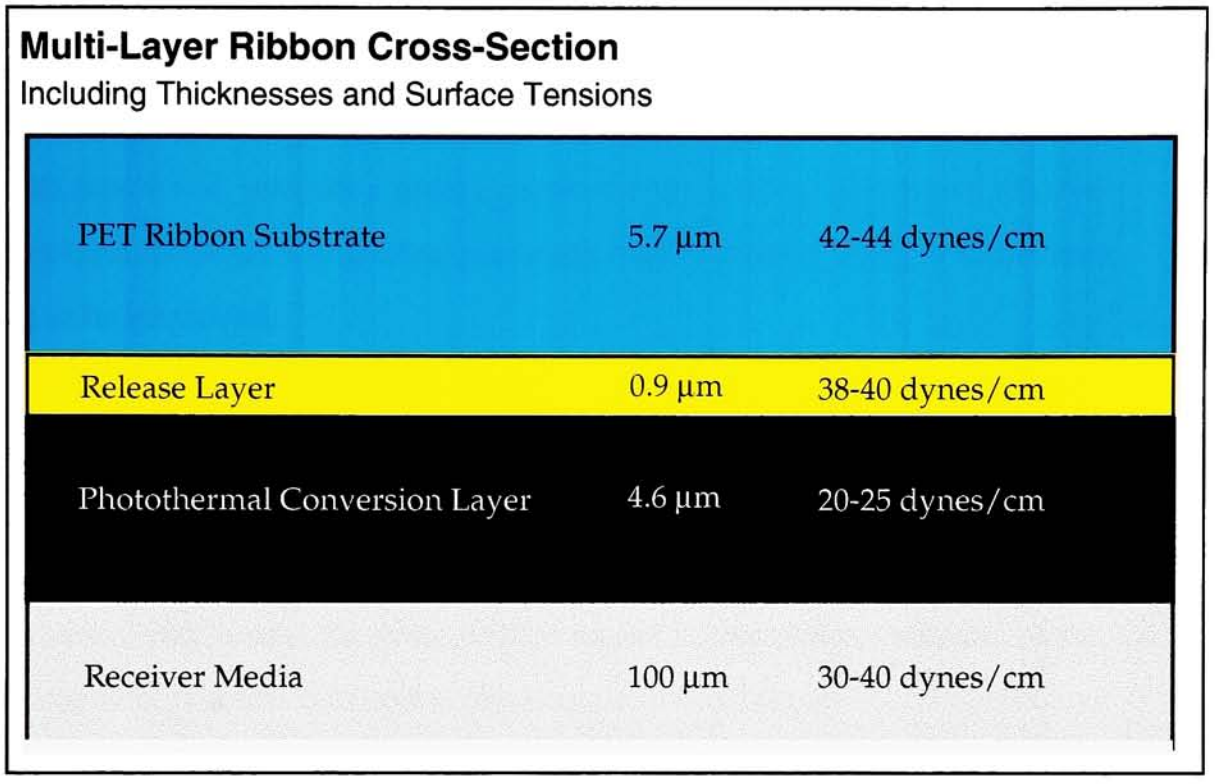

Figure 4.2.2.2 ~ Multi-Layer Ribbon Cross-Section.

Both the RL and PCL were coated via Meyer Rod draw-down method, #7 for RL and #22 for PCL. A set of experiments showed that the data for coating thickness vs. Meyer rod gauge originally obtained for solvent dispersed inks also held for water/alcohol dispersions. Sets of single variable experiments served to determine the appropriate Meyer rods necessary to achieve the desired coating weights given mix viscosities. Release Layer thickness was kept as thin as possible while maintaining coating weight uniformity, as the purpose of this layer was only to allow uniform, efficient release from the PET substrate. Photothermal Conversion Layer thickness

was chosen primarily on the basis of coating uniformity. For carbon black pigmented ribbons, the Meyer rod chosen produced a coating having satisfactory uniformity and minimum thickness. Optical density of the dots, while monitored, was not a great concern for black inks. In order to achieve acceptable densities using other pigments, higher coating weights sometimes had to be employed.

4.3 Measuring and Modeling the Imaging System

With the writing engine, ink ribbon construction, basic ink formulation, and measurement techniques known, it became possible to mathematically model the system. The model, a closed form solution of the Fourier heat transfer differential equation, allowed hundreds of hypothetical situations to be investigated in a fraction of the time that would have been required to empirically test a particular scenario. While the closed form solution imposed some limitations on the accuracy of the model, the fundamental knowledge gained of the printing nip proved invaluable to the completion of the research. The imaging system was modeled as a multi-layer slab heated by a circular disk having a Gaussian spatial energy density profile. The model took into account several parameters of the beam and ink ribbon that are outlined through the following derivation.

4.3.1 Derivation of Writing System Mathematical Model

The wax ink component of the donor ribbon is, at room temperature, a solid with a distribution of temperature at time t given by:

$$v = f(x,y,z,t). \qquad (1)$$

It is possible to perceive a surface within the ink that, at any instant, will have uniform temperature v at every point. Such a surface is known as an isothermal surface of the temperature v; it may be viewed as a boundary between regions within the wax that are warmer and cooler than v. If one had a means of measuring various points within the wax instantaneously, plotting the readings, and connecting points of equal temperature, the result would be a map of the isothermal lines, or isotherms. There are no rules governing the formation of isotherms save that they may not intersect one another. Any one point may not have two temperatures at once. Such a solid having "...structure and properties in the neighborhood of any point the same relative to all directions through the point..." (Carslaw et al, 1959) is known as an isotropic solid. It is this concept of an isotropic solid that the mathematical model of the imaging process is founded upon. Because the heat capacity of the wax/resin varies somewhat as a function of temperature around T_m/T_g, the ink is not isotropic at these temperatures. Although the model assumes constant heat capacity over all temperatures, it proved to be a sufficient first order approximation for the materials used. This topic is discussed with more detail later in this section.

When pigment in the photothermal conversion layer (PCL) absorbs incident IR laser radiation, it absorbs a percentage and re-emits it as heat with some effective efficiency. The binder particles local to the irradiated pigment aggregate will rise in temperature v as a continuous function of (1). With l

the distance between the plane faces of the PCL, ρ and c the average density and specific heat of the mixture, and w an infinitesimal segment of the wax, the rate at which the material gains heat is

$$\rho cwl\frac{\partial v}{\partial t}. \qquad (2)$$

As the incident beam heats the wax, a heat flow gradient is set up. The heat flow rate through the material, from one face to the other, may be represented as

$$f_1 l - f_2 l = l(f_1 - f_2). \qquad (3)$$

Equating (2) and (3) reveals

$$f_1 - f_2 = \rho cw\frac{\partial v}{\partial t}. \qquad (4)$$

Note that the above derivation does not require the thermal properties to be continuous, only finite. This fact is important, as it validates the assertion that the heat flux is continuous at the surface of separation of two layers (Carslaw et al, 1959), such as the interface between the PCL and release layer or PCL and receiver sheet.

The PCL has been modeled as an homogeneous isotropic solid whose thermal conductivity is independent of temperature. Thermal conductivity K of a material of thickness d may be empirically calculated by measuring the quantity Q of heat passed through the surface of the material within some length of time t. Opposing sides of the slab are initially at differing temperatures $v1$ and $v2$. An imaginary disk of surface area S is placed normal to the face of lower temperature and the radiating heat over this area measured. Figure 4.3.1.1 illustrates this arrangement.

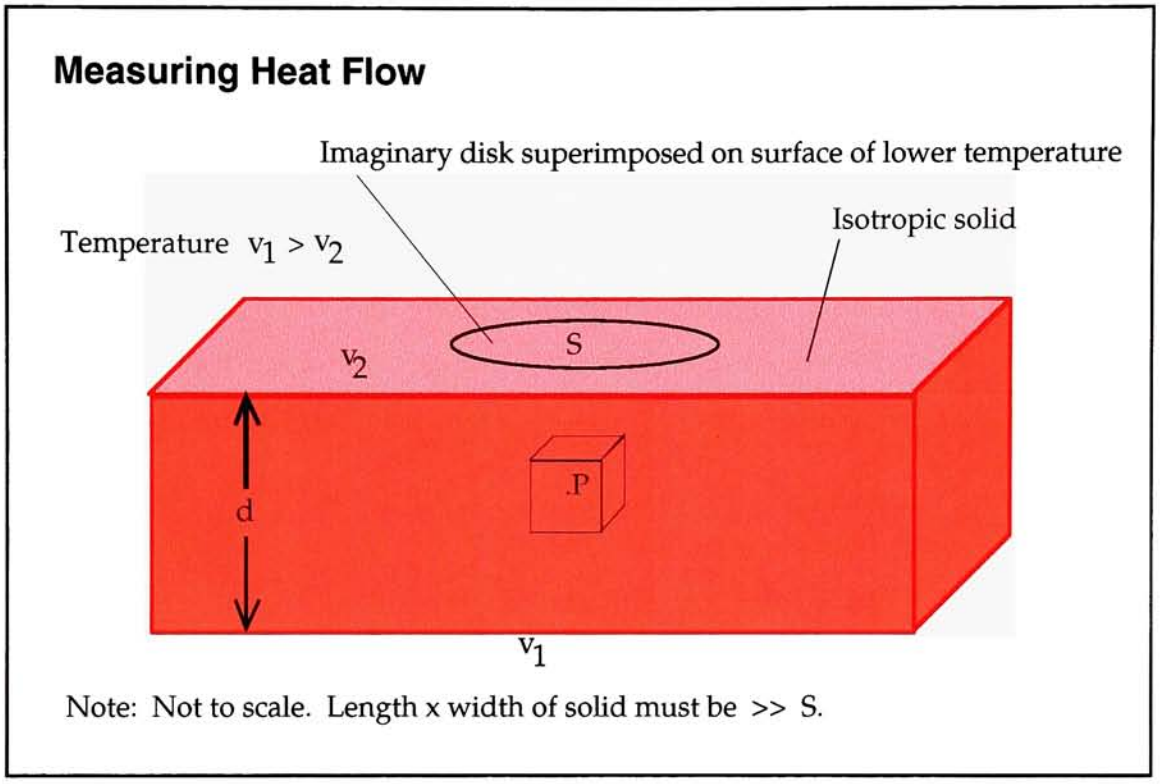

Figure 4.3.1.1 ~ Measuring Heat Flow.

Once a steady state has been reached,

$$Q = \frac{K(v_1 - v_2)St}{d} \qquad (5)$$

where K is the Thermal Conductivity constant, a quantity varying primarily with material. While there is actually a slight dependence on temperature, it is most often neglected with no adverse effects. "In the ordinary mathematical theory it is assumed that the conductivity does not vary with temperature" (Carslaw et al, 1959). When a change of state is involved, this assumption must be scrutinized. The waxes and resins comprising the ink

did undergo a change in heat capacity when they changed phase or passed through their glass transition, a fact which was kept in mind during analysis of the model's output.

In the case of a heated block of homogeneous material, the isotherms are planes parallel to the faces of the slab and normal to the direction of the heat flux. Given (5) and two isotherms for temperatures v and $v + \partial v$ a distance ∂x apart, the rate of flow of heat, per unit time per unit area, may be represented by

$$-K\frac{\partial v}{\partial x}. \tag{6}$$

Taking the limit as $\partial x \to 0$ reveals the equation of heat flux

$$f_x = -K\frac{\partial v}{\partial x}. \tag{7}$$

The differentiation may be applied to any axis drawn outward normal from the isotherm, yielding

$$f_n = -K\frac{\partial v}{\partial n}. \tag{8}$$

which proposes that heat flow from the inside to the outside of an isothermal surface per unit area per unit time is equal to the heat flux in that direction. This result is widely accepted as the one hypothesis fundamental to mathematical theory of the conduction of heat (Carslaw et al, 1959; Chapman, 1974; Thomas, 1993). The isothermal PCL has then three-dimensional thermal fluxes of

$$f_x = -K\frac{\partial v}{\partial x}, \tag{9}$$

$$f_y = -K\frac{\partial v}{\partial y}, \tag{10}$$

and $$f_z = -K\frac{\partial v}{\partial z}. \tag{11}$$

A fundamental gradient vector f may be introduced using (9), (10), and (11) (Carslaw et al, 1959).

$$f = -K\nabla v. \tag{12}$$

Consider the point P in figure 4.3.1.1 above. The infinitesimal element surrounding it has dimensions dx, dy, and dz. The rate of heat gain from flow through the x-dimension of the rectangular parallelepiped is given by

$$-dxdydz\frac{\partial f_z}{\partial z}. \tag{13}$$

For the three-dimensional model, the flux over all axes must be added, yielding the total rate of heat gain

$$-(\frac{\partial f_x}{\partial x} + \frac{\partial f_y}{\partial y} + \frac{\partial f_z}{\partial z})dxdydz \tag{14}$$

which is also given by recasting (2) in three-dimensional differential form

$$\rho c\frac{\partial v}{\partial t}dxdydz. \tag{15}$$

Equating (14) and (15) gives

$$\rho c\frac{\partial v}{\partial t} + (\frac{\partial f_x}{\partial x} + \frac{\partial f_y}{\partial y} + \frac{\partial f_z}{\partial z}) = 0, \tag{16}$$

which holds for all points within the PCL, except those supplied heat directly by the laser beam. Substituting (9), (10), and (11) into (16) reveals

$$\frac{\partial^2 v}{\partial x^2} + \frac{\partial^2 v}{\partial y^2} + \frac{\partial^2 v}{\partial z^2} - \frac{1}{k}\frac{\partial v}{\partial t} = 0, \text{ where } k = \frac{K}{\rho c}. \tag{17}$$

While Kelvin referred to the constant k as Diffusivity, James Clerk Maxwell termed it Thermometric Conductivity.

Conventional thermal transfer utilizes rectangular heating elements, so the cartesian coordinate system best fits that case. It was found that the laser exposure system of LT2, however, has a profile best described within the polar coordinate system. For modeling purposes, the ideal spatial pulse profile would be a delta function. In a case where the wax layer is much thicker than the beam is wide, such an approximation would be valid. In this case, the beam diameter is more than six times greater than the thickness of the wax layer (30 μm vs. 4.6 μm), making such an approximation wholly inappropriate. Keeping the ratio of the beam diameter to the PCL thickness in mind, the ideal beam profile to model would be cylindrical, with a uniform intensity distribution over a circular area. A series of measurements confirmed that this was not the case.

The measurements of the pulse intensity profile outlined in section 4.1.5 confirmed that a Gaussian spot function would adequately describe the incident laser beam. With the beam tuned for radial symmetry, it could be modeled as in the "Actual" case presented in Figure 4.3.1.2. As pointed out in section 4.1.6, it is important to note that had the pulse not possessed the sloping, continuous profile characteristic of the Gaussian shape, modulating dot size would have been significantly more difficult.

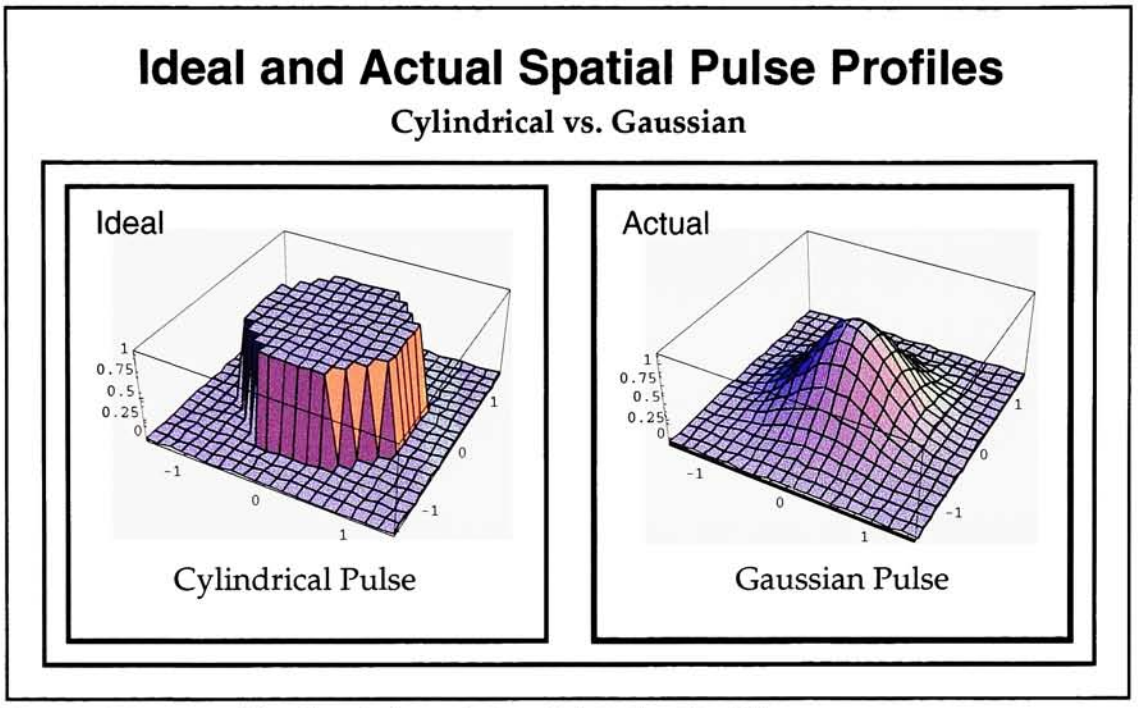

Figure 4.3.1.2 ~ *Ideal* and Actual Spatial Pulse Profiles.

Given the above results, in order to simplify model calculations, (17) may be transformed from Cartesian coordinates to polar. The common identities

$$x = r\cos\theta, \tag{18}$$

$$y = r\sin\theta, \tag{19}$$

and $$ds^2 = dr^2 + rd\theta^2 + dz^2 \tag{20}$$

allow (17) to be recast as

$$\frac{\partial v}{\partial t} = k\left(\frac{\partial^2 v}{\partial r^2} + \frac{1}{r}\frac{\partial v}{\partial r} + \frac{1}{r^2}\frac{\partial^2 v}{\partial \theta^2} + \frac{\partial^2 v}{\partial z^2}\right). \tag{21}$$

The aforementioned empirical measurements of the spatial pulse shape guaranteed that the pulse could be treated as a series of disks of varying intensities having radial symmetry about the z-axis. Therefore, initial and boundary conditions are independent of θ, and (21) simplifies to what is commonly referred to as *the equation of conduction of heat,* cast in polar coordinates

$$\frac{\partial v}{\partial t} = k\left(\frac{\partial^2 v}{\partial r^2} + \frac{1}{r}\frac{\partial v}{\partial r} + \frac{\partial^2 v}{\partial z^2}\right) . \qquad (22)$$

The applied temperature gradient on the left side of (22) represents the rate at which energy is applied to the system. In order to model the system, it again became important to quantitatively determine this gradient. In the ideal case, energy would be applied to the ribbon uniformly for a known period of time, then switched off. The measurements of temporal pulse shape outlined in section 4.1.5 confirmed that, indeed, the rate at which the laser applied heat was uniform. Put another way, the temporal profile was rectangular, yielding an applied radiation gradient of zero. Applying these conditions to (22) yields a simplified equation for the conduction of heat in the PCL:

$$\frac{\partial^2 v}{\partial r^2} + \frac{1}{r}\frac{\partial v}{\partial r} + \frac{\partial^2 v}{\partial z^2} = 0 . \qquad (23)$$

The above representation, Laplace's equation cast in polar coordinates, models the conduction of heat as applied to the PCL via the IR laser over the spatial width of its pulse $0 \leq a \leq r$ in the plane $z = 0$ at a rate dependent only on the radius r.

Equation (23) may be solved via the separation of variables technique so that

$$v(r,z) = F(r)G(z). \tag{24}$$

Substituting into (23) and collecting like terms produces

$$FG'' + G(\frac{1}{r}F' + F'') = 0. \tag{25}$$

An arbitrary constant λ may be chosen such that

$$-\frac{G''}{G} = \frac{1}{F}(\frac{1}{r}F' + F'') = -\lambda^2 \Rightarrow G'' - G\lambda^2 = 0, \tag{26}$$

which may be recast as

$$F'' + \frac{1}{r}F' + F\lambda^2 = 0. \tag{27}$$

In equation (27), F(r) is a Bessel function of order zero and may be represented by $J_0(\lambda r)$. In terms of $G(z)$, the general solution to (26) is

$$G' = C_1 e^{-\lambda z} + C_2 e^{\lambda z}, \tag{28}$$

the second term of which fortunately equals zero in this case. Plugging the results of (27) and (28) into (24) reveals

$$v(r,z) = Ce^{-\lambda z} J_0(\lambda r) \tag{29}$$

which is valid for any λ. Integrating over all λ will solve (29) so long as $f(\lambda)$ is chosen to satisfy the boundary conditions at $z = 0$:

$$v = \int_0^\infty Ce^{-\lambda z} J_0(\lambda r) f(\lambda) d\lambda. \tag{30}$$

Referring to the conditions imposed on (23), the criteria that must be met is given by (11), where

$$-2K\left[\frac{\partial v}{\partial z}\right]_{z=+0} = Q, \quad 0 < r < a; \quad = 0 \text{ otherwise}. \tag{31}$$

Equating (30) and (31) yields

$$v = \frac{Q}{2KC}\int_0^\infty e^{-\lambda z} J_0(\lambda r)\lambda f(\lambda)d\lambda, \quad 0 < r < a; \quad z = +0. \tag{32}$$

Choosing $f(\lambda)$ appropriately is the key to the derivation of the model. While a valid function may be derived through several techniques including those relying upon Fourier integrals and Neumann's integral theorem, the use of a well known integral involving yet another Bessel function yields the most interesting solution:

$$\int_0^\infty J_0(\lambda r)J_1(\lambda a)d\lambda = \begin{cases} 0, & r > a \\ 1/2a, & r = a \\ 1/a, & r < a \end{cases}. \tag{33}$$

Using (33) as a model and substituting for λf(λ) produces

$$v = \frac{Qa}{2KC}\int_0^\infty e^{-\lambda z} J_0(\lambda r)J_1(\lambda a)\frac{d\lambda}{\lambda}. \tag{34}$$

Note, at this point, the model has no dependence on time. Equation (34) returns the temperature v of a point at or below the surface of the spot on the PCL irradiated *continuously* by the laser beam. Carslaw and Jaeger published in 1959 a generalization of (34), which is of singular importance to the model's derivation, as their particular solution adds the necessary time dependence:

$$v = \frac{Qa}{2KC}\int_0^\infty J_0(\lambda r)J_1(\lambda a)\left\{e^{-\lambda z}erfc\left[\frac{z}{2(kt)^{1/2}} - \lambda(kt)^{1/2}\right] - e^{\lambda z}erfc\left[\frac{z}{2(kt)^{1/2}} + \lambda(kt)^{1/2}\right]\right\}\frac{d\lambda}{\lambda}. \tag{35}$$

In (35), Q represents the rate per unit time per unit area at which energy is applied. In the case of the investigated laser heating, while the laser is irradiating the ribbon, the rate is independent of time and of angle, but is

dependent on radial position according to the beam's Gaussian profile, as explained above. Therefore, Q may be defined as

$$Q = \frac{2P}{\pi a^2} e^{-2r^2/a^2} \tag{36}$$

where P, the power incident on the plane of the PCL, was measured as in section 4.1.5.

The efficiency with which the laser heats a layer depends on the absorption coefficient of the material. Absorption coefficients at the laser's wavelength for both PET and RL were found to be zero, using FT-IR spectroscopy. The absorption coefficient α for the PCL was added to the model so that

$$v = \frac{Qa}{2KC} \int_0^\infty J_0(\lambda r) J_1(\lambda a) \left\{ e^{-\lambda \alpha z} erfc\left[\frac{\alpha z}{2(kt)^{1/2}} - \lambda (kt)^{1/2} \right] - e^{\lambda \alpha z} erfc\left[\frac{\alpha z}{2(kt)^{1/2}} + \lambda (kt)^{1/2} \right] \right\} \frac{d\lambda}{\lambda}$$

where $Q = \frac{2P}{\pi a_b^{\,2}} e^{-2r^2/a^2}$.

(37)

As the beam passed through the PET substrate and RL, it was slightly scattered. The amount of scatter was quantified by placing these two layers over the aperture of the beam diameter measuring device and observing the *blurring* effect. The scatter did not degrade the Gaussian nature of the beam, but it did widen the profile significantly. The PET widened the beam by a factor of 1.30; the RL widened the beam by a factor of 1.05. These factors were incorporated into the model in the following manner:

$$v = \frac{Qa_b}{2KC}\int_0^\infty J_0(\lambda r)J_1(\lambda a_b)\left\{e^{-\lambda\alpha z}erfc\left[\frac{\alpha z}{2(kt)^{1/2}} - \lambda(kt)^{1/2}\right] - e^{\lambda\alpha z}erfc\left[\frac{\alpha z}{2(kt)^{1/2}} + \lambda(kt)^{1/2}\right]\right\}\frac{d\lambda}{\lambda}$$

where $Q = \frac{2P}{\pi a_b^{\,2}}e^{-2r^2/a_b^2}$ and $a_b = f_{PET}f_{RL}a$.

(38)

4.3.2 Applying the Writing System Mathematical Model

Once derived, the model was coded in Wolfram Research's Mathematica, version 2.2, and evaluated for hundreds of theoretical *systems*. For these calculations, characteristics given in Table 4.3.2.1 were used. The 1.064 μm α values given in the table were obtained through use of a Perkin-Elmer FT-IR Spectroscope. Aside from the c values for the RL and PTCs, the K, c, and ρ values presented in Table 4.3.2.1 were gathered from Gregory, 1991, Carslaw et. al., 1959, Bennet, 1956, and Tolbert et. al., July/August, 1993. Specific heat values for the Release and Photothermal Conversion Layers were calculated using the following formula, derived from an equation for the specific heat of paraffin wax given in Bennet, 1956:

$$c = C_b(0.492 + 0.0009v) + (1 - C_b)c_p \ . \qquad (39)$$

where C_b is the binder concentration neglecting solvent, v is the temperature of the layer of interest (RL or PCL), and c_p is the specific heat of the pigment.

Ribbon Characteristics at 150 °C and 1.064 μm

Layer	Thickness d μm	Thermal Conductivity K 1/(μm μsec K)	Specific Heat c 1/g K	Density ρ g /μm^3	Diffusivity k μm^2/μsec	Absorption Coefficient α
PET	5.7	1.4 e-13	1.3	1.4 e-12	0.077	0.00
RL	0.9	.50 e-13	.63	.92 e-12	0.087	0.00
PCL (CB)	4.6	.55 e-13	.56	1.1 e-12	0.090	2.58
PCL (IR165)	4.6	.48 e-13	.63	.99 e-12	0.077	1.27
Receiver	100	.60 e-13	1.2	1.0 e-12	0.050	•

Table 4.3.2.1 ~ Ribbon Characteristics at 150°C and 1.064 μm.

A few important scenarios served to describe the actual imaging process and are presented here. In the first case, Figures 4.3.2.1 and 4.3.2.2, show decreasing temperature as a function of depth into the PCL for a set of exposure parameters commonly used. Note that the temperature is very high at the RL/PCL interface (z = +0 μm) but decreases rapidly through the wax ink. At the PCL/receiver interface (z = +4.6 μm), the temperature profile predicts that a 35-40 μm dot will be formed. This determination can be made by observing Figure 4.3.2.2 while using Figure 6.0.1, the Pseudo Color Look Up Table to determine the threshold transfer temperature. Note that the threshold transfer temperature of the PCL is considerably above its melting point, as the wax must be in a highly liquid, low viscosity state in order to transfer to the microporous substrate. Figure 4.3.2.3 illustrates the modeled pulse used to generate the above temperature distributions.

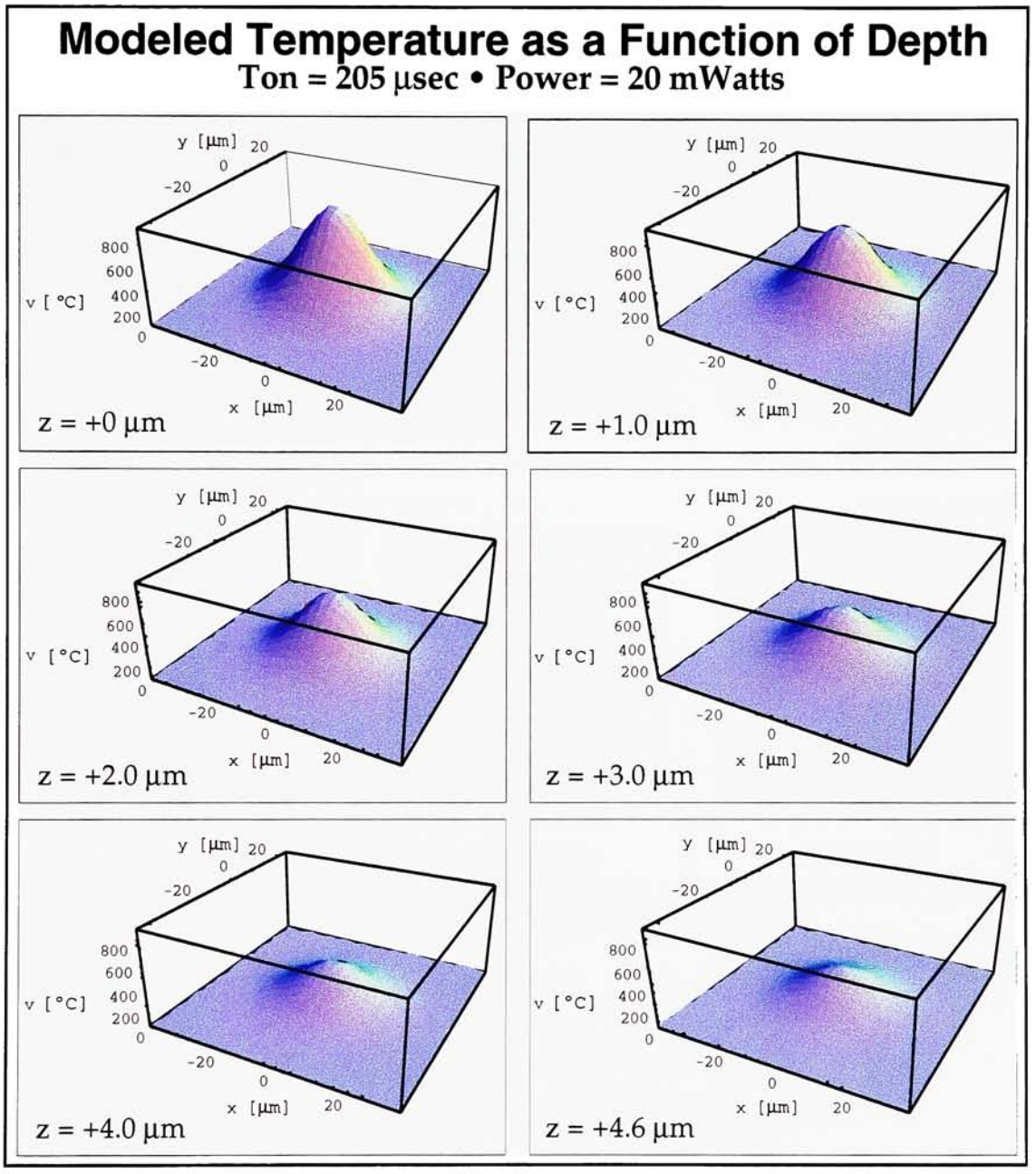

Figure 4.3.2.1 ~ Modeled Temperature as Function of Depth.

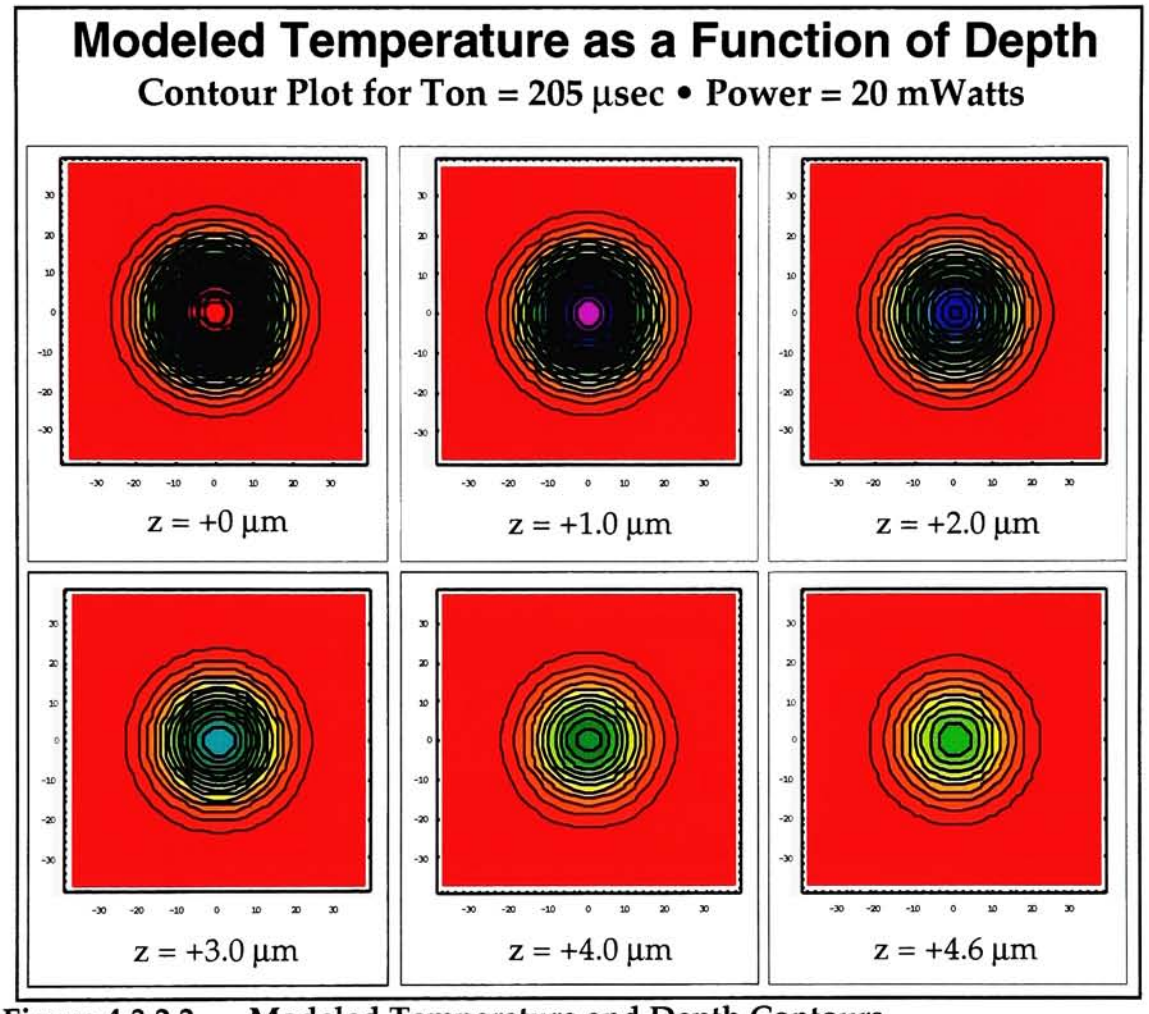

Figure 4.3.2.2 ~ Modeled Temperature and Depth Contours.

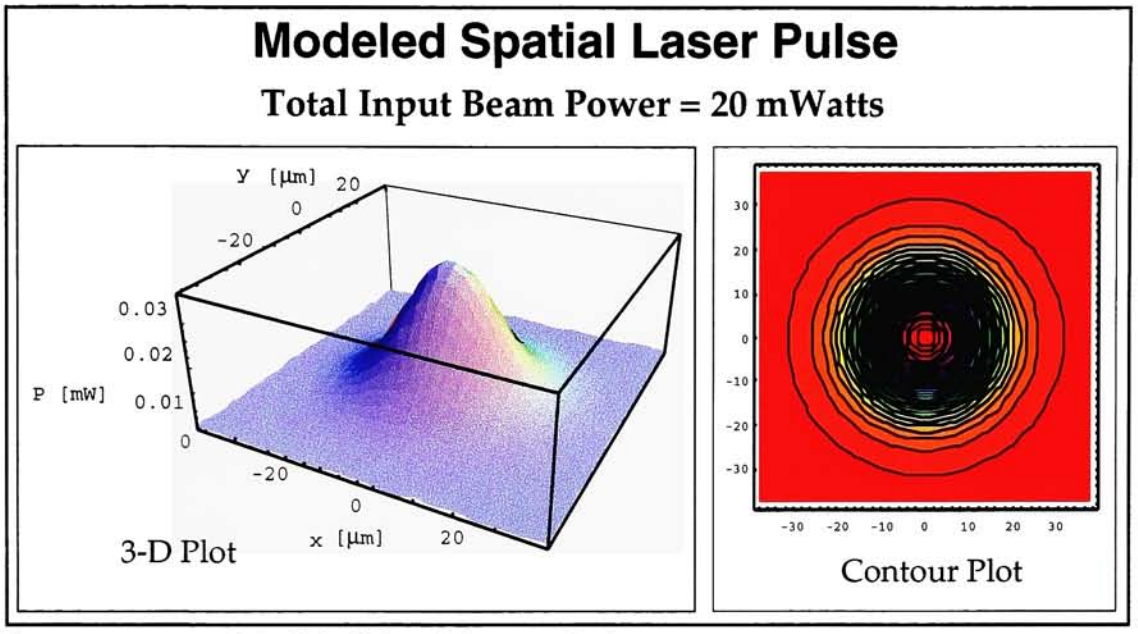

Figure 4.3.2.3 ~ Modeled Spatial Laser Pulse.

While heat is generated only in the PCL, the heat generated propagates both forward and backward. Figure 4.3.2.4 shows that the RL is very hot at the interface to the PET substrate. At the rear surface of the PET, the temperature is still above 230 °C, right around the T_g of the PET used ($T_g \approx 235$ °C). These exposure conditions represent the absolute maximum conditions of exposure. Beyond this point, the ribbon materials began to vaporize; holes were created through the PET. In practical application, thicker PET may be desirable as long as the optical quality is high enough so that blurring and absorption of the laser wavelength are not too great.

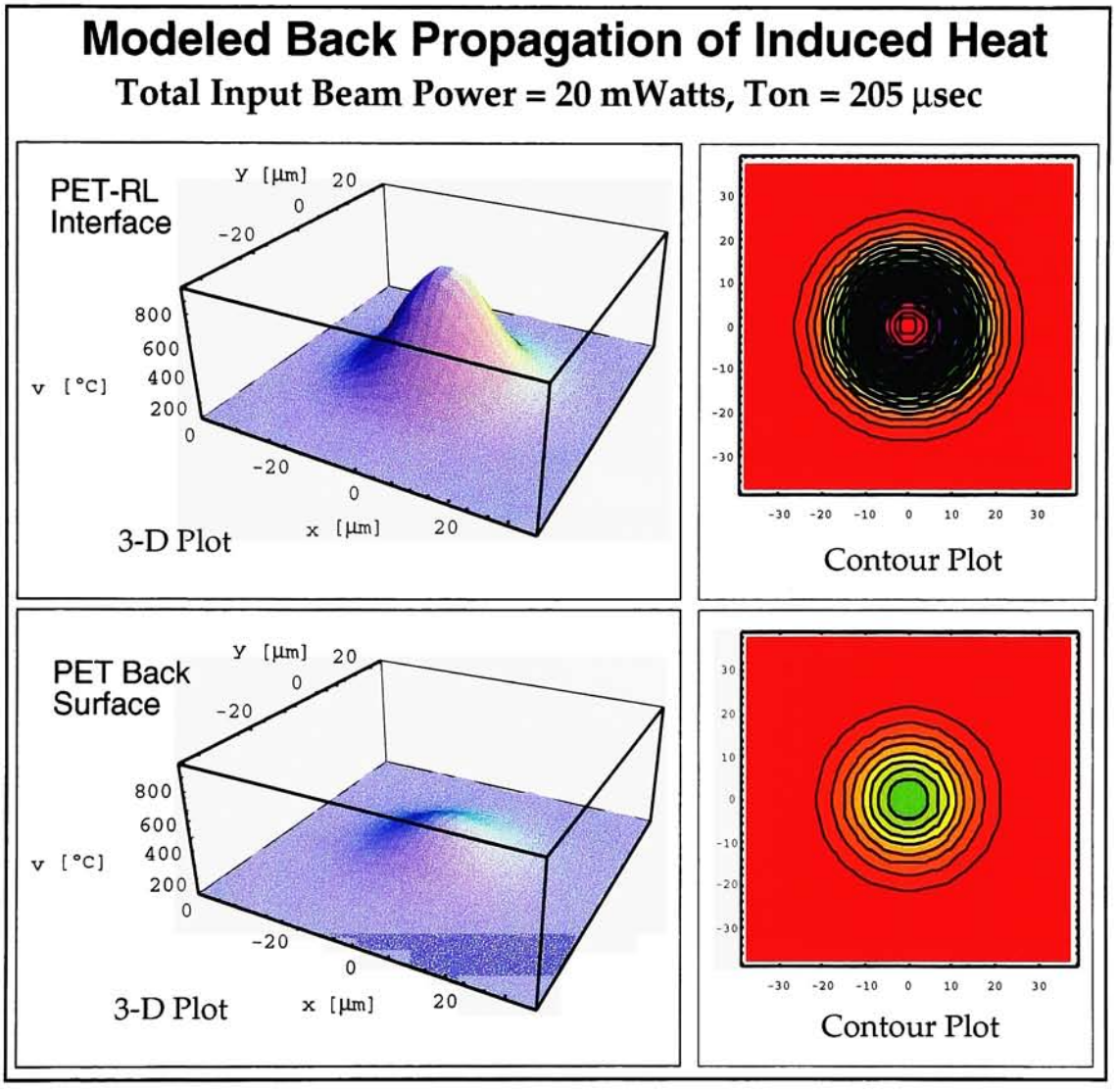

Figure 4.3.2.4 ~ Modeled Heat Back Propagation.

Pushing laser output higher and using shorter exposure times theoretically would increase imaging speed, based on the assumption that the reciprocal relationship Energy Density = Pulse Amplitude × Pulse Duration holds true. As in photography, however, such is true for LT2 until the

reciprocal relationship fails. At exposure times below 100 μsec, the pulse required to generate enough heat to transfer wax causes vaporization of the ribbon rather than melting of wax. As can be seen in Figure 4.3.2.5, for a pulse width of 1.0 μsec and an amplitude of 300 mWatts, the temperature at the RL/PCL interface is approaching vaporization. Within 0.1 μm of this point, temperature has dramatically decreased. At the PCL/receiver interface, there is no trace of an elevation in temperature. The model predicts the only way to transfer wax using such short exposure times is either to use ultra thin layers of wax or to use a higher power laser and ablate the wax to the receiver, as in LAT.

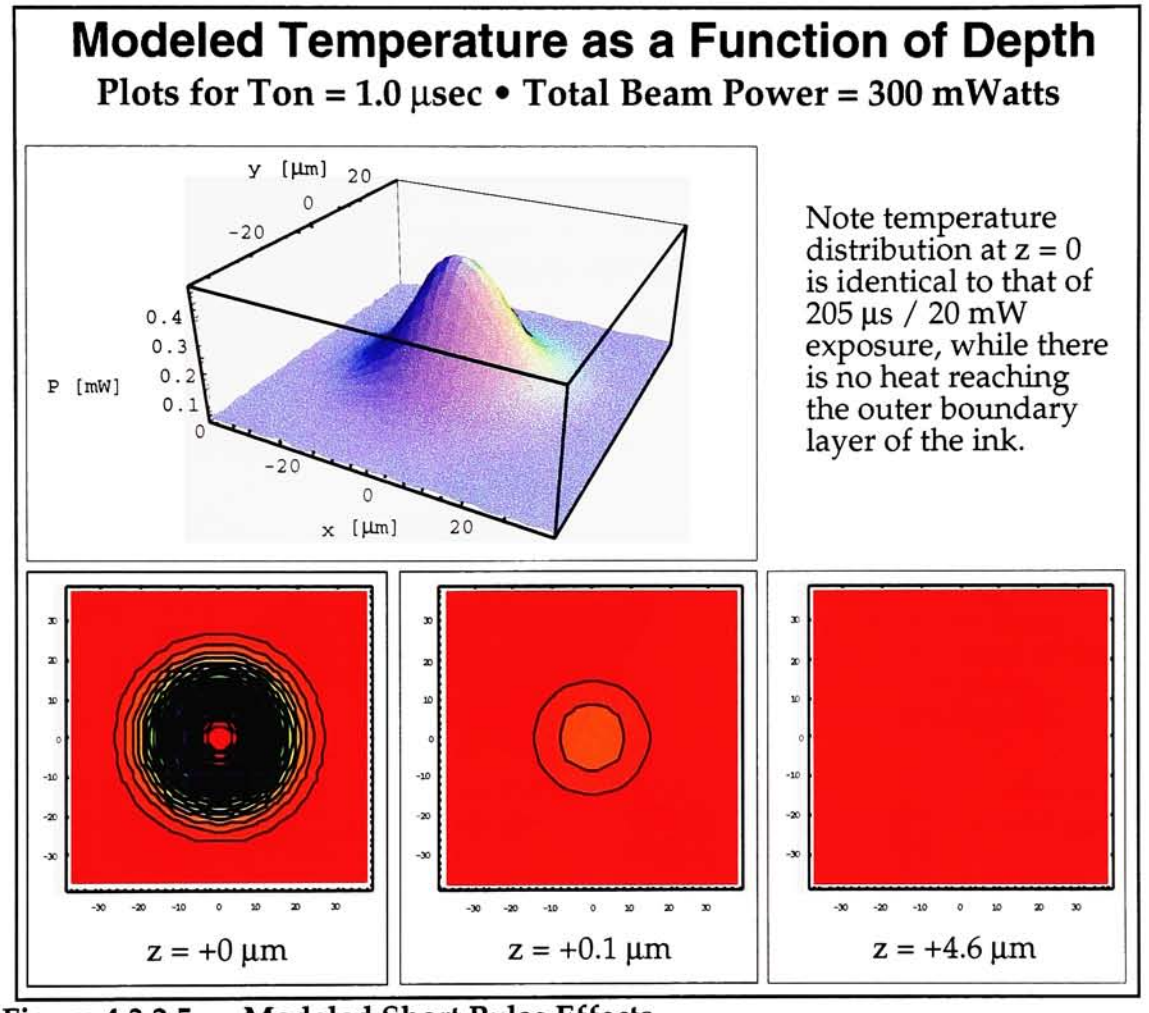

Figure 4.3.2.5 ~ Modeled Short Pulse Effects.

An exposure of 100 μsec with a pulse amplitude of 30 mWatts represents imaging conditions near the limit of the designed process. Figure 4.3.2.6 shows that at a depth of 4.6 μm, the PCL/receiver interface, the temperature profile dictates a dot on the order of 20 μm would print. By keeping this power constant and varying pulse width, smaller dots would be achievable. Figure 4.3.2.7 illustrates this concept using a 20 mWatt pulse. By

varying the exposure time, it is possible to achieve variable dot sizes. In section 4.6, photomicrographs of printed dots are presented that show such dot size modulation is indeed possible.

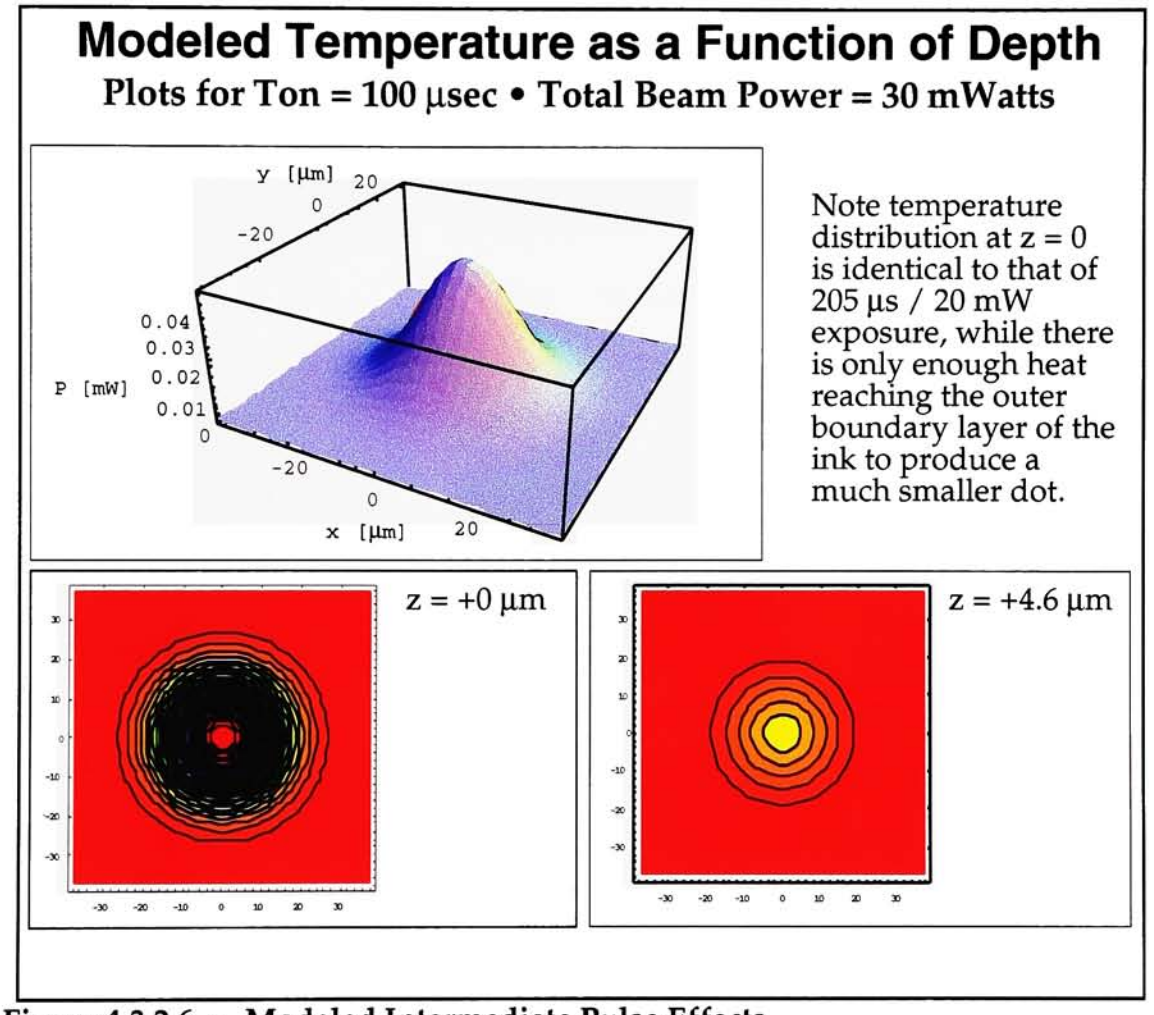

Figure 4.3.2.6 ~ Modeled Intermediate Pulse Effects.

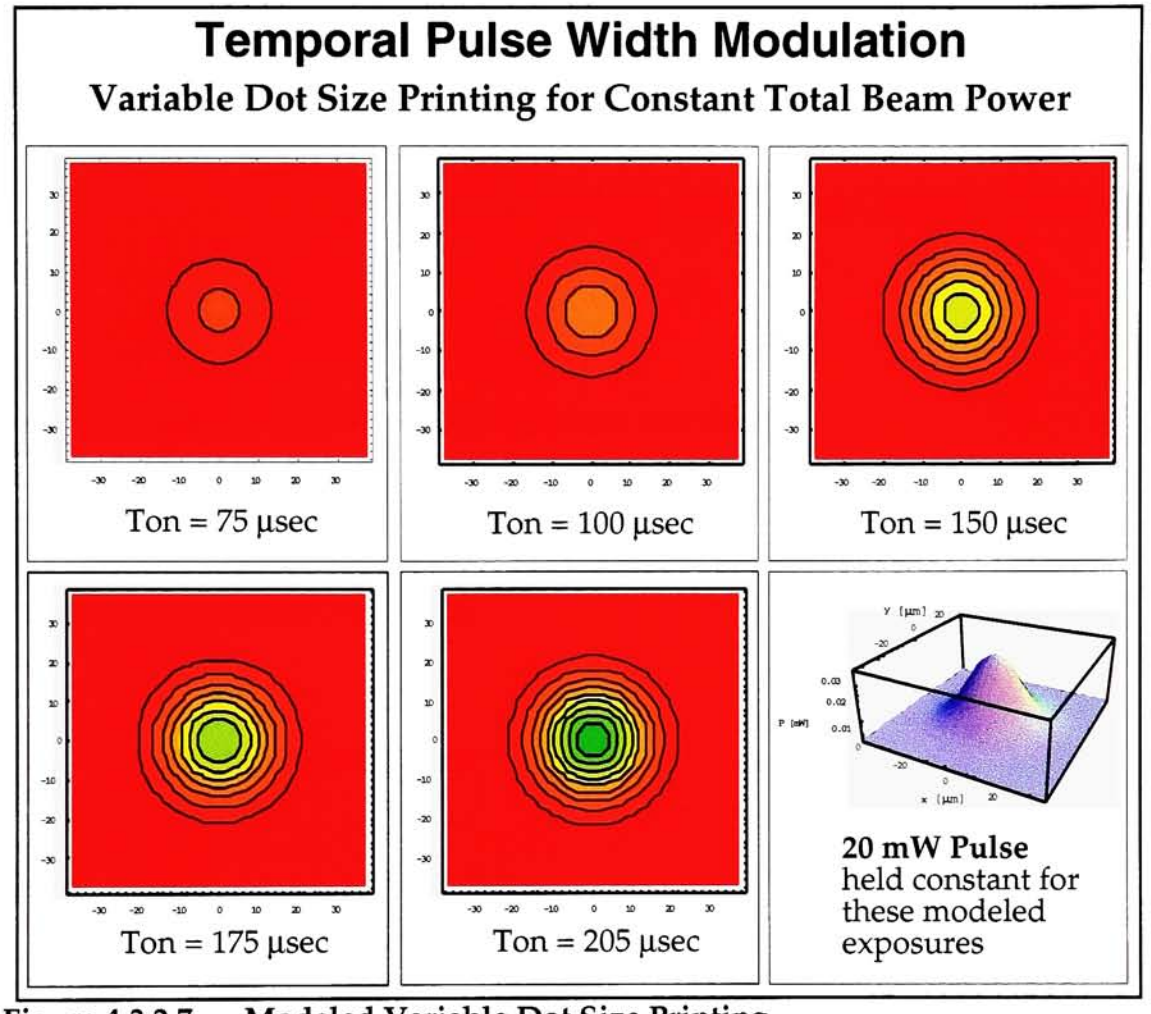

Figure 4.3.2.7 ~ Modeled Variable Dot Size Printing

4.3.3 A Second Approach to LT2 Heating and Cooling

In order to look at the temperature profile of the heated spot over an extended period of time, the heating and cooling process was modeled as a steady state, periodic function, under the assumption that the duty cycle of the pulse was 50%. This approach was taken in order to gain knowledge of the process without investing enormous amounts of time doing so. Drawing

from a derivation of the temperature fluctuations of the Earth's crust caused by the Sun (Carslaw et al, 1959), the model derivation follows.

Following the logic of section 4.3.2, any point heated by the laser beam may be modeled as

$$\frac{\partial^2 v}{\partial x^2} - \frac{1}{k}\frac{\partial v}{\partial t} = 0, \text{ where } k = \frac{K}{\rho c} \ . \tag{40}$$

For a periodic system, the desired solution has the form

$$v = ue^{i(\omega t - \varepsilon)} \tag{41}$$

where u is a function of x only. Of course, the period of this solution is $2\pi/\omega$. Substituting (40) into (39) yields

$$\frac{\partial^2 u}{\partial z^2} = \frac{i\omega}{k}u \ . \tag{42}$$

This equation may be solved by

$$u = Ae^{-z\sqrt{i\omega/k}} \tag{43}$$

which leads to the solution of (40):

$$v = Ae^{-z\sqrt{\omega/2k}} \begin{matrix}\cos \\ \sin\end{matrix}\left\{\omega t - \varepsilon - z\sqrt{\omega/2k}\right\} \ . \tag{44}$$

Desiring $A\cos(\omega t - \varepsilon)$ at $z = 0$ forces the particular solution

$$v = Ae^{-z\sqrt{\omega/2k}} \cos\left(\omega t - \varepsilon - z\sqrt{\omega/2k}\right) \ . \tag{45}$$

An equation describing the input temperature as a periodic function of the time (of period $2\pi/\omega$) may be given by the Fourier expansion:

$$p(t) = A_0 + A_1\cos(\omega t - \varepsilon_1) + A_2\cos(\omega t - \varepsilon_2) + \ \ldots \tag{46}$$

which, when combined with (43), yields the resulting temperature

$$v = A_0 + \sum_{n=1}^{\infty} A_n e^{-\alpha z\sqrt{n\omega/2k}} \cos(n\omega t - \varepsilon_n - x\sqrt{n\omega/2k}) \ . \tag{47}$$

Using the square temporal pulse (defined above) at 50% duty cycle as the periodic input, so that

$$\begin{aligned} &p(t) = V \text{ for } 2rT_{on} < t < (2r+1)T_{on} \\ &p(t) = 0 \text{ for } (2r+1)T_{on} < t < (2r+2)T_{on} \\ &\text{where } T_{on} \text{ is the length of the input pulse} \\ &\text{for } r = 0,1,2, \ldots \end{aligned} \quad , \tag{48}$$

produces the input function

$$p(t) = \frac{V}{2} + \frac{2V}{\pi}\sum_{n=0}^{\infty}\frac{1}{(2n+1)}\sin\left[\frac{(2n+1)\pi t}{T_{on}}\right] \quad . \tag{49}$$

Following (44) and (45), the output of this model is then

$$v = \frac{V}{2} + \frac{2V}{\pi}\sum_{n=0}^{\infty}\frac{1}{(2n+1)}e^{-\alpha z\sqrt{(2n+1)\pi/2kT_{on}}}\sin\left[\frac{(2n+1)\pi t}{T_{on}} - z\left\{\frac{(2n+1)\pi}{2kT_{on}}\right\}^{1/2}\right] \quad . \tag{50}$$

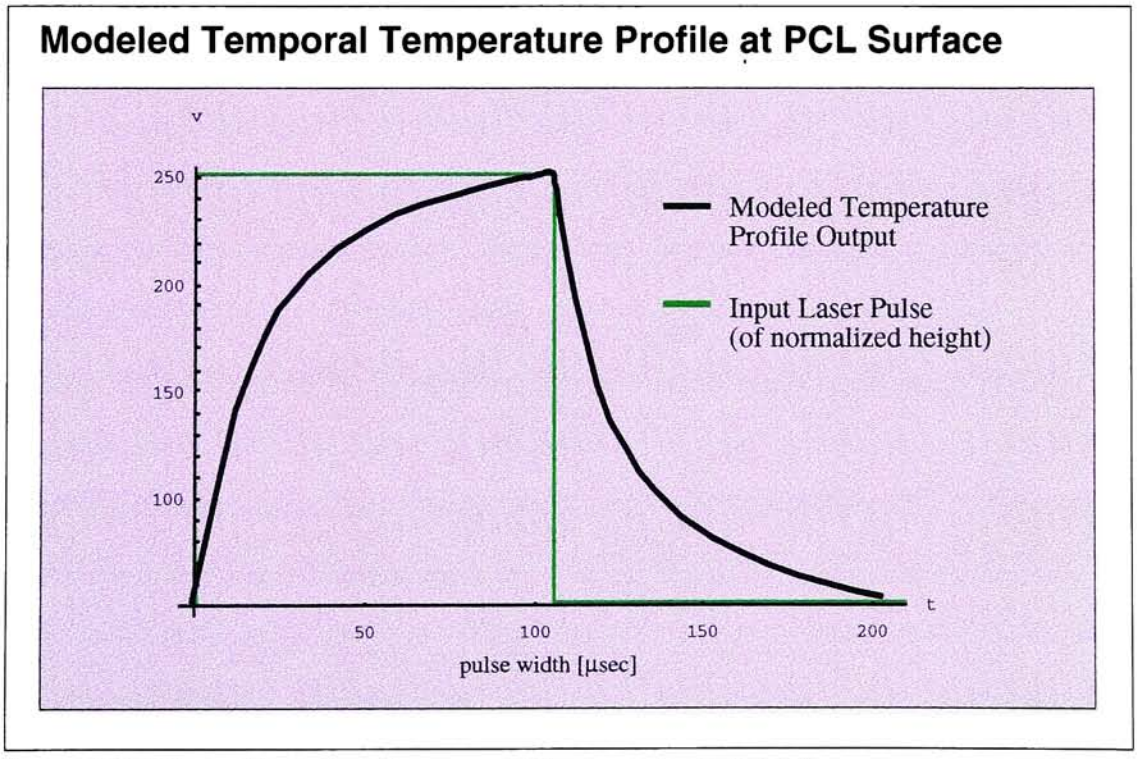

Figure 4.3.3.1 ~ Modeled Temporal Temperature Profile.

Figure 4.3.4.1 graphically illustrates the temperature profile for one set of input parameters, namely those at the interface between the RL and PCL. The large thermal inertia of the system at this depth beneath the ribbon surface slows both the rise and fall of temperature. The model predicts no such lag at the surface of the substrate. Indeed, at a depth of z = 0, the model's input and output functions are of identical shape. The time required by the ink to attain the threshold transfer temperature is a function of the thickness of the ribbon layers as well as their composition. The most significant point raised by this model is the importance of high efficiency IR absorbers and ink pigments.

4.3.4 Limitations of Writing System Mathematical Model

As mentioned earlier, in reality the wax is isotropic until it changes its state from solid to liquid or vice versa. As the wax melts (or resin passes through its T_g, the conditions of isotropicity are not met at the interface between the solid and liquid phases. The proposed model therefore approximates the physical situation less accurately as the melting point is reached. Once the wax melts, it again behaves isotropically until it solidifies and the process is reversed. Depending on the physical properties of the wax, the approximation fits better or worse. Differential Scanning Calorimetry (DSC) was used to judge how well the approximation would work for the wax inks formulated for this research. The DSC measurement system records a signal proportional to the heat capacity of the material being measured.

Figure 4.3.5.1 shows a DSC curve characteristic of the PCL waxes used. Note that the enthalpy (heat) of fusion of the wax does cause the heat capacity to change. Because the model doesn't account for this change, it predicts temperatures to be slightly higher than actual as the wax ink passes through its T_m and T_g. Even so, the model works well as a first order approximation of the temperature profile of the wax/resin ink.

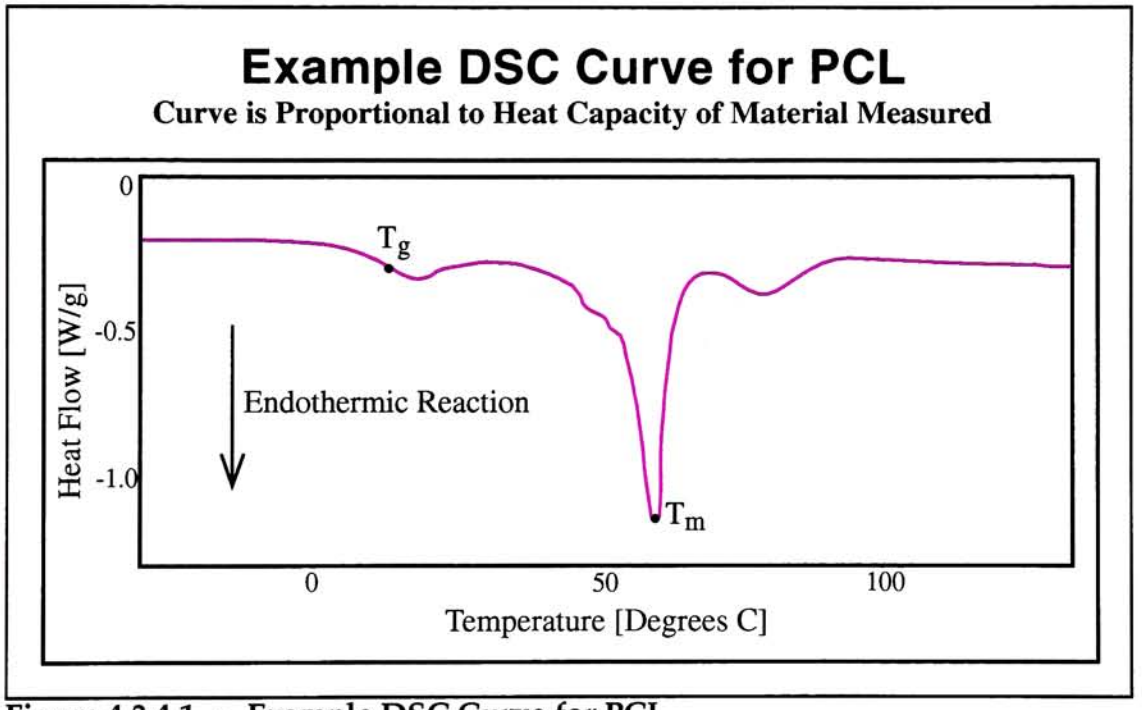

Figure 4.3.4.1 ~ Example DSC Curve for PCL.

A closed form solution to the differential equation for the conduction of heat provided an elegant approach to modeling the system. One shortcoming of this approach is the difficulty of interpreting multi-layer systems. In complex ribbon designs, it would be simpler and potentially more accurate to make use of finite element heat transfer modeling software such

as the PTC Mechanica Thermal Package. However, the point of the above model was not to absolutely predict the performance of the system, but instead was to gain a mathematical understanding of the physics of image formation. Hence, the classical approach was taken, suiting the purpose ideally.

4.4 Measuring Output Quality

Digital image analysis techniques permitted quantitative judgment of ribbon quality. As discussed in section 4.4, high quality of the ink coating was a prerequisite for acceptable image quality. Because of the fundamental importance of coating quality, a technique was designed for its analysis. Once acceptable coating quality was verified, ribbons were print tested and the resulting image analyzed. Image quality (IQ) was defined as a weighted combination of dot size, shape, and placement accuracy.

The algorithm for analyzing the coating quality (CQ) of an 8.5" x 11" section of ribbon was compiled through the aid of Noesis Visilog version 4.1, revision 3. The analysis of many experimental ribbons of varying quality aided development of the algorithm. Once each CQ analyzed ribbon was print tested, an attempt was made to correlate variations in coating thickness to the printed image. Only one significant correlation was made. In areas where there was little ink, there was no transfer. Images of the coatings were captured as above, and the grayvalues corresponding to areas of little ink were

probed. Based on these measurements, a threshold grayvalue was obtained, above which the probability of a printed dot was low.

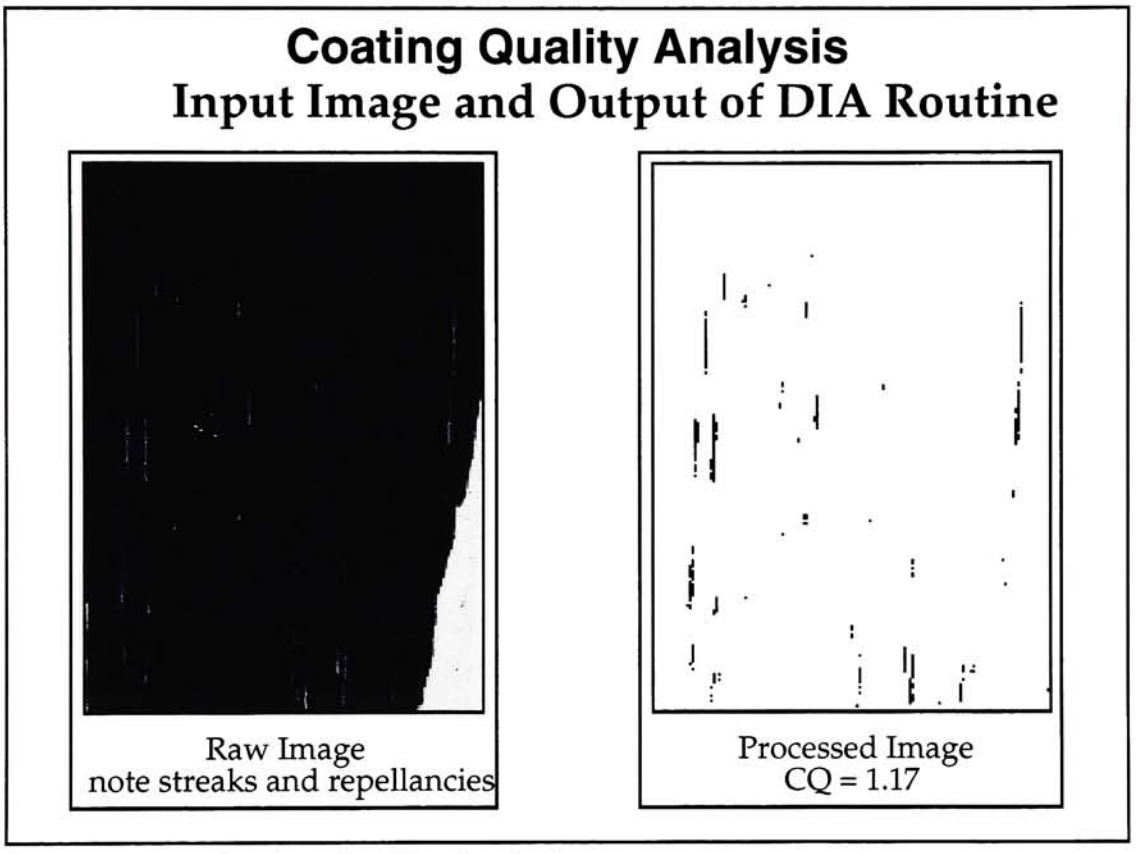

Figure 4.4.1 ~ Coating Quality Analysis.

The first step in the algorithm was to threshold the image to this critical grayvalue. Areas corresponding to low density at the edges of the image were then removed via the well known morphological *border kill* technique, for these low thickness border regions are common to all draw-down coatings. Working with this image of legitimate defect areas, a defect free image was created through the aid of further morphological filtering

techniques. A five iteration morphological erosion and subsequent reconstruction yielded the defect free comparison image. The area of the draw-down defect image was divided by the area of the comparison image and the result multiplied by 100. This number was defined as the *Percent Defects*, or CQ of the ribbon. Figure 4.4.1 shows an original image and the corresponding processed defect image.

In order to quantify IQ, a more-or-less conventional dot analysis routine was developed and compiled again with the aid of Noesis Visilog. IQ was defined as

$$IQ = 100\left[1-\left(0.5\frac{\overline{x}_{size}}{X_{size}}+0.3\frac{n}{N}+0.2\frac{\overline{x}_{shape}}{X_{shape}}\right)\right] \quad (1)$$

where:

$\overline{x}_{size}$ is the average dot size,

X_{size} is the expected dot size,

n is the number of dots imaged,

N is the expected number of dots,

$\overline{x}_{shape}$ is the average dot shape, and

X_{shape} is the expected dot shape.

Dot size refers to an equivalent circular diameter based on an area determination. Dot shape was calculated to be 1 minus the dot area divided by its normalized circumference. A perfect circle yielded a value of 0. As can be seen in (1), IQ varied between 0 and 100, with 0 being the optimum result. Of course, no actual result yielded the optimum, but there was a satisfactory spread between 20 and 95. Table 6.0.1 shows the range of values obtained for IQ during the designed experiment.

Initially, the greatest source of variation was found to be the printing process itself. Repeated measurements of prints yielded nearly identical results, but measurements of different prints made with the same exposure conditions produced considerably varying results. It was this variation that caused the experimenter to invest such a large amount of time optimizing the particulars of ribbon production and printing. Examples of refinements employed include longer mix times, centrifuging of inks, and pressure rolling the ribbon/receiver combination to remove entrained air prior to printing. Once these refinements had been implemented, the standard deviation of 10 IQ measurements from 10 "identical" prints fell to 1.7 units.

4.5 Optimizing the Photothermal Conversion Layer (PCL)

With the imaging process well understood, it became desirable to explore more thoroughly the design space of the system. Clearly there were many variables that could be included in the optimization process. The main effects of some of these variables were better understood than others. Exposure parameters provide a good example. From preliminary experiments, it was found that reciprocity held over a wide range of pulse amplitude and duration combinations. Additionally, exposure was constrained on the basis of laser cost. For these reasons, exposure parameters were not varied in the optimization process. Of course, the higher order interactions of exposure parameters with other variables was not well understood, so further experimentation in this area, although beyond the

scope of this research, would certainly be desirable. Other potential variables ruled out on the basis of good preliminary understanding and various constraints included layer thicknesses and pigment concentrations. Coating quality constrained these and others so that there was little freedom to move them. By far, the area of least understanding was PCL formulation. Interactions between the binder ingredients, although known to be of great importance, were not well understood.

A large number of screening experiments not only served to determine the waxes, resins, and pigments used, but also permitted the experimenter to gain a basic understanding of the relationships between the ingredients. At the conclusion of the preliminary experimentation, the quality of the LT2 system's output was acceptable, but was not optimal. Furthermore, the experimenter's knowledge of the complex relationships between the ingredients was not well understood. Additional experimentation was required. It was decided that, as mentioned in section 3.8, the following materials would be included in a PCL formulation optimization process:

- thermoplastic wax emulsion
- thermosetting resin dispersion
- thermoplastic resin latex
- thermoplastic resin emulsion.

Pigment and surfactant levels were held to constant percentages of the mix.

4.5.1 Mapping the PCL Design Space

Several of the screening experiments yielded image quality results suggesting significant interaction among the variables. In order to gain adequate understanding of the relationships among the four variables as well as their interactions, it was clear that an organized experimental design series would have to be run. Numerous four variable experimental design techniques exist. The challenge was to choose a design that would yield the most meaningful results from a reasonable number of experimental trials. Perhaps the greatest difficulty associated with experimental design is the selection of the most appropriate method for a given application.

Initial experiments led to the conclusion that none of the interactions could be ignored, therefore, some sort of full factorial was in order. Both two and three level designs were considered. While two well defined points may be connected to form a line, it is difficult to adequately describe a curve by connecting three points, no matter how well the three points are defined. That is, a good deal can concluded from the analysis of the relative position of two points from a bilevel experimental design. It is difficult to derive with certainty further information from the relative positions of three points. (Nelson et. al., 1994) Following this logic, a two level design was constructed, allowing a much greater area of the design space to be covered than with a three level design containing the same number of points.

The most useful statistical technique for this situation was found to be that employing response surface methodology, or RSM. RSM is often useful "...for analyzing problems where several independent variables influence a dependent variable or response, and the goal is to optimize this response" (Montgomery, 1976). Because the screening experiments showed that the response, image quality (IQ), could not be well-modeled by a linear function of the independent variables, a second order polynomial was employed, and proved to approximate the design surface sufficiently over the range of interest. The IQ polynomial was cast as

$$IQ = \hat{\beta}_0 + \sum_{i=1}^{k} \hat{\beta}_i x_i + \sum_{i=1}^{k} \hat{\beta}_{ii} x_i^2 + \sum_{i,i<j} \sum_{j} \hat{\beta}_{ij} x_i x_j \qquad (1)$$

where $\hat{\beta}_i$ are regression coefficients and x_i are independent input variables. Of course, while this model approximates the surface reasonably well over the design space, it most likely would not hold over the entire space of independent variables.

The choice of design type had much to do with the degree of fit achieved with the surface approximation. An *orthogonal, rotatable* design was chosen in order to realize the greatest degree of fit possible. "A design is said to be rotatable if the variance of the predicted response at some point is a function of only the distance of the point from the design center, and not a function of direction. This implies that the variance contours of [the response surface] are concentric circles. Furthermore, a design with this property will leave the variance of [the response surface] unchanged when the design is rotated about the center (0, 0,..., 0); hence the name rotatable

design" (Montgomery, 1976). Orthogonality of the design was of importance, for it led to clear response surface estimates with the lowest possible variance. "Orthogonality also [led] to joint confidence regions that [were] symmetric in all dimensions (for example, spheres) as opposed to asymmetric joint confidence regions (for example, ovoids). The symmetric joint confidence regions [were] smaller than their asymmetric counterparts. In addition, the lengths of individual confidence intervals are smaller for orthogonal designs than for nonorthogonal designs" (Manugistics, Inc., 1993).

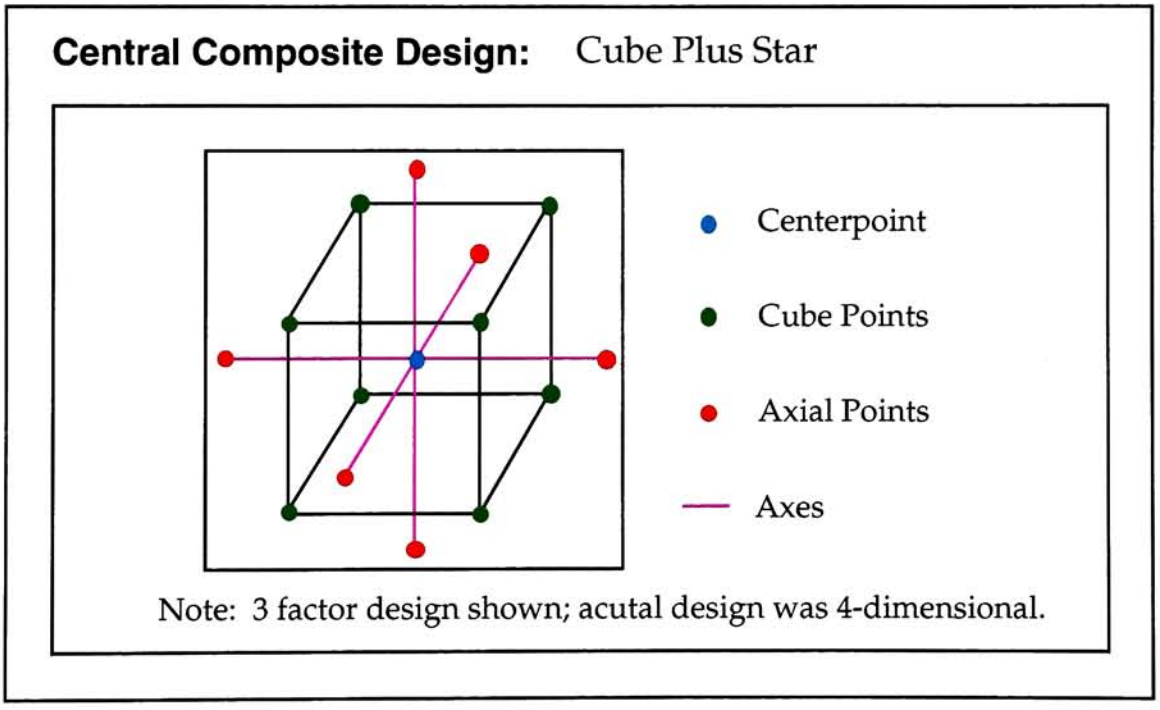

Figure 4.5.1.1 ~ Central Composite Design.

The chosen design was of *central composite* construction. That is, it consisted of a 2^4 factorial augmented by $2 \times 4 = 8$ axial points. The design was

made rotatable by carefully choosing the axial distances α, or the distances of the design points laying on axes. In coded notation, the box portion of the design included ±1 levels, while the axial points, forming the star portion, included ±2 levels. See Figure 4.5.1.1. To insure rotatability, the distances were chosen so that the variances of the predicted responses were "...constant on a hyperspherical surface centered at the design origin:

$$\alpha = (n_c)^{1/4} \tag{2}$$

where n_c is the number of points in the cube portion of the design, excluding centerpoints" (Manugistics, Inc., 1993). To make the design approximately orthogonal while maintaining rotatability, the number of centerpoint replications was set to satisfy

$$n_o = 4(n_c)^{1/2} + 4 - 2k \tag{3}$$

where n_o is the number of centerpoint replicates and k is the number of factors in the design. For the 2^4 design, the centerpoint was replicated 12 times, leading to a robust estimate of variation caused by experimental error. Again, because the design was rotatable, the estimate of variation at the centerpoint was related to the variation at any of the other points by their distance from the center.

The parameters relevant to the design were fed into the Manugistics Statgraphics, version 7.0 RSM design and analysis tools, which generated a fully randomized design worksheet to be followed. Once all of the experimental ribbons had been made, IQ was measured for each ribbon and

the results were entered back into Statgraphics. The raw input and response data can be found in the Appendices.

4.5.2 Analyzing and Modeling the PCL Design Space

An analysis of variance (ANOVA) was completed with the aid of Statgraphics. In so doing, several statistics, including diagnostics, were computed by the software. The ANOVA information, presented in Table 4.5.2.1, shows the significance of each of the modeled terms. From the data, the estimated effects were also calculated. Table 4.5.2.2 presents the effects, estimates of error for the effects, and the standardized effects. The standardized effects were determined by dividing the terms by their respective error estimates. While these conventional tables are useful, the graph of Figure 4.5.2.1 presents the results in a much friendlier manner.

ANOVA Table for Ribbon Formulation Designed Experiment

Term	Sum of Squares	DF	Mean Square	F-Ratio	P-value
A: Jonwax 120	5894.3686	1	5894.3686	171.29	0.0000
B: PVP K90	0171.4279	1	0171.4279	004.98	0.0366
C: SCX 2560	2376.6812	1	2376.6812	069.07	0.0000
D: Joncryl 624	0528.5936	1	0528.5936	015.36	0.0008
AB	0123.2100	1	0123.2100	003.58	0.0723
AC	0001.0043	1	0001.0043	000.03	0.8678
AD	0132.3060	1	0132.3060	003.84	0.0633
BC	0042.1085	1	0042.1085	001.22	0.2812
BD	0255.6086	1	0255.6086	007.43	0.0127
CD	0256.1284	1	0256.1284	007.44	0.0126
AA	1786.6047	1	1786.6047	051.92	0.0000
BB	8023.4420	1	8023.4420	233.16	0.0000
CC	4804.8944	1	4804.8944	139.63	0.0000
DD	4352.8455	1	4352.8455	126.49	0.0000
Total error	0722.6418	21	0034.4115		
Total (corr.)	29417.6822	35			

R-squared 0.975
R-squared (adj. for D.F.) 0.959

Table 4.5.2.1 ~ ANOVA Table for Formulation Designed Experiment.

In Figure 4.5.2.1, as above, the standardized effect for each modeled term was calculated by dividing the effect of each term by its standard error. However, in order to plot the results in a "Pareto" type of format, the absolute value of each standardized effect was plotted. The critical level represents the t-value for an α of 0.05. All of the effects exceeding this level are significant. Using this rule, the only insignificant effect is the A-C interaction. Note the relative significance of the second order terms of the model, showing that the

response surface is not linear. If these terms were insignificant, a linear model would have sufficed.

Estimated Effects from ANOVA

Term	Estimated Effect		Standard Error	Standardized Effect
Average	19.9978	+/-	1.69342	11.81
A: Jonwax 120	-31.3432	+/-	2.39484	-13.09
B: PVP K90	5.34522	+/-	2.39484	02.23
C: SCX 2560	19.8929	+/-	2.39368	08.31
D: Joncryl 624	9.38097	+/-	2.39353	03.92
AB	-5.55	+/-	2.93307	-01.89
AC	-0.501074	+/-	2.93306	-00.17
AD	-5.75121	+/-	2.93306	-01.96
BC	-3.24455	+/-	2.93306	-01.11
BD	-7.99387	+/-	2.93306	-02.73
CD	-8.00198	+/-	2.93306	-02.73
AA	14.9441	+/-	2.07399	07.21
BB	31.6691	+/-	2.07399	15.27
CC	24.448	+/-	2.06897	11.82
DD	23.2626	+/-	2.06834	11.25

Standard error estimated from total error with 21 d.f.
t = 2.08012
$\alpha/2$ = 0.025

Table 4.5.2.2 ~ Estimated Effects from ANOVA.

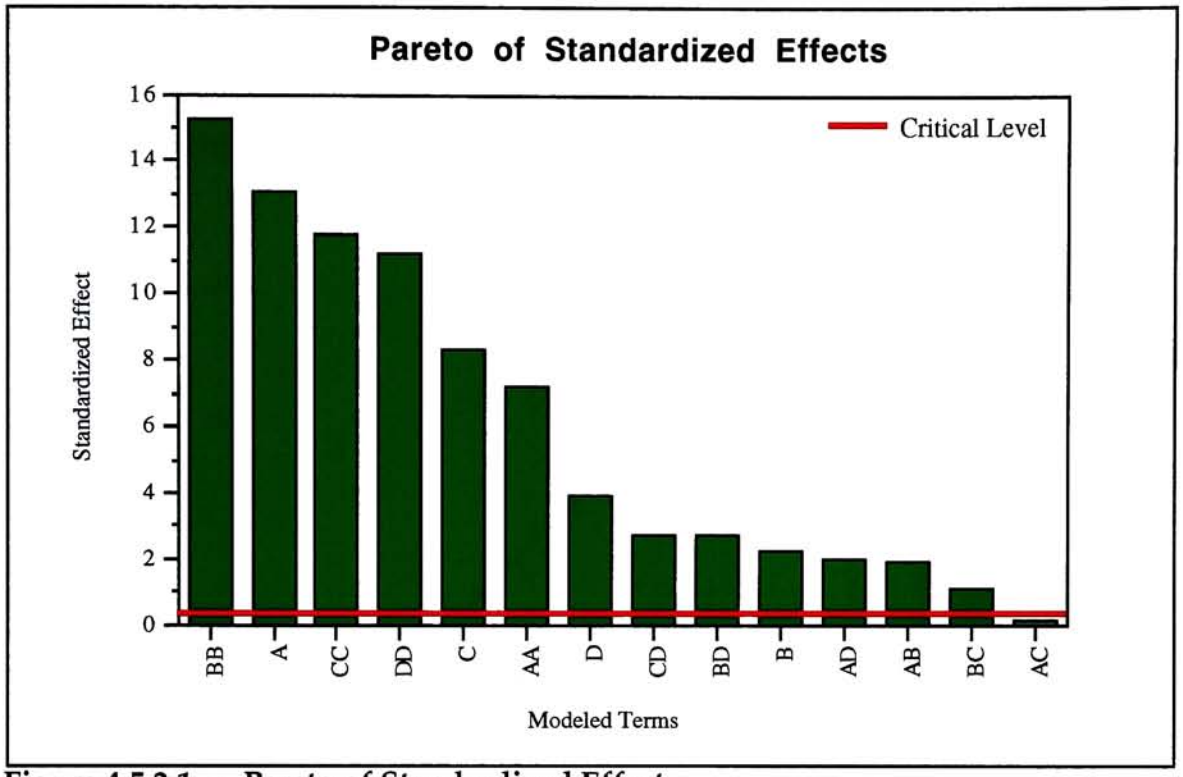

Figure 4.5.2.1 ~ Pareto of Standardized Effects.

One way to diagnose a design model is to plot observed responses versus model predicted responses. Such data was generated using the Statgraphics RSM analysis tools. Figure 4.5.2.2 presents a plot of the experimental data. Note that the variance of the data is uniformly distributed about the slope = 1 line. If the variation was uniform but wide about the slope = 1 line, the precision of the measurement system would have been suspect. Similarly, if the spread of data was wider at one portion of the plot than at another, local precision of the measurement system would be in question. Large random deviations from the line would have indicated excessive variance in the measurement system.

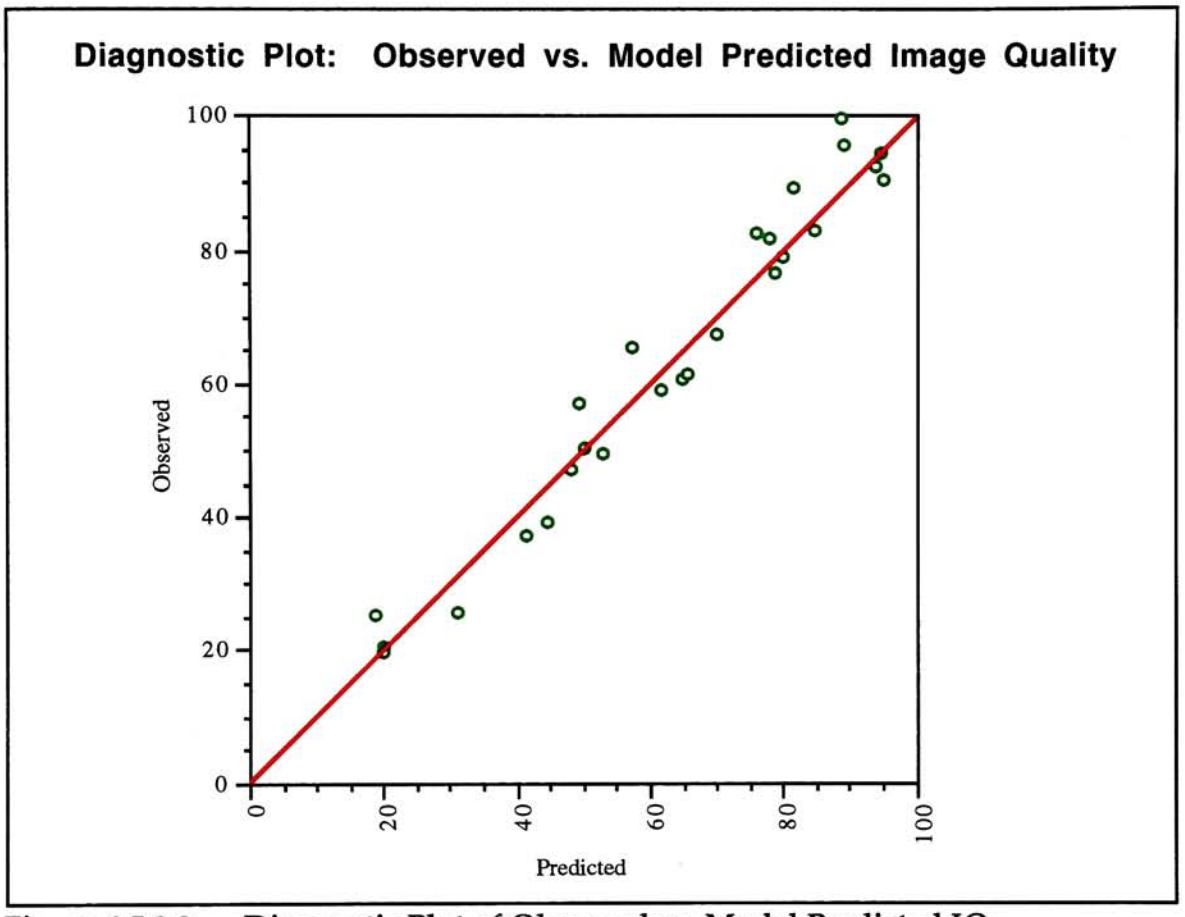

Figure 4.5.2.2 ~ Diagnostic Plot of Observed vs. Model Predicted IQ.

Another method by which to diagnose a design model is to plot the residuals versus the run number, looking for trends. Residuals were defined as

$$e_j = y_j - \hat{y}_j$$

where y_j represents an IQ observation (4)

and $\hat{y}_j$ a corresponding fitted value from the model.

Such a graph was created and is presented in Figure 4.5.2.3. Looking at the residuals in this manner, it can be seen that there was no trend in variance

over time. It is interesting to note that the highest residuals correspond to those formulations at the star points. Although the second order polynomial regression model certainly is adequate, the fit is less than optimal at these points. If this case were significantly worse, the design would have been augmented to included third order terms.

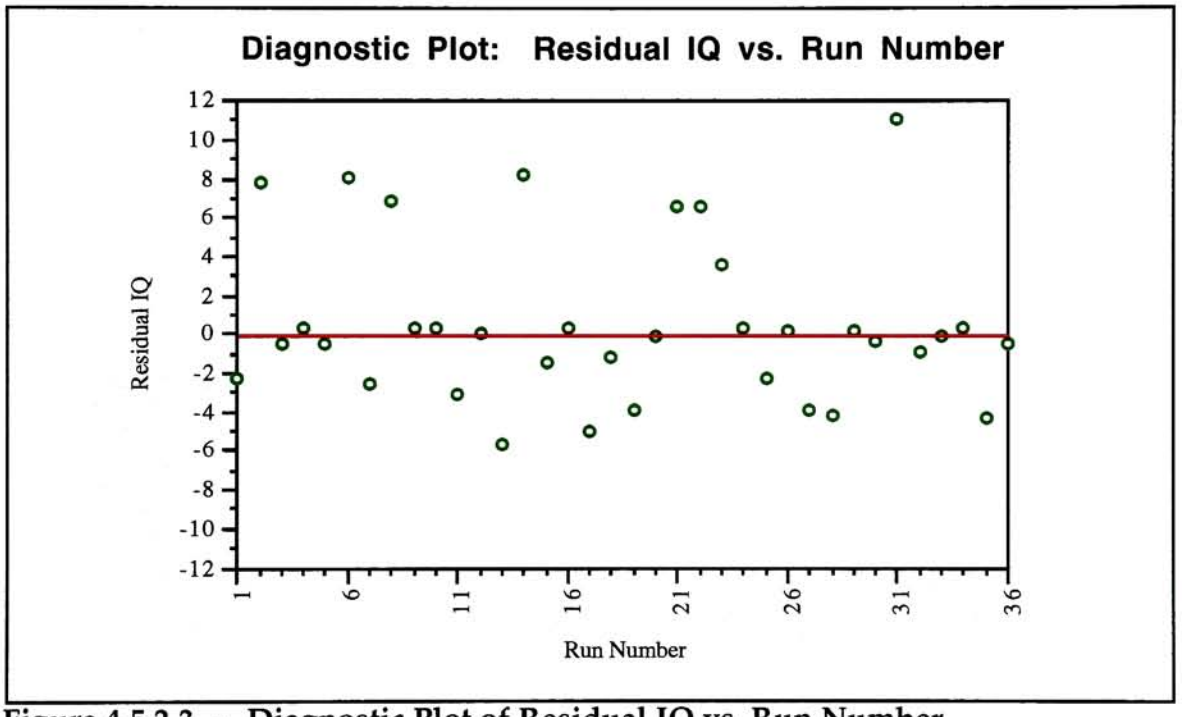

Figure 4.5.2.3 ~ Diagnostic Plot of Residual IQ vs. Run Number.

4.5.3 Constrained Optimization of the PCL Design Space

Once convinced that the model adequately described the PCL design space, Statgraphics was used to estimate the coefficients for a second order regression model based on the data. Table 4.5.3.1 presents the coefficients. Plugging the coefficients into the IQ polynomial of section 4.5 equation 1 led

to an approximation of the response surface within the constraints of the central composite design space. The axial star points, representing regions where each variable was at its highest and lowest level, constrained the space. The IQ polynomial, or *objective function*, was used to generate plots aiding visualization of the response surface. More importantly, however, it was used to complete RSM analysis of the surface and optimization of the PCL formulation. The objective function was optimized for the single objective, image quality, using a C program employing Nelder and Mead's *Downhill Simplex Method* of optimization and verified with a minimum locating function within Wolfram Research's Mathematica, version 2.2.

Regression Coefficients		
k = 293.95	AB = -0.0569231	CD = -1.5298
A = -11.5617	AC = -0.0224747	AA = 0.176853
B = -4.82805	AD = -0.290099	BB = 0.281503
C = -15.4228	BC = -0.126124	CC = 4.1561
D = -7.90805	BD = -0.349459	DD = 5.00136

Table 4.5.3.1 ~ Regression Coefficients.

An analogy to a minimum-locating function is the dropping of a marble onto the response surface. The marble would seek the lowest point of the constrained area driven by gravity. Depending on the surface, the final resting place of the marble may represent either a global or local minimum. If the function were *convex* within the constrained area, the marble would come to rest in a global minimum. A function is said to be *convex* if linear interpolation between any two function values never underestimates the real

value of the function at the interpolated point. Any local minimum of a convex function attained over a convex set is a global minimum. The plots given in Figure 4.5.3.1 were used to visualize the response surface (while three-dimensional graphs are shown, note that the actual response surface was four-dimensional). Although this design yielded a bowl-shaped response surface, such is not always the case. In fact, generally speaking, most optimization problems in engineering involve either non-convex functions or functions whose convexivity cannot be easily be proven. Other response surface topographies include, for example, saddle-points, rising ridges, and domes. It is not a coincidence that the design yielded such a bowl-shaped surface. Careful screening of the input variables helped insure that a minimum would exist within the design space.

Given that the fitted surface adequately approximated the actual response surface within the constrained area, a necessity which was verified by the analysis of the statistics presented in section 4.5.2, then analysis of the fitted surface was approximately equivalent to analysis of the actual system (Montgomery, 1976). Following this logic, in order to determine the optimum formulation, the path of steepest descent could be followed to the lowest local minimum, described by a set x_1, x_2, x_3, and x_4 such that their partial derivatives

$$\frac{\partial IQ}{\partial x_1} = \frac{\partial IQ}{\partial x_2} = \frac{\partial IQ}{\partial x_3} = \frac{\partial IQ}{\partial x_4} = 0. \qquad (5)$$

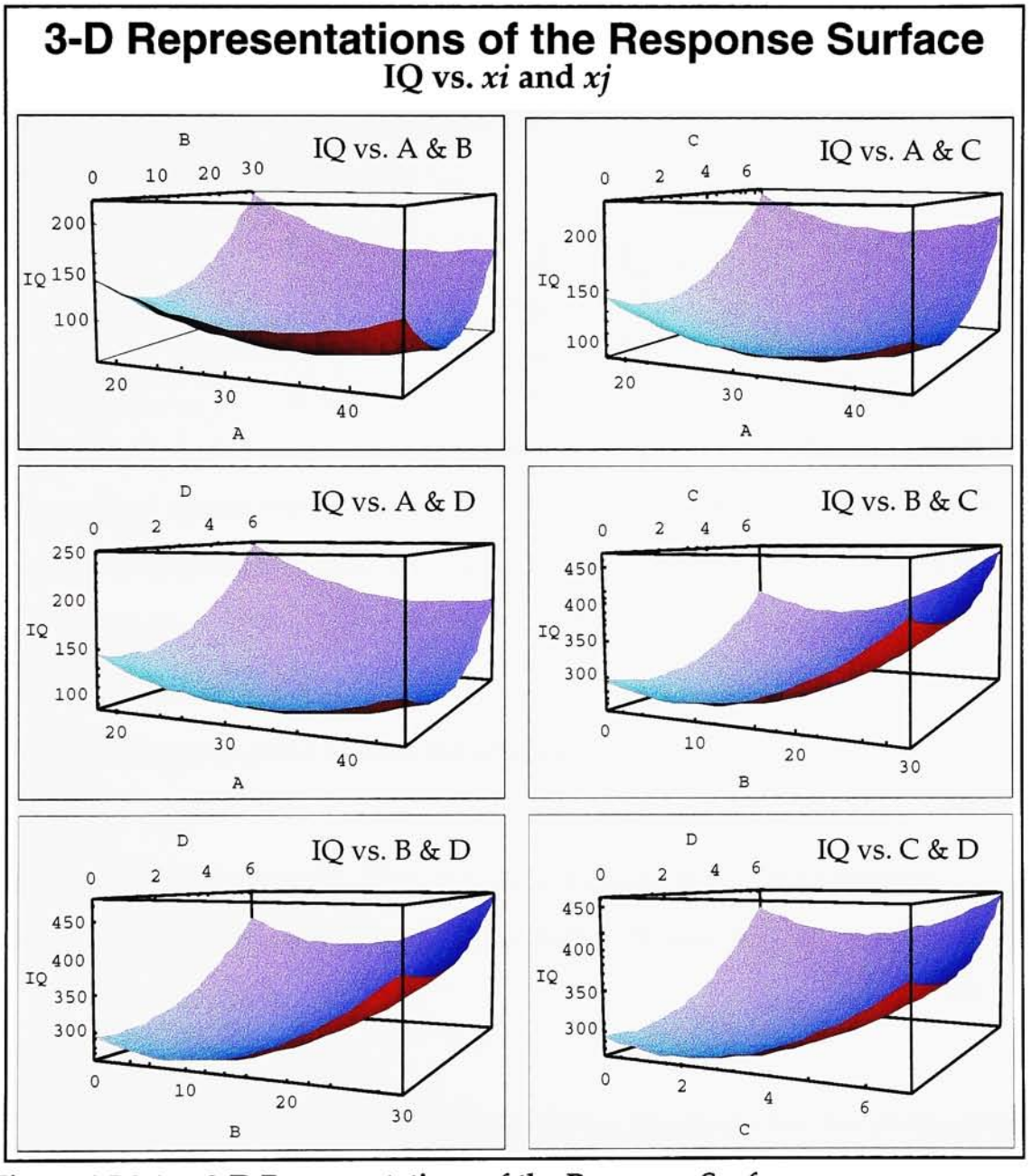

Figure 4.5.3.1 ~ 3-D Representations of the Response Surface.

The point at which these criteria were met is commonly referred to as the *stationary point*. To arrive at a general solution for this point, (5) must be recast in matrix notation:

$$IQ = \hat{\beta}_0 + \mathbf{x}'\mathbf{b} + \mathbf{x}'\mathbf{B}\mathbf{x}$$

where

$$\mathbf{x} = \begin{bmatrix} x_1 \\ x_2 \\ x_3 \\ x_4 \end{bmatrix} \quad , \quad \mathbf{b} = \begin{bmatrix} \hat{\beta}_1 \\ \hat{\beta}_2 \\ \hat{\beta}_3 \\ \hat{\beta}_4 \end{bmatrix} \quad \text{, and} \quad \mathbf{B} = \begin{bmatrix} \hat{\beta}_{11} & \hat{\beta}_{12}/2 & \hat{\beta}_{13}/2 & \hat{\beta}_{14}/2 \\ \hat{\beta}_{21}/2 & \hat{\beta}_{22} & \hat{\beta}_{23}/2 & \hat{\beta}_{24}/2 \\ \hat{\beta}_{31}/2 & \hat{\beta}_{32}/2 & \hat{\beta}_{33} & \hat{\beta}_{34}/2 \\ \hat{\beta}_{41}/2 & \hat{\beta}_{42}/2 & \hat{\beta}_{43}/2 & \hat{\beta}_{44} \end{bmatrix}. \quad (6)$$

In 4.5.3, **b** represents a vector of the first order regression coefficients and **B** is a symmetrical matrix whose diagonals are the pure quadratic coefficients and whose off-diagonal elements are one-half the mixed quadratic coefficients. The partial derivative of IQ with respect to the vector **x** set to zero is

$$\frac{\partial IQ}{\partial \mathbf{x}} = \mathbf{b} + 2\mathbf{B}\mathbf{x} = 0 \quad (7)$$

and the stationary point is then the solution to (7):

$$\mathbf{x}_0 = -\frac{1}{2}\mathbf{B}^{-1}\mathbf{b} \quad . \quad (8)$$

As shown by Montgomery, 1976, it is now possible to find the predicted response at the stationary point by substituting (8) into (6):

$$IQ_0 = \hat{\beta}_0 + \frac{1}{2}\mathbf{x}_0'\mathbf{b} \quad . \quad (9)$$

In practice, there are many well known algorithms for the computation of the stationary point of an objective function. (Press, et. al., 1992) In determining the optimization algorithm best suited to the task, a fundamental choice had to be made between "...methods that need only

evaluations of the functions to be minimized and methods that also require evaluations of the derivative of [the objective] function [as above]. In the multidimensional case, this derivative is the gradient, a vector quantity. Algorithms using the derivative are somewhat more powerful than those using only the function, but not always enough so as to compensate for the additional calculations of derivatives" (Press, et. al., 1992). The best algorithm for any particular optimization problem depends on the nature of the function, the computational resources available, and the amount of time allotted for programming and computation. In this case, the second order polynomial objective function was relatively simple (see Figure 4.5.3.2), the amount of time spent programming was desired to be small, and the amount of time taken by the available computer for computation was not important. For these reasons, a direct search method was employed -- a method not requiring the computation of gradients. In particular, the *Downhill Simplex Method* of Nelder and Mead (1965) was chosen as the optimization algorithm.

The Downhill Simplex Method (DSM) requires only function evaluations, not derivatives. The code is therefore concise, but less efficient in the number of function evaluations required as compared to a method such as Powell's (Press, et. al., 1992), which relies upon the calculation of derivatives. In fact, the DSM code written was about 100 lines with a storage requirement on the order of the number of dimensions squared ($4^2 = 16$). DSM is elegant in its compactness and its method of "...crawling downhill in a straightforward fashion that makes almost no assumptions about the

[objective] function" (Press, et. al., 1992). While DSM "...can be extremely slow, it can also, in some cases, be extremely robust.... This method is most useful when the minimization calculation is only an incidental part of [the] overall problem.... [DSM] may frequently be the *best* method to use if the figure of merit is 'get something working quickly' for a problem whose computational burden is small" (Press, et. al., 1992). DSM was ideally suited to the task of optimizing the second order polynomial objective function describing the PCL design space.

As illustrated in Figure 4.5.3.2, a *simplex* is a geometrical figure consisting of $N + 1$ points in N dimensional hyperspace. All of the simplex points, or vertices, are interconnected by line segments. When N is greater than 2, the polygonal faces are included in the simplex. For $N = 3$, as in Figure 4.5.3.1, it is a tetrahedron, although not necessarily a regular tetrahedron. "In general we are only interested in simplexes that are nondegenerate, i.e., that enclose a finite inner N-dimensional volume. If any point of a nondegenerate simplex is taken as the origin, then the N other points define vector directions that span the N-dimensional vector space" (Press, et. al., 1992).

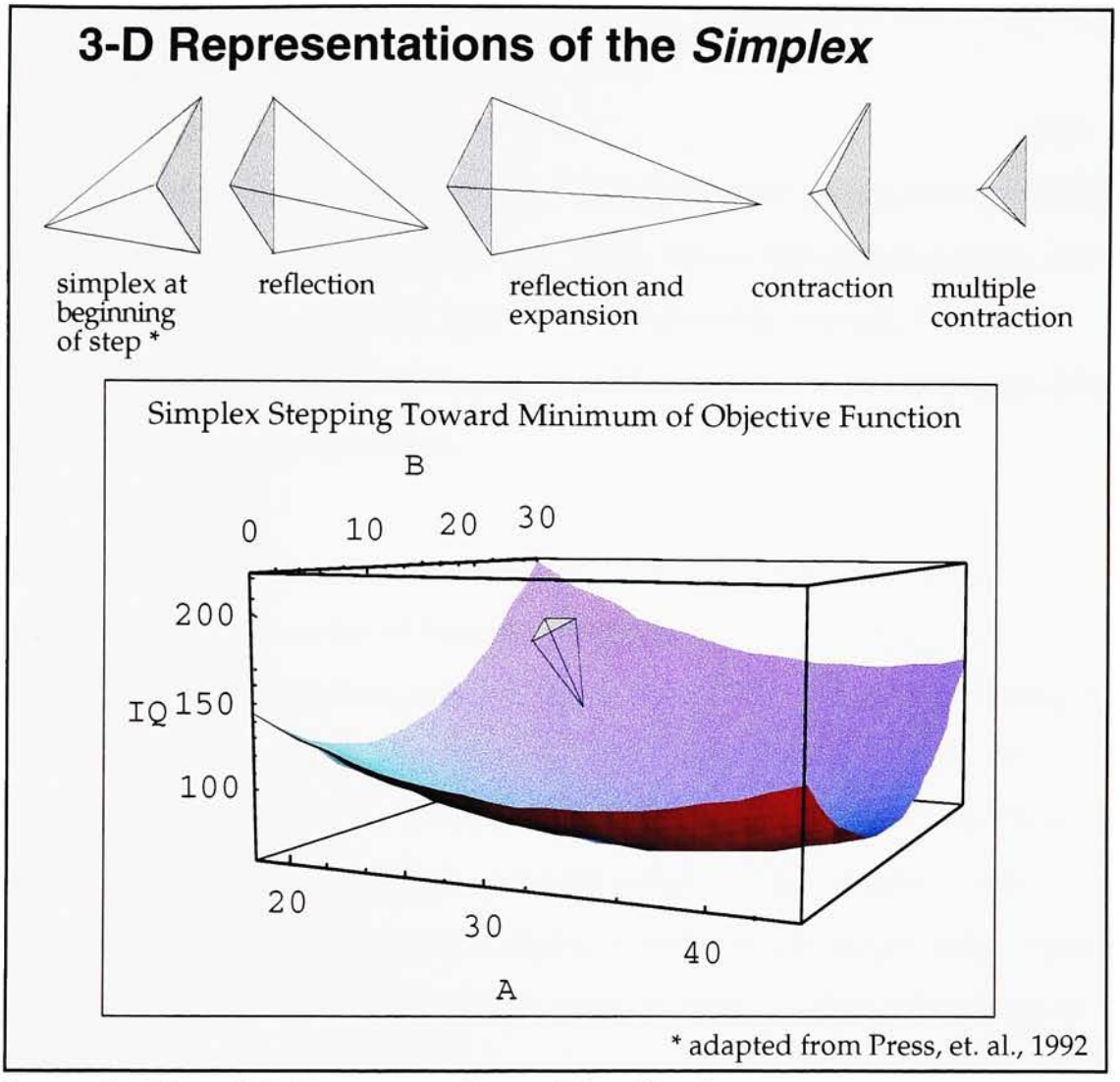

Figure 4.5.3.2 ~ 3-D Representations of the *Simplex*.

In multidimensional optimization, there is no way to bracket a minimum so that the success of a subsequent isolation is guaranteed (Press, et. al., 1992). Therefore, the algorithm must be presented with an N+1-dimensional vector of independent variables as a starting guess. The points

of this simplex may be described by $\mathbf{P}_0$, any one of the points, with the remaining N values denoted by

$$\mathbf{P}_i = \mathbf{P}_0 + \lambda \mathbf{e}_i \tag{10}$$

where $\mathbf{e}_i$'s are N unit vectors, and where λ is a constant guess of the problem's characteristic length scale (Press, et. al., 1992). Given this initial simplex, the algorithm employed then attempts to move downhill through the "unimaginable complexity" (Press, et. al., 1992) of N-dimensional topography until it encounters a minimum.

In converging on the minimum, DSM takes a series of steps, most moving the simplex point of highest value through the centroid of the simplex, or center of gravity, and outside opposite face in hopes of landing on a lower point. Such steps are commonly known as "reflections" and are illustrated in Figure 4.5.3.2. In order to avoid degeneracy, these reflections must be constructed to maintain constant volume of the simplex. When possible, the method expands the simplex in order to take larger steps. Upon reaching a "valley floor," the method contracts itself, in effect attempting to "...ooze down the valley. If there is a situation where the simplex is trying to 'pass through the eye of a needle,' it contracts itself in all directions, pulling itself in around its lowest (best) point" (Press, et. al., 1992).

Although not a concern with this particular objective function, it is worth mentioning that the convergence of DSM can be hampered when the simplex oversteps a constraint. In this case, the simplex must be contracted to

remain within the bounds of the problem, slowing convergence. Penalty function methods such as SWIFT (Sequential Weight Increasing Factor Technique) avoid this deficiency in the flexible polyhedron search by transforming a constrained problem into a series of unconstrained problems (Sheela, et. al., 1974). In minimizing the objective function, each vertex is forced by the penalty function to satisfy the constraint to some degree. By varying the penalty weights based on previous iterations, penalty function methods constantly compromise between minimization and constraint satisfaction. Because the simplex is not permitted to overstep the constraints, convergence is reached significantly earlier for complex problems. The objective function in this particular case was simply not of high enough complexity to warrant the increased coding of a penalty function method such as SWIFT.

Two methods of terminating the optimization algorithm were investigated. The first method required the total vector distance moved per step to be less than a hard coded tolerance. When contraction of the simplex led to a total movement vector distance beneath this tolerance, the algorithm terminated, and the optimal (minimum) point of the objective function was reported. The second method required that the decrease in the function value from one step to the next be less than a tolerance value for algorithm termination. While the second method allows a tolerance value on the order of machine precision, the first requires a tolerance on the order of the square

root of the machine precision in order to avoid error induced by roundoff . For this reason, the second termination criteria was employed.

It is possible for DSM to be fooled by a "...single anomalous step that, for one reason or another, failed to get anywhere" (Press, et. al., 1992). To assure the research was not thrown off course by an erroneous optimal point, the algorithm was restarted from the reported minimum as well as from several other points within the design space. In every case, the algorithm converged to the same point on the design space in less than 25 steps.

As a further check on the validity of the result, the objective function was coded into Mathematica. The "FindMinimum" function was then used to determine the optimal point. For all practical intents and purposes, "FindMinimum" yielded the same result as the DSM code. It is interesting to point out that "FindMinimum" uses Brent's Conjugate Gradient Method, which is a very different algorithm from the Downhill Simplex Method described above. Brent's Conjugate Gradient Method, as the name implies, makes use of the first partial derivative vectors of the N-dimensional objective function points. While DSM is efficient in the amount of code required, Brent's Conjugate Gradient Method is efficient in the number of iterations required to determine the minimum. A complete description of Brent's Conjugate Gradient Method can be found in **Numerical Recipes in C** (Press, et. al., 1992). Although Brent's Conjugate Gradient Method did in fact require fewer iterations to reach the optimum point, the topography of the

objective function was not severe enough to reveal much difference in computing time between the two algorithms. Each algorithm required only a few seconds to converge, running on an 80 MHz PowerPC 601 RISC microprocessor. With the minimum point of the PCL design space definitely determined, the corresponding formulation was used to create optimized ribbons.

4.6 Imaging and Discussing the Optimized System

In producing the optimized ribbon, all of the refinements to the process learned during development were implemented. These refinements included simple things, such as optimal mix times and impeller shape and speed, order of addition rules, and 185 °F / 1.25 min. drying conditions. They also included centrifuging of the PCL ink, the use of a special, microporous synthetic receiver sheet, and pressure rolling of the ribbon / receiver / platen combination prior to printing. Of these parameters, the two with the largest impact were PCL ink centrifuging and receiver sheet material. These refinements led to images with the least IQ variance.

4.6.1 PCL Ink Centrifuging

The importance of adequate pigment dispersion cannot be overstressed. In the case where there were large pigment aggregates remaining in the PCL ink, coatings having poor uniformity resulted. The aggregates, if not broken up or removed, produced local areas having pigment to binder ratios much above the desired condition of 0.18, and, perhaps more

importantly, produced non-uniformities in coating thickness and heat capacity. These local variations, on the order of a couple to several micrometers in width, added to the variance of the system in such a way as to adversely modify dot size, shape, and placement accuracy -- all of the factors contributing to IQ. Figure 4.6.1.1 presents two images, both of which were made with the optimal ribbon using a pulse width of 100 μsec and a total beam power of 20 mWatts. The first image was made with a ribbon having a non-centrifuged PCL; the second with a ribbon having a centrifuged PCL. Note the differences in variance. Within some boundaries, where there is locally high coating thickness, no dot will transfer; where there is locally low coating thickness, a large dot will transfer.

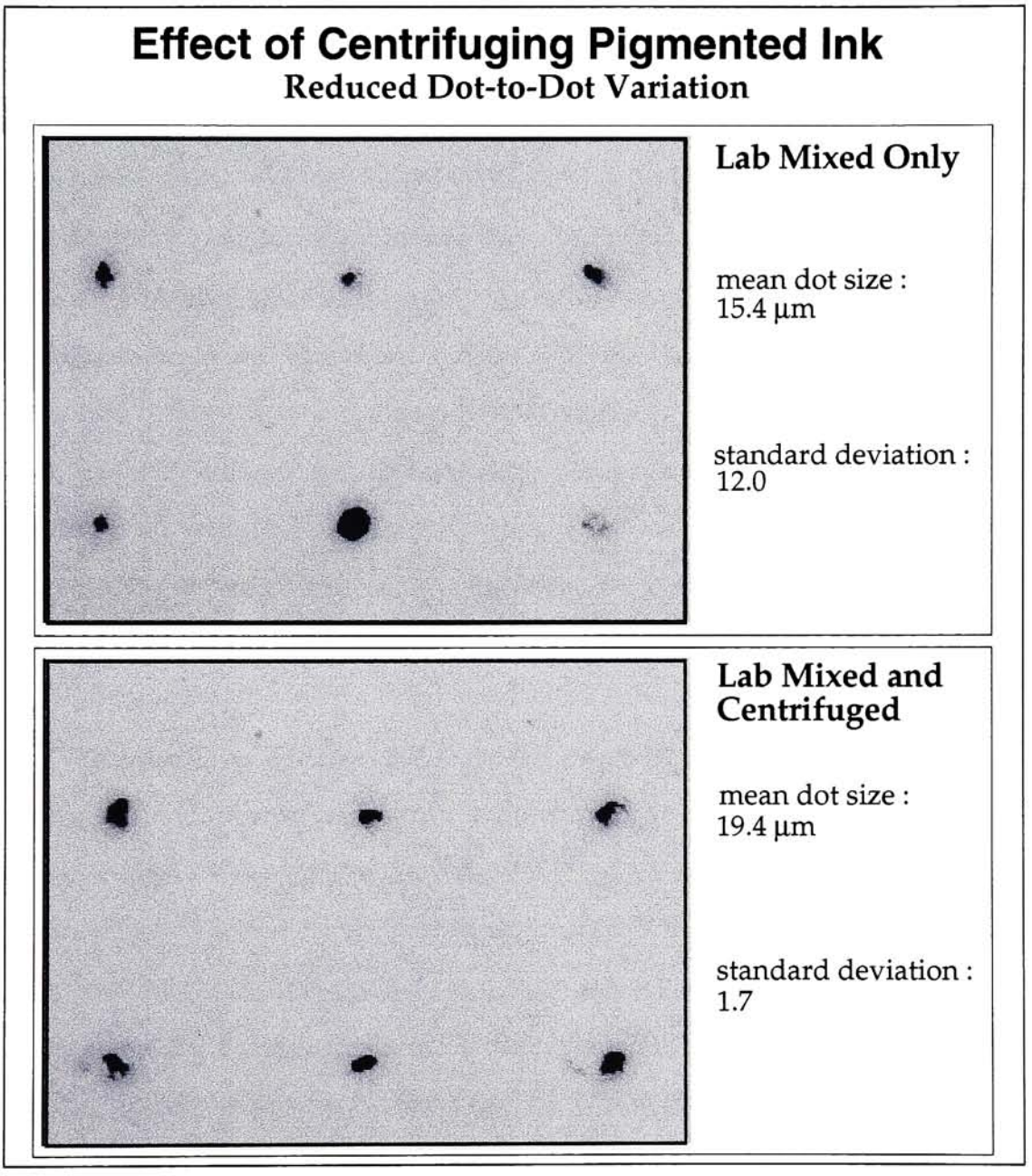

Figure 4.6.1.1 ~ Effect of Centrifuging Pigmented Ink.

4.6.2 Microporous Receiver Sheet

Printing the optimal ribbon on different receiver sheets confirmed that receiver non-uniformity leads to excessive variance in IQ. In the case when the cohesive force between the PCL ink molecules is higher than the adhesive force of the PCL molecules to the receiver, no dot will transfer. The receiver sheet was specifically chosen so that the adhesive force of the molten ink to its surface was great. The receiver was "wettable" by the molten ink primarily due to the construction and topology of its surface. While on one scale the sheet was very smooth and uniform, on a micrometer scale it was known to be filled with pores. It was the smoothness that helped insure intimate contact between the ribbon and the receiver, and the micro-porosity of the surface that gave the sheet the ability to mechanically *grab* the molten ink.

Compared to a conventional coated paper sheet, the uniformity of the surface and bulk isotropicity of the chosen microporous receiver was much greater, as can be seen in the Scanning Electron Microscope (SEM) images of Figure 4.6.2.1. Each of the three images represents a close-up view of a single pixel, printed with a 300 dpi conventional thermal transfer writing engine. In conventional DT2 imaging, the uniformity, or smoothness, of the sheet is of concern, but not nearly so much as in LT2, where nip pressure is minimal and desired resolution is three times higher. Even smooth, coated cellulosic sheets may have surface deviations on the order of an LT2 pixel. In the first image of Figure 2.4.6.1, the highly irregular surface topography and composition of Hammermill Laser Print has limited the transfer of molten

wax ink to areas where the donor ribbon and receiver were in intimate contact. The center image of Figure 4.6.2.1 shows a dot printed with the same engine and donor ribbon as the image on the left, but with a specially coated receiver sheet (Tektronix Phaser 200 Coated Paper). Note the surface uniformity of the coated paper allowing good contact between ribbon and receiver. Of course, this sheet not only has high smoothness, but also chemistry of the coating tuned to accept the wax ink.

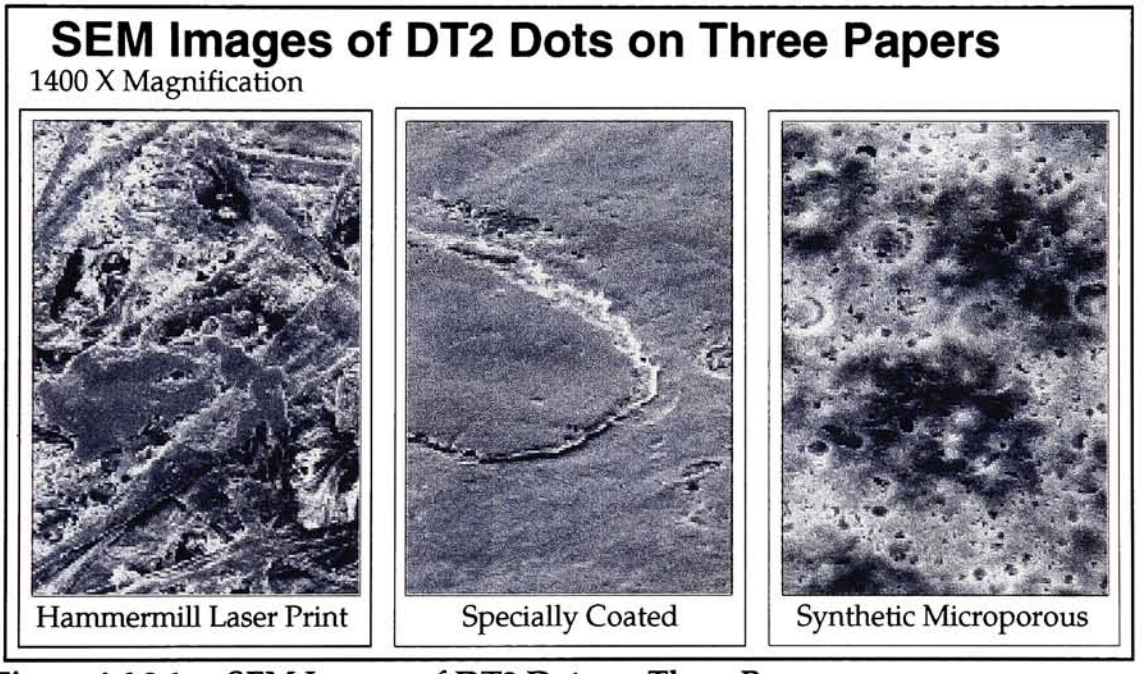

Figure 4.6.2.1 ~ SEM Images of DT2 Dots on Three Papers.

The image on the right of Figure 4.6.2.1 is perhaps the most interesting. While the macroscopic surface of the sheet is smooth, the microscopic surface is filled with small pores on the order of 10 μm in diameter. The capillary suction associated with these pores greatly increases the affinity of the wax ink

to the receiver. Additionally, the air entrained in the coating greatly increases the receiver's ability to impede the conduction of heat away from the spot being imaged by the laser (or conventional printhead). The combination of these attributes, namely those associated with the high surface regularity and thermally insulative nature of the microporous coating, led to a LT2 receiver sheet far superior to any others evaluated.

4.6.3 Variable Dot Size LT2 Printing

The ribbon was optimized for total beam power of 20 mWatts and a pulse width of 205 μsec. As the model predicted, it was possible to produce variable dot sizes by varying temporal pulse width. Because it is often more cost effective to modulate pulse width (duty cycle) of such a system rather than pulse height (applied power), this approach was used almost exclusively in variable dot size experimentation. Figure 4.6.3.1 provides images of dots made at various temporal pulse widths. The pulse widths of images one through six were 75 μsec, 100 μsec, 125 μsec, 150 μsec, 175 μsec, 205 μsec, respectively. These images compare favorably with the model predictions illustrated in Figure 4.3.2.7. There is no doubt that, given these results, the system is capable of variable dot size printing. The number of gray levels desired must be factored into the desired cost of the engine, weighing in issues such as power source stability and allowed component variations such as coating quality and air entrained in the nip.

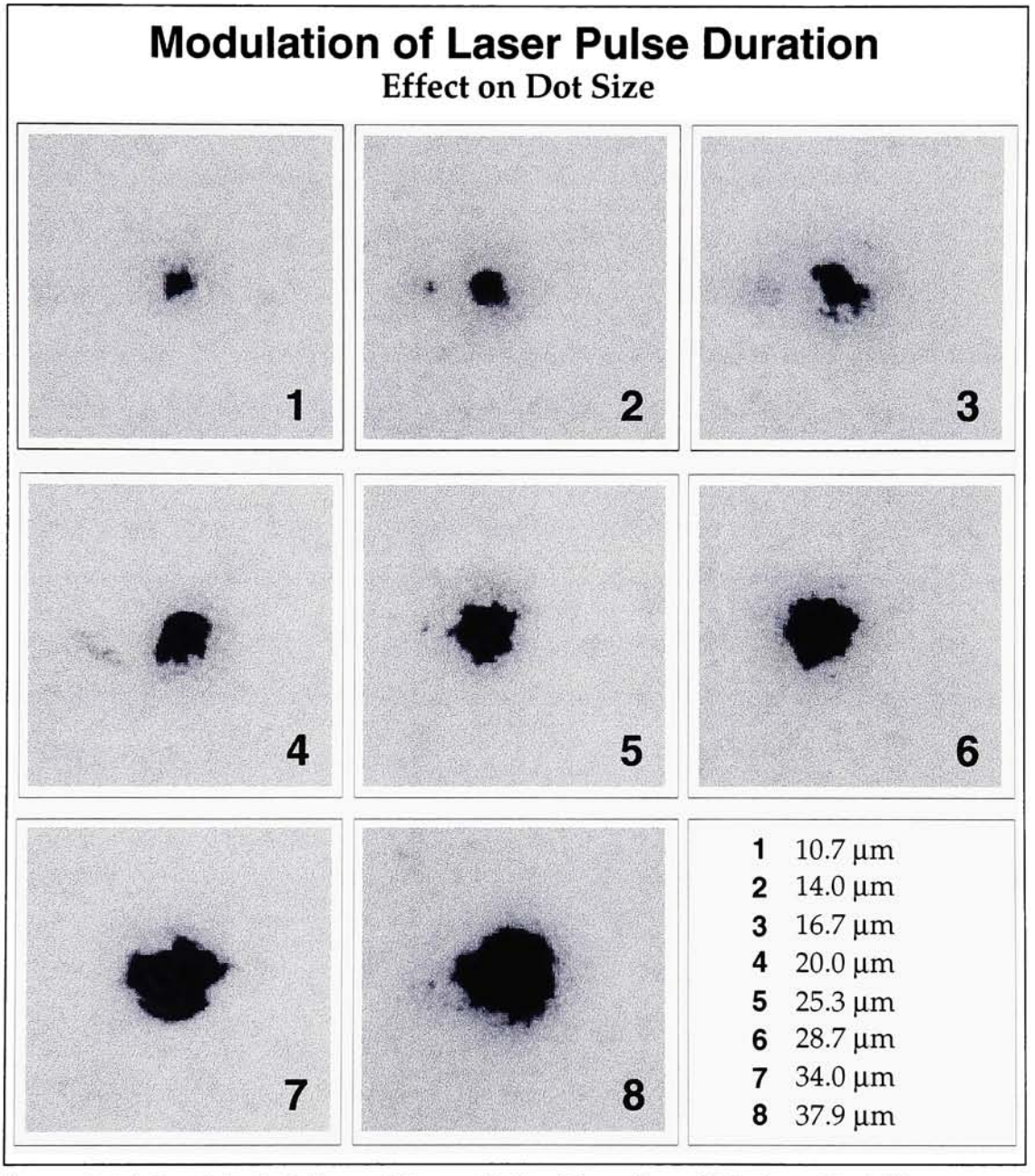

Figure 4.6.3.1 ~ Modulation of Laser Pulse Duration: Effect on Dot Size.

4.6.4 Vector Format LT2 Printing

Although the system was optimized primarily for bitmap type printing, vector (single pixel line) quality was also periodically checked. Figure 4.6.4.1 shows two printed single width lines, both of which were made in the raster scan direction. The first of the two was made with the optimized system. The second of the two was made with a ribbon having low amounts of the primary wax. Note that in the areas of highest fluence, there is little transfer, and that the high cohesive force of the ink caused excess ink transfer upon separation of the receiver and donor sheet. This example shows the range of performance mapped by the design space. While there was indeed a large amount of control over IQ afforded by the writing engine, it was the ribbon that required the most effort to optimize. Figure 4.6.4.1 demonstrates that producing a thermal transfer print is not a simple matter of melting wax in an image-wise manner.

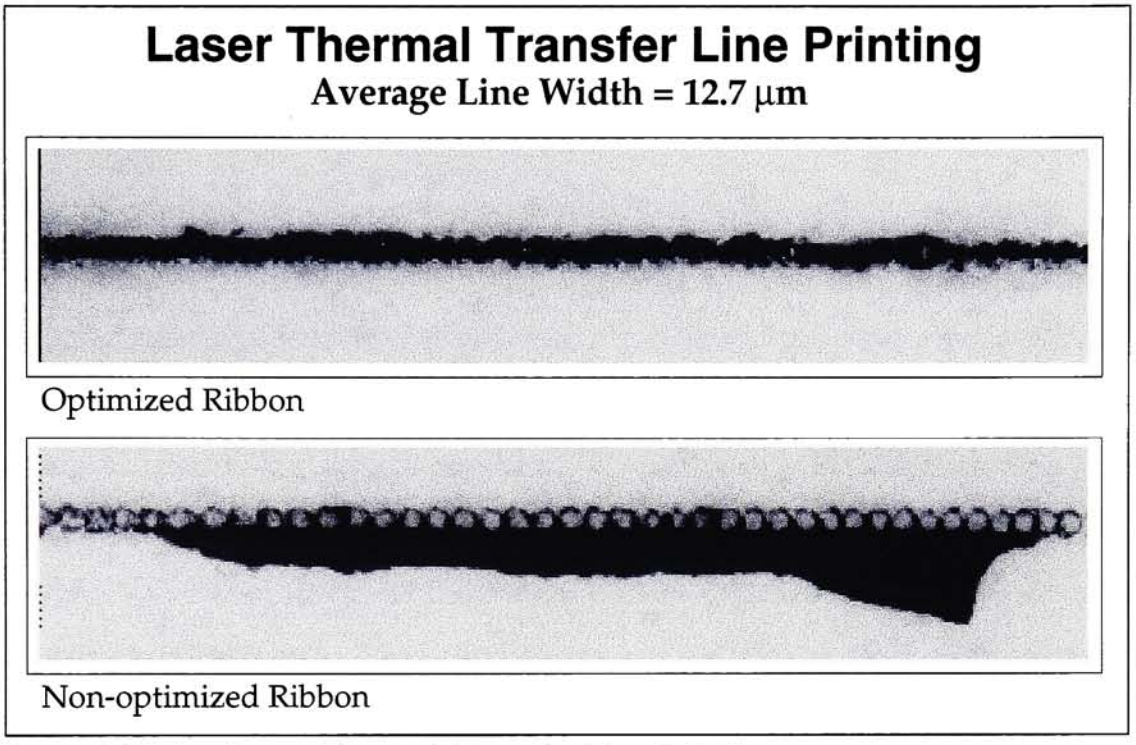

Figure 4.6.4.1 ~ Laser Thermal Transfer Line Printing.

5.0 Conclusions and Recommendations

The RSM model predicted that the optimal ribbon would yield an IQ rating of 9.60. When optimal prints were measured, actual IQ of the system was, on average, 9.8. These results show that given careful control of the imaging system, it was possible to create dots of highly uniform size, shape and placement. Moreover, the above outlined print tests demonstrated that it was possible to vary dot size as well as to print high quality lines with the optimized ribbon and imaging system. The resolution limitations of the system rested in the combined effects of the variation of the RL and PCL coatings and the difficulty of insuring intimate contact of donor to receiver on a sub-micrometer scale. These limitations are not fatal to the further success of the proposed system. Scaling up efforts to machine coating of the donor ribbon alone would significantly decrease variation in the system, leading to increased resolution limits. Further minor refinements to the imaging system would permit similar decreases in variation.

With the experimentation complete, a construction may be suggested for the next LT2 prototype imaging system. It was shown that LT2 can work well using a beam with 20 mWatts total power. At this power, however, writing speed is very slow, at 205 μsec per dot. In order to raise the writing speed of the system, inexpensive diode lasers, multi-plexed laser diodes, and laser diode arrays should be considered. It is now possible to buy a 1 Watt semiconductor laser diode for under $1,000. With some extra effort placed in the beam shaping optics, such a laser would be well suited to LT2. In another

approach, it would be possible to multi-plex three medium power semiconductor laser diodes in order to yield a beam of acceptable power density. Still another possibility would be to employ a diode array, whose parallel elements would be focused onto the ribbon with fiber lenses. To this end, the Vixel Corporation recently introduced the LASE-ARRAY™ family of "...laser diodes for optical information systems" (Vixel Corporation, 1995). While they are modestly rated in the literature, each diode within these arrays will reportedly output 10-12 mWatts. The diodes are individually addressable, and the arrays may be custom built. There are several configurations available, including a 1×64 element unit.

The above ideas represent only a few of a rapidly increasing number of possible solutions to the "power versus speed" dilemma. "In 1994, considerable progress was made in reducing the cost of fiber-coupled diode laser power, and diode sources began to encroach on other laser sources, such as YAG and diode-pumped YAG. This trend will accelerate this year with the introduction of new approaches to achieving improved brightness from diode arrays and getting higher power into fiber diameters..." (Tracy, 1995). Further, "...volume markets for diodes no longer depend on diode-pumping; increasingly, direct thermal applications [i.e. ablating and soldering] are driving volumes accelerating cost reductions" (Tracy, 1995). With laser diodes a key to the success of many laser manufacturers, there is little doubt the speed/cost trade-off will continue to become more favorable in the short, and long, term.

To further increase throughput, ink layer thickness should be reduced. Due to the nature of laboratory mixing and draw-down coatings, it was not possible to produce PCL layers thinner than 4.6 μm due to coating thickness variations. Using a machine coater, a 2 μm PCL thickness could be achieved. Because temperature decreases exponentially with PCL thickness, reducing coating weight by one half would have a great effect. Figures 4.3.2.1 and 4.3.2.2 graphically illustrate the advantage that would be gained in moving to a thinner PCL. For carbon black PCLs, the reduced amount of IR absorber in a thinner layer would probably not present a problem. For color formulations on the other hand, where the absorbency of the IR dye is not nearly as great as that of carbon black, the reduction in thickness would be of greater concern.

Process color LT2 requires further investigation. While some effort was put into color formulations, the vast majority of research performed dealt with carbon black pigmented systems. In the case where color ribbons were formulated, the IR absorbing dye was placed in the PCL. The imaging process was identical to that of the carbon black systems produced. Another approach worthy of future research may be to place a non-transferring IR absorbing layer apart from the PCL and RL, as in Type II LAT (Tolbert, et. al., July/August, 1993) and the color thermal transfer work of Irie, et. al., (1993). In so doing, there would be no contamination of the colorant by the IR absorbing dye, a problem with the investigated approach. Such an approach would, however, trade efficiency for color fidelity, with heat being generated

not in the ink, but in a layer above. Highly absorbent carbon black or certain metals could possibly be used in this type of donor ribbon.

A decision was made early on to produce a system capable of high resolution possessing a modest laser power requirement. As a result, only optics that were absolutely necessary were employed in order to aid in achieving this goal. The decision was made knowing that it would be more difficult to achieve intimate contact between the donor and receiver without overlaying some type of glass element. Great pains were taken to remove entrained air and hold the two layers together with vacuum pressure. One step beyond this approach would be to pull the donor and receiver over a thin ($\approx$ 25 mm) platen, pinching the materials just before and after imaging with pressure rollers. It has been proven that this approach works, although there is variation associated with it. In order to decrease this variation, it would be worthwhile to investigate the use of an optical glass piece placed over the "nip." The piece could be a glass sheet beneath which the donor and receiver slide, or, perhaps more practically, the piece could function as a pressure roller and lens, rolling over the moving materials, with the beam passing through.

The system achieved the goal of the research: to design and implement a novel high resolution thermal transfer printing system capable of making its way onto the desktop. Over the course of the research, many aspects of the LT2 writing system were investigated. Laser exposure systems, beam

modulation systems, optical systems, positioning systems, and measurement techniques were all examined. Both wax and wax/resin inks were designed using both solvent and water based dispersants. The imaging system was modeled and the donor ribbon formulation optimized using techniques of experimental design. Even with this research complete, there certainly is more development to be done. Fortunately laser prices continue to fall; implementation of LT2 will become even more feasible over the next couple years. Further, its simplicity is an asset and its high resolution, efficiency, and capability for variable dot size printing increase its appeal over many current desktop printing technologies.

6.0 Appendices

A. Unit Check of Mathematical Model

Refer to section 4.3.2 for a derivation of the model. As presented by section 4.3.2 equation 38, the mathematical model in its final form is:

$$v = \frac{Qa_b}{2KC}\int_0^{\infty} J_0(\lambda r)J_1(\lambda a_b)\left\{e^{-\lambda\alpha z}erfc\left[\frac{\alpha z}{2(kt)^{1/2}} - \lambda(kt)^{1/2}\right] - e^{\lambda\alpha z}erfc\left[\frac{\alpha z}{2(kt)^{1/2}} + \lambda(kt)^{1/2}\right]\right\}\frac{d\lambda}{\lambda}$$

where

$$Q = \frac{2P}{\pi a_b^{\,2}}e^{-2r^2/a_b^{\,2}} \quad \text{and} \quad a_b = f_{PET}f_{RL}a \ . \tag{1}$$

The individual terms have the following units:

$$\begin{aligned}
v &\equiv [\text{Kelvins}] = [\text{K}] \\
\lambda &\equiv [\text{meters}^{-1}] = [\text{m}^{-1}] \\
z &\equiv [\text{m}] \\
r &\equiv [\text{m}] \\
a &\equiv [\text{m}] \\
a_b &\equiv [\text{m}] \\
C &\equiv [\text{scalar}] \equiv 1 \\
\alpha &\equiv [\text{scalar}] \equiv 1 \\
f_{PET} &\equiv [\text{scalar}] \equiv 1 \\
f_{RL} &\equiv [\text{scalar}] \equiv 1 \\
t &\equiv [\text{seconds}] = [\text{sec}] \\
P &\equiv [\text{Watts}] = [\text{W}] \equiv [\text{J}\cdot\text{sec}^{-1}] \\
Q &\equiv [\text{J}\cdot\text{m}^{-2}\cdot\text{sec}^{-1}] \\
K &\equiv [\text{J}\cdot\text{m}^{-1}\cdot\text{sec}^{-1}\cdot\text{K}^{-1}] \\
k &\equiv [\text{m}^2\cdot\text{sec}^{-1}] \ .
\end{aligned}$$

In order to check the unit validity of the model, the term units may be substituted into the model. Substituting into the group of terms in front of the integral of (1) and ignoring constants yields the following:

$$\frac{Qa_b}{2KC} = \left(\frac{\mathrm{J}}{\mathrm{m}^2 \cdot \mathrm{sec}}\right) \cdot \left(\frac{\mathrm{m}}{1}\right) \cdot \left(\frac{\mathrm{m} \cdot \mathrm{sec} \cdot \mathrm{K}}{\mathrm{J}}\right) = \mathrm{K} \quad . \tag{2}$$

Substituting units into the Bessel Functions within the integral of (1) leads to a scalar:

$$J_0(\lambda r) J_1(\lambda a_b) = J_0\left(\frac{1}{\mathrm{m}} \cdot \frac{\mathrm{m}}{1}\right) \cdot J_1\left(\frac{1}{\mathrm{m}} \cdot \frac{\mathrm{m}}{1}\right) = J_0(scalar) \cdot J_1(scalar) \quad . \tag{3}$$

Likewise, substituting units into both exponential functions produces scalars:

$$e^{-\lambda \alpha z} = e^{-\left(\frac{1}{\mathrm{m}} \cdot 1 \cdot \frac{\mathrm{m}}{1}\right)} = e^{-(scalar)} \quad \text{and} \quad e^{\lambda \alpha z} = e^{\left(\frac{1}{\mathrm{m}} \cdot 1 \cdot \frac{\mathrm{m}}{1}\right)} = e^{(scalar)} \quad , \tag{4}$$

as does substitution into both complementary error functions:

$$erfc\left[\frac{\alpha z}{2(kt)^{1/2}} - \lambda (kt)^{1/2}\right] = erfc\left[\frac{1 \cdot \mathrm{m}}{\left(\frac{\mathrm{m}^2}{\mathrm{sec}} \cdot \frac{\mathrm{sec}}{1}\right)^{1/2}} - \frac{1}{\mathrm{m}}\left(\frac{\mathrm{m}^2}{\mathrm{sec}} \cdot \frac{\mathrm{sec}}{1}\right)^{1/2}\right] = erfc(scalar) \tag{5}$$

and

$$erfc\left[\frac{\alpha z}{2(kt)^{1/2}}+\lambda(kt)^{1/2}\right]=erfc\left[\frac{1\cdot \mathrm{m}}{\left(\frac{\mathrm{m}^2}{\mathrm{sec}}\cdot\frac{\mathrm{sec}}{1}\right)^{1/2}}+\frac{1}{\mathrm{m}}\left(\frac{\mathrm{m}^2}{\mathrm{sec}}\cdot\frac{\mathrm{sec}}{1}\right)^{1/2}\right]=erfc(scalar)\quad .\quad (6)$$

With all of the terms within the integral reducing to scalars, the unit form of (1) simplifies to:

$$v=\mathrm{K}\int_0^{\infty} J_0(scalar)J_1(scalar)\left\{e^{-scalar}erfc[scalar]-e^{scalar}erfc[scalar]\right\}d(scalar)=\mathrm{K} \qquad (7)$$

which is precisely the desired result, with the output of the model v representing Kelvin temperature at a given point within the laser heated ribbon.

B. Pseudo Color Look Up Table for Contour Plots

The following look up table may be used to convert color information to temperature gradient information for the mathematical model output contour plots given in section 4.3.2. The threshold for thermal ink transfer in the designed system corresponds to the third band from the left, which represents a temperature band from 67 to 100 °C.

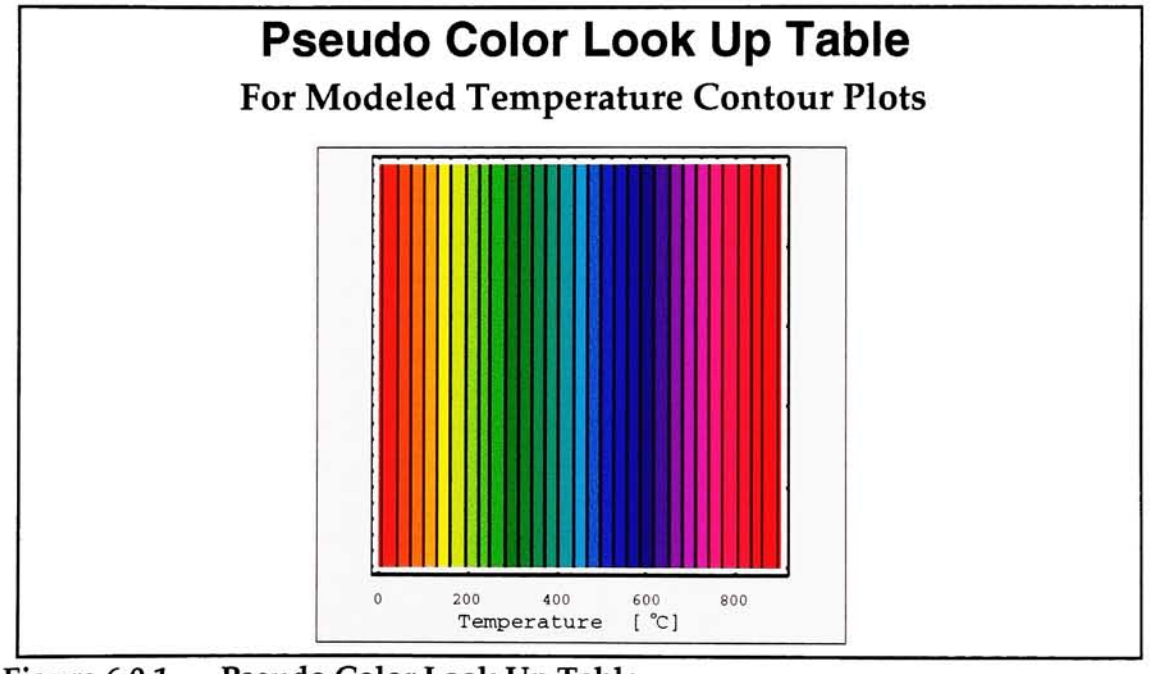

Figure 6.0.1 ~ Pseudo Color Look Up Table

C. Raw Data from Designed Experiment

The table on the following page presents the raw input variable data, observed IQ, RSM model predicted IQ, and residual IQ for the LT2 ink ribbon experimental design.

Run #	Jonwax 120 A	PVP K90 B	SCX 2560 C	Joncryl 624 D	Observed IQ	Predicted IQ	Residual IQ
1	25.0	22.5	1.71	1.52	67.6	69.9	-2.25
2	31.0	15.0	-0.01	3.05	57	49.2	7.84
3	25.0	7.5	5.14	1.52	79.2	79.7	-0.55
4	31.0	15.0	3.43	3.05	20.4	20.0	0.36
5	31.0	15.0	3.43	3.05	19.6	20.0	-0.44
6	18.0	15.0	3.43	3.05	89.4	81.3	8.11
7	38.0	7.5	5.14	1.52	59	61.5	-2.50
8	31.0	15.0	6.86	3.05	95.8	88.9	6.85
9	31.0	15.0	3.43	3.05	20.3	20.0	0.26
10	25.0	7.5	5.14	4.57	94.7	94.4	0.27
11	38.0	22.5	5.14	4.57	49.7	52.8	-3.11
12	31.0	15.0	3.43	3.05	20.1	20.0	0.06
13	38.0	22.5	1.71	4.57	39.1	44.7	-5.60
14	31.0	15.0	3.43	-0.01	65.5	57.3	8.17
15	25.0	22.5	1.71	4.57	83.1	84.5	-1.45
16	38.0	7.5	1.71	4.57	50.4	50.1	0.31
17	38.0	7.5	1.71	1.52	25.9	30.9	-5.00
18	25.0	22.5	5.14	4.57	92.5	93.7	-1.16
19	38.0	7.5	5.14	4.57	60.8	64.7	-3.88
20	31.0	15.0	3.43	3.05	20	20.0	-0.04
21	31.0	15.0	3.43	6.10	82.6	76.1	6.52
22	44.0	15.0	3.43	3.05	25.2	18.6	6.63
23	31.0	0.0	3.43	3.05	81.7	78.1	3.63
24	31.0	15.0	3.43	3.05	20.3	20.0	0.26
25	25.0	7.5	1.71	4.57	76.6	78.8	-2.23
26	31.0	15.0	3.43	3.05	20.2	20.0	0.16
27	38.0	22.5	5.14	1.52	61.7	65.6	-3.92
28	38.0	22.5	1.71	1.52	37.3	41.5	-4.21
29	31.0	15.0	3.43	3.05	20.2	20.0	0.16
30	31.0	15.0	3.43	3.05	19.7	20.0	-0.34
31	31.0	30.0	3.43	3.05	99.8	88.7	11.11
32	25.0	7.5	1.71	1.52	47.3	48.1	-0.84
33	31.0	15.0	3.43	3.05	19.9	20.0	-0.14
34	31.0	15.0	3.43	3.05	20.3	20.0	0.26
35	25.0	22.5	5.14	1.52	90.7	95.0	-4.26
36	31.0	15.0	3.43	3.05	19.6	20.0	-0.44

Table 6.0.1 ~ Raw Data from Formulation Designed Experiment.

7.0 References

_____, **Carbon Black Dispersion,** Cabot Corporation, Bellerica, MA, 1989.

_____, **LASE-ARRAY™ Lightwave Transmitter Advertisement**, Vixel Corporation, Broomfield, CO, 1995.

_____, **Statgraphics Plus Reference Manual, Version 7,** Manugistics, Inc., Rockville, MD, 1993.

_____, **Technical Note 71: Optical Isolators,** Conoptics, Inc., Danbury, CT, 1991.

_____, **Tightly Folded Resonator User's Manual,** SpectraPhysics, Inc., Mountain View, CA, 1992.

_____, **Fluorosurfactants Technical Note**, EI DuPont de Nemours and Co., Wilmington, Delaware, 1993.

Abe, T., Kitamura, S., *Relation Between Dynamic Characteristics of Thermo-Fusible Ink and Print Quality in Thermal Transfer Printing.* **IS&T: Journal of Imaging Science and Technology**, Vol. 17, Santa Clara, CA, 1991, pp. 119-122.

Anderson, V.L., McLean R.A., **Design of Experiments: A Realistic Approach**, Marcel Dekker, Inc., New York, New York, 1974.

Bennett, H., **Commercial Waxes**, Second Edition, Chemical Publishing Co., Inc., New York, New York, 1956.

Bortman, H., *Fine Print.* **MacUser**, Vol. 11, Number 4, Foster City, CA, April, 1995, pp. 75-82.

Brent, R.P., **Algorithms for Minimization without Derivatives**, Prentice-Hall, Englewood Cliffs, New Jersey, 1973.

Carslaw, H.S. Jaeger, J.C., **Conduction of Heat in Solids**, Oxford University Press, Oxford, England, 1959.

Davids, D.A., Chan, K-H., Bertoni, H.L., *Temporal and Spatial Response in Thermal Transfer Printing.* **Proceedings of the SID**, Vol. 28/4, 1987, pp. 465-470.

Ellis, E., Foley, D., Arnold, D., U.S. Patent 5,171,650, May 29, 1991.

Ellis, E., Foley, D., Arnold, D., U.S. Patent 5,256,506, February 26, 1992.

Foley, D., Bennett, E., Slifkin, S., U.S. Patent 5,156,938, May 29, 1991.

Gigon, A., *Thermal Transfer Technology Determination of Cost Performance Competitiveness.* **Proceedings of the Third Annual Thermal Printing Workshop**, Information Management Institute, Inc., 1992, pp. 120-137.

Gregory, P., **High Technology Applications of Organic Colorants**, Plenum Press, New York, New York, 1991.

Heiberger, R.M., **Computation for the Analysis of Designed Experiments**, John Wiley and Sons, New York, 1989.

Irie, M., Kato, M., Kitamura, T., *Thermal Transfer Color Printing Using Laser Heating.* **IS&T: Journal of Imaging Science and Technology**, Vol. 37, Number 3, Santa Clara, CA, May/June, 1993, pp. 235-238.

Irie, M., Kitamura, T., *High Definition Thermal Transfer Printing Using Laser Heating.* **IS&T: Journal of Imaging Science and Technology**, Vol. 37, Number 3, Santa Clara, CA, May/June, 1993, pp. 231-234.

Komerska, J.F., *Thermal Imaging Materials.* **Handbook of Imaging Materials,** Diamond, A., ed., Marcel Dekker, Inc., New York, 1991, pp. 487-526.

Koshizuka, K., Kitamura, S., Abe, T., *The Study on Properties of Thermal Transfer Ink Ribbon.* **SPSE: The Third International Congress on Advances in Non-Impact Printing Technologies,** 1986, pp. 142-147.

Lacy, Y., *Recent Developments in Thermal Transfer Ribbon Technology.* **IMI: Sixth Annual Thermal Printing Workshop Presentation Notes,** 1995.

Lee, I., Tolbert, W., Dlott, D., Doxtader, M., Foley, D., Arnold, D., Ellis, E., *Dynamics of Laser Ablation Transfer Imaging Investigated by Ultrafast Microscopy.* **IS&T: Journal of Imaging Science and Technology**, Vol. 36, Number 2, Santa Clara, CA, March/April, 1992, pp. 180-7.

Letcher, C.S., *Waxes.* **Kirk-Othmer Encyclopedia of Chemical Technology, Vol. 24, Third Edition**, John Wiley and Sons, New York, 1984, pp. 466-481.

Montgomery, D.C., **Design and Analysis of Experiments**, John Wiley and Sons, New York, 1976.

Muller, O., Drews, R.E., *Infrared Microradiometry of Thermal Inkjet Heaters.* **SPIE: Hard Copy Output**, Vol. 1079, CA, 1989, pp. 100-

111.

Nelder, J.A., Mead, R., *Downhill Simplex Method of Multidimensional Minimization.* **Computer Journal**, Vol. 7, New York, New York, 1965, pp. 308-313.

Nelson, T., Shainin, P., **Shainin Statistical Engineering Journeyman Course**, Shainin Consultants, Carson City, Nevada, 1994.

Osipow, L.I., **Surface Chemistry, Theory and Industrial Applications**, Reinhold Publishing Corporation, New York, New York, 1962.

Press, W.H., Teukolsky, S.A., Vettering, W.T., Flannery, B.P., **Numerical Recipes in C, Second Edition**, Cambridge University Press, New York, New York, 1992.

Sheela, B.V., Ramamoorthy, P., *SWIFT -- A New Constrained Optimization Technique.* **Computer Methods in Applied Mechanics and Engineering**, Vol. 6, San Francisco, CA, 1975, pp. 309-318.

Siegman, A.E., **Lasers**. University Science Books, Mill Valley, CA, 1986.

Swift, P. F. , *Quantitative Methods for the Evaluation of Thermal*

Transfer Materials. **European Thermal Printing Workshop Proceedings**, Vol. 1, R.I.T.R.C., September, 1991, pp. 1-27.

Tanaka, Y., Abe, T., *Quantitative Analysis of Print Quality Features.* **SPSE: Journal of Imaging Technology**, Vol. 13, San Francisco, CA, 1987, pp. 202-207.

Tanaka, Y., Koshizuka, K., Abe, T., *Quantitative Evaluation of Print Quality of Thermal Transfer Printing.* **SPSE: Journal of Imaging Science**, Vol. 32, San Francisco, CA, 1988, pp. 210-215.

Tolbert, W., Lee, I., Wen, X., Dlott, D., Doxtader, Ellis, E., *Laser Ablation Transfer Imaging Using Picosecond Optical Pulses: Ultra-High Speed, Lower Threshold and High Resolution.* **IS&T: Journal of Imaging Science and Technology**, Vol. 37, Number 5, Santa Clara, CA, September/October, 1993, pp. 485-489.

Tolbert, W., Lee, I., Wen, X., Doxtader, Ellis, E., Dlott, D., *High Speed Color Imaging by Laser Ablation Transfer with a Dynamic Release Layer: Fundamental Mechanisms.* **IS&T: Journal of Imaging Science and Technology**, Vol. 37, Number 4, Santa Clara, CA, July/August, 1993, pp. 411-421.

Tracy, J., *Diode Lasers Find a Role in Direct Thermal Applications.* **Photonics Spectra**, Vol. 29, Number 1, Pittsfield, MA, January, 1995, pp. 88-90.

Warth, A.H., **The Chemistry and Technology of Waxes, Second Edition**, Reinhold Publishing Corporation, New York, New York, 1956.

Williams, D., Kammin, M., U.S. Patent 4,686,549, August 11, 1987.

Wilson, J., Hawkes, J.F.B., **Optoelectronics: An Introduction, Second Edition**, Prentice Hall International (UK) Ltd., Hertfordshire, England, 1989.